Enhancing the Photovoltaic Performance of Dye-Sensitised Solar Cells for Building Integrated Applications

Submitted by **Prabhakaran Selvaraj** to the University of Exeter

as a thesis for the degree of

Doctor of Philosophy in Renewable Energy

In December 2018

I certify that all material in this thesis which is not my own work has been identified and that no material has previously been submitted and approved for the award of a degree by this or any other University.

Signature: …….

தம்மின்தம் மக்கள் அறிவுடைமை மாநிலத்து

மன்னுயிர்க் கெல்லாம் இனிது.

(*திருக்குறள் - 68)*

All living creatures on this earth feel prouder

when their children are smarter than themselves.

(Thirukkural- 68)

This thesis is dedicated to my parents for their unconditional love and never-ending support.

Abstract

The building sector is responsible for more than one-third of global energy consumption. With increasing global population, the demand for energy efficiency buildings and on-site electricity production is rising. Building integrated photovoltaics (BIPV) is one of the most promising contributors to net-zero energy buildings, while also increasing the aesthetic value of the built environment. Among all the transparent solar cells, dye-sensitised solar cells (DSSCs) have low production cost, semi-transparency nature and a range of colours for building design.

This thesis presents an overview of the current energy scenario and future prospects, state-of-the-art of photovoltaic technologies and the challenges in commercialising new generation solar cells. The first approach here is to find an efficient and low-cost alternative photoanode, sensitiser and counter electrode for DSSC. The tested materials are high surface area mesoporous TiO_2, new ruthenium complex (m-HRD-1) sensitiser and Jet nebulizer spray coated CZTS. All the obtained results are compared with the commercial materials. Secondly, semi-transparent DSSCs are fabricated with different transparencies and their colour properties such as correlated colour temperature and colour rendering index are evaluated. Moreover, glazing properties and daylight glare analysis are studied to assess the possibility of adopting semi-transparent DSSCs into building architectures. Finally, a low solar concentrator is placed on the transparent-DSSCs to enhance their photovoltaic performance. The internal charge transfer mechanism of the DSSCs is also studied to understand the impact of the concentrated light. Furthermore, the performance of the concentrator coupled devices under different light intensities is studied.

The results presented here provide a fertile base for further investigation, which will focus on improving the performance of all the new generation low cost solar cells using optical elements with new designs. The target is to improve the performance and stability of the transparent solar cell devices and use them as BIPV materials to overcome the challenges of the increasing energy demand.

Acknowledgements

This thesis is the culmination of four years of hard work and procrastination. Throughout this time, I have received support, guidance and advice from innumerable people that have all contributed, in their own way, to this piece of work.

First and foremost, I would like to express my gratitude to my thesis supervisor **Dr Senthilarasu Sundaram**, for giving me the opportunity to work under his wings and always going beyond of what is expected for PhD supervision. His enthusiastic approach, numerous moments of attention and positive criticism has kept me going even at times of crisis.

Secondly, I owe a huge amount to my co-supervisor **Prof Tapas Kumar Mallick** for his constant guidance, and determination in giving valuable information and support throughout this research.

I am extremely grateful to the professors of Kongunadu arts and science college, India. Especially **Dr Sathyamoorthy Ramakrishnan** for being my inspirational teacher and mentor from undergraduate days.

The fruitful conversations I have had with several researchers within the department have helped me in my research. I would like to express my sincere gratitude to **Dr Asif Tahir, Dr Hasan Baig, Dr Aritra Ghosh, Dr Sourav Khanna** and **Dr Katie Shanks** for all those exchanges.

I would like to thank my mentor **Prof Stuart Townley** and PGR director **Dr Mohammad Abusara** for their advice and moral support over the course of my work.

My deepest appreciation to all the collaborators and co-authors involved in my milestones. Special acknowledgement to **Richard Little** for proofreading all my articles and helping me to improve my academic English writing skills.

I would also like to thank the **University of Exeter**, as without their funding this work would not have been carried out.

A special thanks must also go to everyone involved in **St. Gluvias cricket club** and **Penryn campus fitness centre** for helping me to keep mentally and physically fit over the last four years.

I am obliged to thank all my fellow **PhD colleagues** and **visiting researchers**, not all the names are possible to be mentioned here, but all my colleagues at ESI made my PhD a memorable experience. I am indebted to all my **friends** and **housemates** in Cornwall who made my stay so pleasant.

Finally, my heartiest thanks to my **family** and **friends** in **India** and in **London** who have been a constant source of support, help and guidance through everything I have done over the years.

P. Selvaraj

Contents

List of figures

List of tables

List of abbreviations

Physical Variables

f	[Hz]	Frequency
FF	[%]	Fill factor
E_g	[eV]	Band gap energy
E_f	[eV]	Fermi level
I_{sc}	[mA]	Short circuit current
J_{sc}	[$mA.cm^{-2}$]	Short circuit current density
R_{CT}	[Ω]	Charge transfer resistance
R_T	[Ω]	Transport resistance
Rs	[Ω]	Series resistance
V_{oc}	[V]	Open circuit voltage
η	[%]	Efficiency
λ	[nm]	Wavelength

Abbreviations

AM	Air mass
ASTM	American Society of Testing and Materials
BHJ	Bulk heterojunction
BICPV	Building integrated concentrated photovoltaics
BIPV	Building integrated photovoltaics

CCT	Correlated colour temperature
CdTe	Cadmium telluride
CIGS	Copper indium gallium selenide
CIS	Copper indium selenide
CPC	Compound parabolic concentrator
CPV	Concentrating photovoltaic
CRI	Colour rendering index
DGI	Daylight glare index
DI	Deionised
DMF	Dimethylformamide
DSC	Differential scanning calorimetry
DSSC	Dye sensitised solar cell
EC	Ethyl cellulose
FTO	Fluorine doped tin oxide
GaAs	Gallium arsenide
HOMO	Highest occupied molecular orbital
HTM	Hole transport material
ITO	Indium tin oxide
JCPDS	Joint Committee on Powder Diffraction Standards
LUMO	Lowest unoccupied molecular orbital

LCPV	Low concentrating photovoltaics
MPN	N-methoxypriopionitrile
N719 dye	Di-tetrabutylammonium cis-bis(isothiocyanato)bis(2,2′-bipyridyl- 4,4′-dicarboxylato)ruthenium(II)
NREL	National Renewable Energy Laboratories (USA)
NSG	Nippon sheet glass
OPV	Organic photovoltaic
P3HT	Poly(3-hexylthiophene)
PCE	Power conversion efficiency
PEN	Polyethylene naphthalate
PET	Polyethylene terephthalate
PV	Photovoltaic
SEM	Scanning electron microscopy
Si	Silicon
SPD	Suspended particle device
ss-DSSC	Solid state dye sensitised solar cell
TCO	Transparent conducting oxide
TEM	Transmission electron microscopy
TGA	Thermogravimetric analysis
TiO2	Titanium Dioxide
UV-Vis	Ultraviolet-visible
XRD	X-ray diffraction

List of publications

Publications included in the thesis

1. **Prabhakaran Selvaraj**, Hasan Baig, Tapas Kumar Mallick, Jonathan Siviter, Andrea Montecucco, Wen Li, Manosh Paul, Tracy Sweet, Min Gao, Andrew R. Knox, Senthilarasu Sundaram. “Enhancing the efficiency of transparent dye-Sensitised solar cells using concentrated light.” *Solar Energy Materials and Solar Cells* **2018**, *175*, 29.
2. **Prabhakaran Selvaraj**, Hasan Baig, Tapas Kumar Mallick, Senthilarasu Sundaram. “Charge transfer mechanics in transparent dye-Sensitised solar cells under Low concentration.” *Materials Letters* **2018**, *222*, 78.
3. **Prabhakaran Selvaraj**, Anurag Roy, Habib Ullah, Parukuttyamma Sujatha Devi, Asif Ali Tahir, Tapas Kumar Mallick, Senthilarasu Sundaram, “Soft - template synthesis of high surface area mesoporous titanium dioxide for dye - sensitised solar cells.” *International Journal of Energy research* **2019**, 43, 523–534.
4. **Prabhakaran Selvaraj**, Aritra Ghosh, Tapas Kumar Mallick, Senthilarasu Sundaram. “Investigation of semi- transparent DSSCs for fenestration integration.” *Renewable Energy* **2019**, 141, 516-525)
5. Aritra Ghosh, **Prabhakaran Selvaraj**, Senthilarasu Sundaram, Tapas Kumar Mallick. “The colour rendering index and correlated colour temperature of dye-sensitised solar cell for adaptive glazing application.” *Solar Energy* **2018**, *163*, 537.
6. Tejaswi Jella, **Prabhakaran Selvaraj**, Hari Upadhyaya, Tapas Kumar Mallick, Senthilarasu Sundaram, Lingamallu Giribabu. “Synthesis and Photo Electrochemical Characterization of an Extended π-Conjugated

Heteroleptic Ruthenium (II) Complex" *Open Access Journal*, **2017**, *1*, 1.

7. David Kirubakaran, Sudhagar Pitchaimuthu, Ravi Dhas, **Prabhakaran Selvaraj**, Smagul Karazhanov, Senthilarasu Sundaram. "Jet-nebulizer-spray coated copper zinc tin sulphide film for low cost platinum-free electrocatalyst in solar cells." *Materials Letters,* **2018**, *220*, 122.

Publications not included in the thesis

1. Anurag Roy, Partha Pratim Das, **Prabhakaran Selvaraj**, Senthilarasu Sundaram, Parukuttyamma Sujatha Devi, "Perforated $BaSnO_3$ nanorods exhibiting enhanced efficiency in dye sensitised solar cells." *ACS Sustainable Chemistry & Engineering* **2018** *6 (3), 3299-3310.*
2. Anurag Roy, Partha Pratim Das, **Prabhakaran Selvaraj**, Senthilarasu Sundaram, Parukuttyamma Sujatha Devi, "Morphology tuned $BaSnO_3$ active layer for ambient perovskite solar cells." *Materials Letters.* **2018**, *219*, 166.
3. Chenglong Wan, Yinglung Ho, S. Nunez-Sanchez, Lifeng Chen, M. Lopez-Garcia, J. Pugh, Bofeng Zhu, **Prabhakaran Selvaraj**, Tapas Kumar Mallick, Senthilarasu Sundaram, Martin Cryan, "A selective metasurface absorber with an amorphous carbon interlayer for solar thermal applications." *Nano Energy* **2016**, *26*, 392.

Chapter 1: Introduction

Solar energy is regarded as the most available source on earth because of its sufficient amount to cover all human energy consumption. After a brief review of energy crisis and importance of renewable energy sources, this chapter gives an overview of existing photovoltaic technologies and their market scenario. It also presents a review of the state of-the-art of one attractive new type of photovoltaic system that mimic natural photosynthesis, dye-sensitised solar cells. Moreover, the challenges that the research community facing to make these new devices commercialised and their solutions are discussed here. Furthermore, the objective and the structure of this thesis is given in detail in the last part of this chapter.

1.1. Motivation

The law of conservation of energy states that,

"Energy can neither be created nor destroyed - only converted from one form to another"

Energy is a key factor in economic development and in providing vital services that improve quality of life [1]. According to the recent world energy outlook report, primary energy consumption grew by 2.2% in 2017 compared to 2016 and is expected to reach 18 billion tonnes of oil equivalent (toe) by 2040 [2]. A third of global energy growth attributed to buildings, the increase in energy use in buildings is driven by a combination of growing population and increasing prosperity, allowing people to live and work in greater comfort [2,3].

As shown in Figure 1, various fossil fuel resources such as oil, coal and natural gas are the largest energy sources for all the sectors as well as regions in the world. The non-combusted use of oil, gas and coal, e.g. as feedstocks for

petrochemicals, lubricants and bitumen, grows robustly driven by particularly strong growth in plastics. The non-combusted use of fuels grows by 1.7% p.a., accounting for around 10% of the overall growth in energy demand. Oil-based fuels account for around 60% of this growth, followed by natural gas (30%) and coal (10%). However, due to the rapid development of modern industrial economy and the sharp increase in population, these conventional energy sources have been gradually depleted [4].

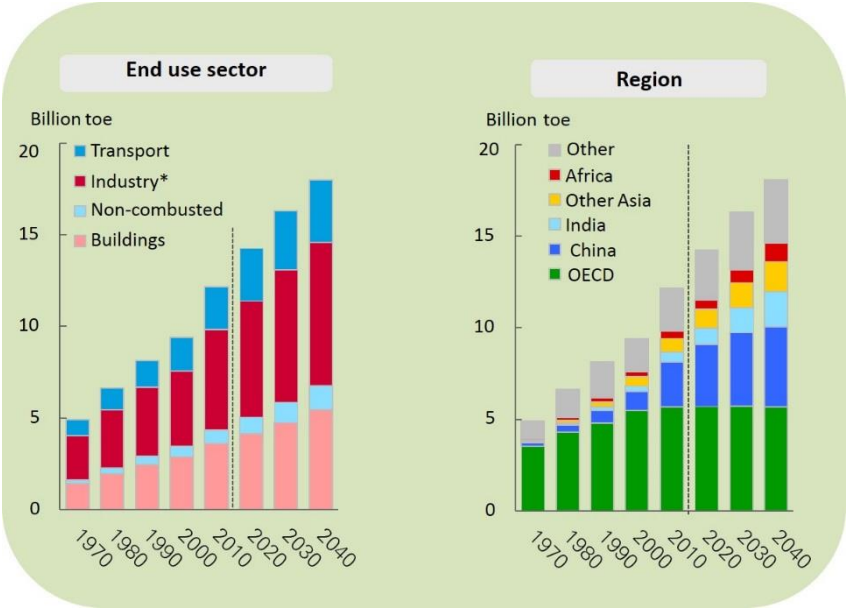

Figure 1. Primary energy demand by sector (left), and region (right) [2]

As shown in Figure 2, the vast majority of the growth in energy used in buildings is provided by electricity, reflecting greater use of lighting and electrical appliances and the increasing demand for space cooling in much of the developing world (Asia, Africa and the Middle East) as living standards increase. There is also small increase in gas consumption, which gains share from both coal and oil in space heating and cooking [2].

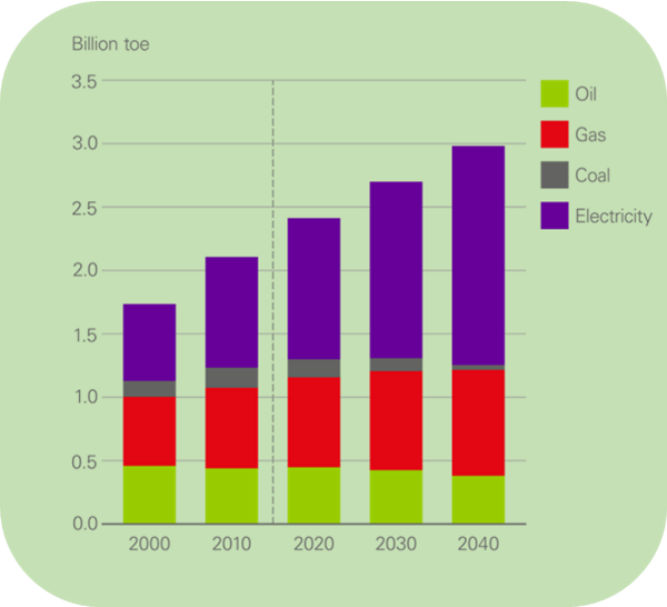

Figure 2. Final energy consumption in buildings by fuel

Since fossil fuels meet a majority of world energy needs and because buildings are a large energy consumer, they are also a major contributor to global carbon emissions. It is now largely recognized that addressing energy use in buildings can reduce total fossil fuel consumption and associated GHG emissions. Benefits such as decreased building operational energy costs have prompted growing interest among policy makers, the technical community, and the general public in addressing building energy issues and investigating solutions for decreasing building energy consumption [5].

The world is blessed with abundant primary energy resources enough to meet its present and future development requirements. Even though both renewable and nuclear energy can mitigate carbon emissions in the short-run, it was proved from the data from 30 countries that only renewable energy can achieve carbon mitigation in the long-run [6].

Renewable energy is defined as “energy produced from sources that do not deplete or can be replenished within a human’s life time”. As mentioned in

the existing literature, renewable energy use can promote economic growth. In simple words, the increased uptake of renewable energy is essential from both the economic and the ecological aspects [7].

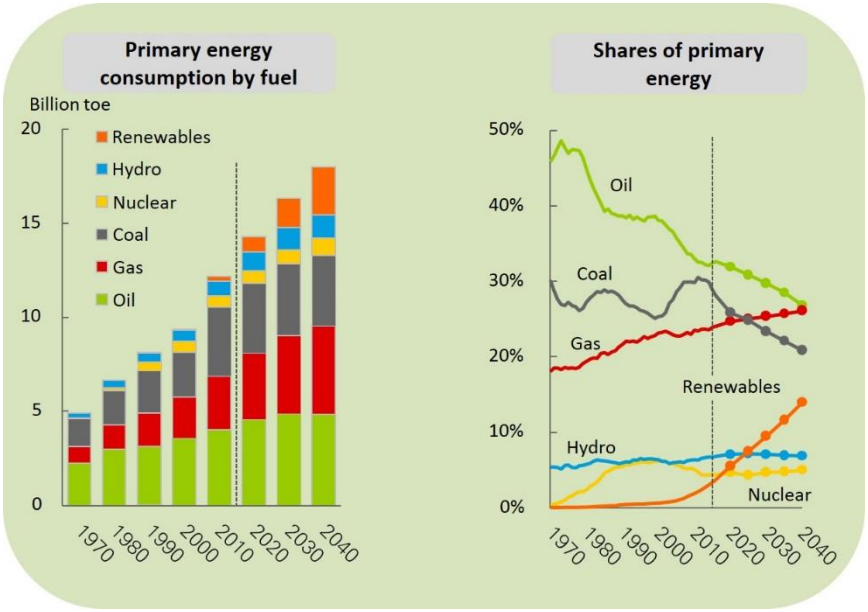

Figure 3. Global energy by fuel [2]

According to the same energy report, renewable energy is the fastest growing source of energy account for over 40% increase in energy supplies. With its shares in primary energy increase from about 4% now to 14% by 2040 as illustrated in Figure 3. In the United Kingdom, renewable energy resources generate 27.9% of tolal electricity and solar PV represents a 3.4% share of total electricity generation [2].

Among all the renewable energy technologies, solar energy is considered as the most powerful energy resource because it is abundant in most part of the world. So, the solar power generation is expected to become competitive with fossil-fuel power generation within the next few decades [8]. In addition to the source abundance, solar energy has another competitive advantage: they can be

independent of the grid and therefore are useful in remote areas or for mobile applications as shown in Figure 4.

Figure 4. Two examples of the independent use of solar energy in Nepal (a) A solar cooker uses the energy of the sun to cook and (b) solar panel empowers villagers [9,10]

1.1.1. Aims and Objectives of Research

Aim

The aim of this thesis is to enhance the DSSCs efficiency for building integrated photovoltaic applications and study the compatability of the system within the buildings.

Objectives

2. Reviewing the new generation photovoltaic technology, disseminating the technology into its multiple constituents and identifying routes to enhance the efficiency for applying in wider applications.
3. Finding alternative materials for cost effective DSSCs. This includes low cost metal oxide nanoparticles, sensitisers with high thermal stability, and Pt- free counter electrode.
4. Analysing the colour properties, solar factor, and daylight glare factor of transparent DSSCs for different weather conditions to find their suitability in BIPV Windows.
5. Studying the effect of low concentrator on semi-transparent DSSC performance to enhance the efficiencey and overcome scaling-up challenge. This includes device performance under different light conditions.

1.2. Solar energy

The amount of energy coming from the sun that hits the surface of the Earth every year is 10 thousand times bigger than the overall energy consumption. In other words, every second the sun delivers 120 petajoules of energy to the earth and in 1 hour the sun gives more energy to the earth than the energy consumed by humans in an entire year [11]. Even with an energy consumption on the rise, especially from newly industrialized countries comprising China, India, Brazil and Mexico, the opportunities that are offered by the Sun's gigantic potential are vast and need to be harnessed with no future delay [12].

5.1.2. 1.2.1. Solar irradiation

The sunlight reaching earth has a characteristic spectrum with intensity peaks in the visible and infra-red range. It does not have uniform irradiance across wavelengths and hence, certain wavelengths have poor irradiance even though a solar device may have the capability of absorbing them. The American Society for Testing of Materials (ASTM) has set a global reference standard for solar spectral distribution [13]. It provides tables for spectral irradiance distributions that are used to compare the performances of products and technologies. The total integrated irradiance for the so-called hemispherical tilted spectrum is 1000.4 W/ m^2. In effect, attenuation of sunlight increases with the distance photons have to travel through the atmosphere because of photon absorption and scattering. The ratio of a solar photon's path length (L) through the atmosphere divided by the thickness d of the atmosphere is defined as the air-mass (AM) coefficient [14,15]. AM 0 corresponds to a solar radiation spectrum above the atmosphere of the Earth and AM 1.5G designates the total global hemispherical irradiance that is commonly used when measuring solar cells. This aspect can be best illustrated by the figure below.

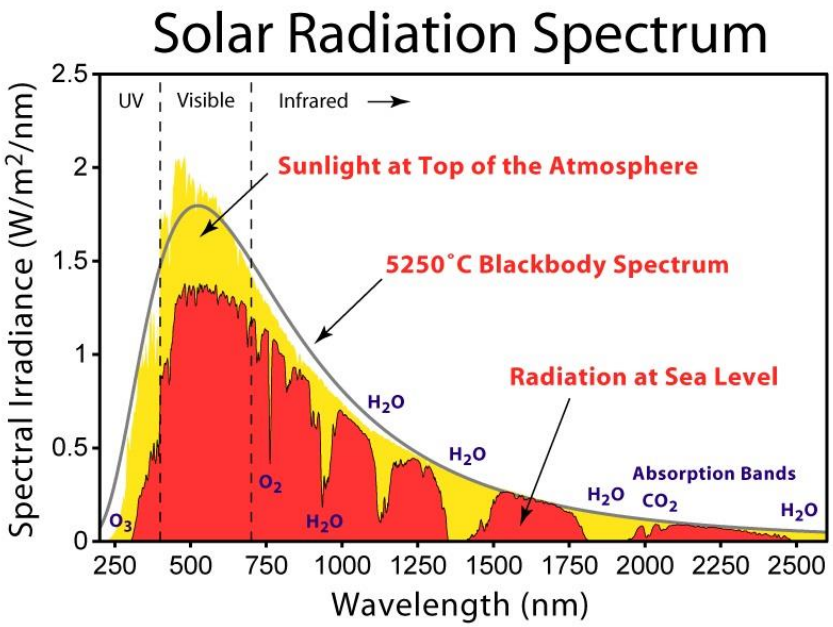

Figure 5. Solar radiation spectrum for direct light at the top of the atmosphere (AM 0) and at sea level (AM 1.5G), the latter corresponding to the standard solar reference. A blackbody spectrum at 5250°C and the specific absorption bands are also given [15]

Solar irradiation can be converted into several energy forms such as heat, chemical energy via natural photosynthesis in plants and electricity. Electrical energy is indeed the product of a particular transformation which is dubbed as photovoltaic (PV) energy conversion [12].

5.3. Photovoltaic Technologies

The term “photovoltaics” (PV) refers to the conversion of sunlight into electrical power, gets its name from the process of converting light (photons) to electricity (voltage), which is called the PV effect [16].

5.3.1. The photo electric effect

The creation of electric potential between two electrodes attached to a solid or liquid system when it is irradiated by light was discovered by French physicist Bequerel in 1839. At the beginning of the 20th century, Albert Einstein was able

to experimentally explain the photoelectric effect, which led him to win a Nobel Prize in 1921. This discovery set a milestone in science for a variety of concepts to convert solar radiation into electricity and has opened a new domain of alternative energy generation [17].

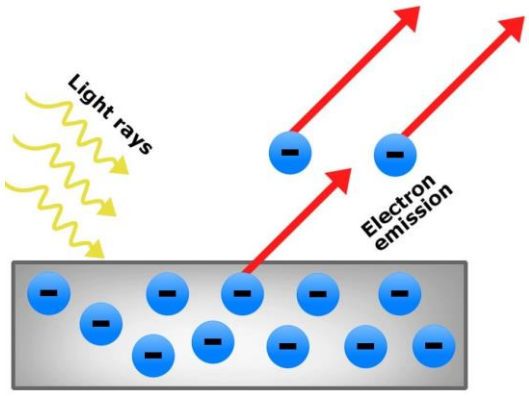

Figure 6. The photo electric effect [18]

In the 1950s, Bell Laboratories developed the first p-n junction using silicon, which reached 6% efficiency. Space was among the first domains where solar panels were used – due to their advantageous power-to-weight ratio – and this helped the promotion of the technology [12,19].

5.3.2. PV cells classification

Several factors including cell material (e.g. silicon, semiconductor compounds, sensitiser, electrolyte); cell size (the larger the cell size, the more the individual cells transforming into either more voltage or current); intensity and quality of the light source, determines the amount of electricity generated.

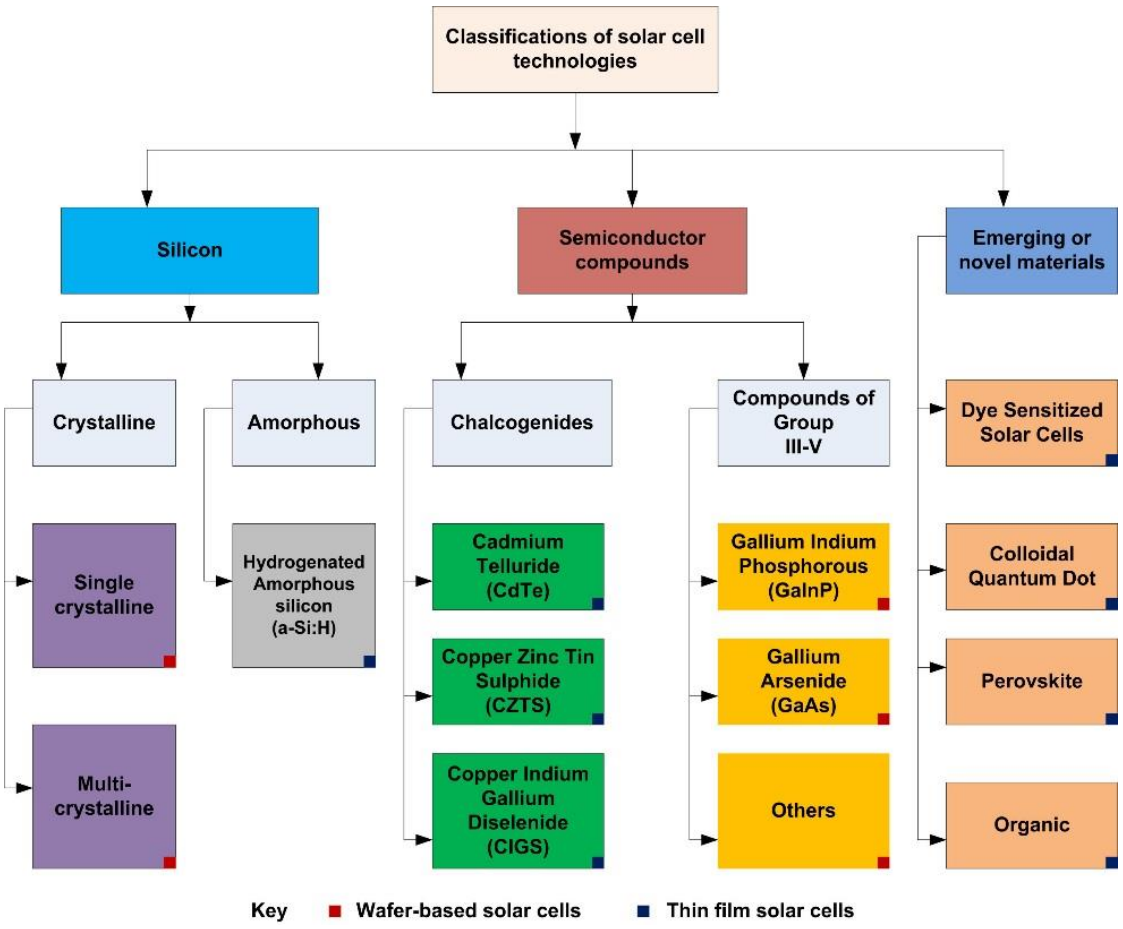

Figure 7. Classification of different generation photovoltaic technologies [20]

As such, PVs are generally grouped into three categories (Figure 7) based on either the active materials (i.e. the primary light-absorbing materials) used for the solar cells or overall device structures [21].

5.3.3. First generation solar cells

Wafer- based single crystalline or multi- crystalline silicon (sc-Si and mc-Si) and GaAs thin film solar cells belong to the first-generation solar cells. The former two accounted for 93% of the global market in 2017 with their best module efficiencies being around 22% for sc-Si and 16% for mc-Si [22].

p-n junction is needed in semiconductors to make them as a solar cell. This p-n junction is created through dopants. One side of the semiconductor is doped with another material at a ratio of about 1 dopant to 1 million original atoms

[23] . The ‘n-type’ side of the semiconductor has dopants with one electron in the valence band that it wants to shed, and the ‘p-type’ side of the semiconductor has dopants that want to incorporate an electron. The ‘n-type’ dopant can be a V or VI column material in the periodic table, and the ‘p-type’ dopant is usually a II or III column material. In the ‘n’ region, the conductivity of electrons is strongly increased, while in the ‘p’ region, the conductivity of electron holes is prevalent. This leads to an electrochemical potential that forces electrons from the ‘p-type’ region to the ‘n-type’ region and vice versa for the holes in the ‘p-type’ region [24].

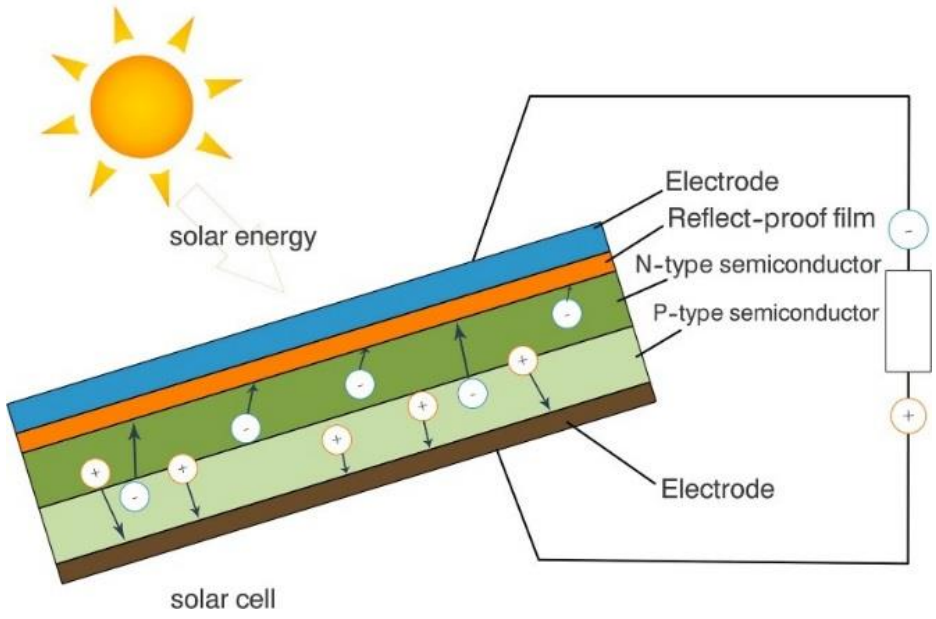

Figure 8. Basic configuration of a p-n junction solar cell [25]

When light hits the semiconductor, photons add energy for an electron to pass from the ‘p’ side to the ‘n’ side and allow a hole to pass in the opposite direction. With an external current path, the electron flows outside the cell, generates electricity, and then returns to the ‘p’ side, completing the circuit and refilling the hole. The minimum amount of energy required to bump the electron from the ‘p’ side to the ‘n’ side of the semiconductor (known as the band-gap) corresponds to the depletion zone [26]. A photon lacking the same or more

energy than the bandgap does not excite an electron. A photon with more energy than the bandgap excites an electron, and the rest of the energy turns into heat. This, along with the absorption of light in all other layers of the cell, is the primary loss mechanism in a photovoltaic cell.

The solar cell is made from one contacted wafer, while the module is a panel containing a number of cells wired with each other in an array. These cells are covered and protected by glass panes. Thus, modules consist of the cells, electrical contacts and wiring between cells and to other modules, and protective coverings, with numerous interfaces [27].

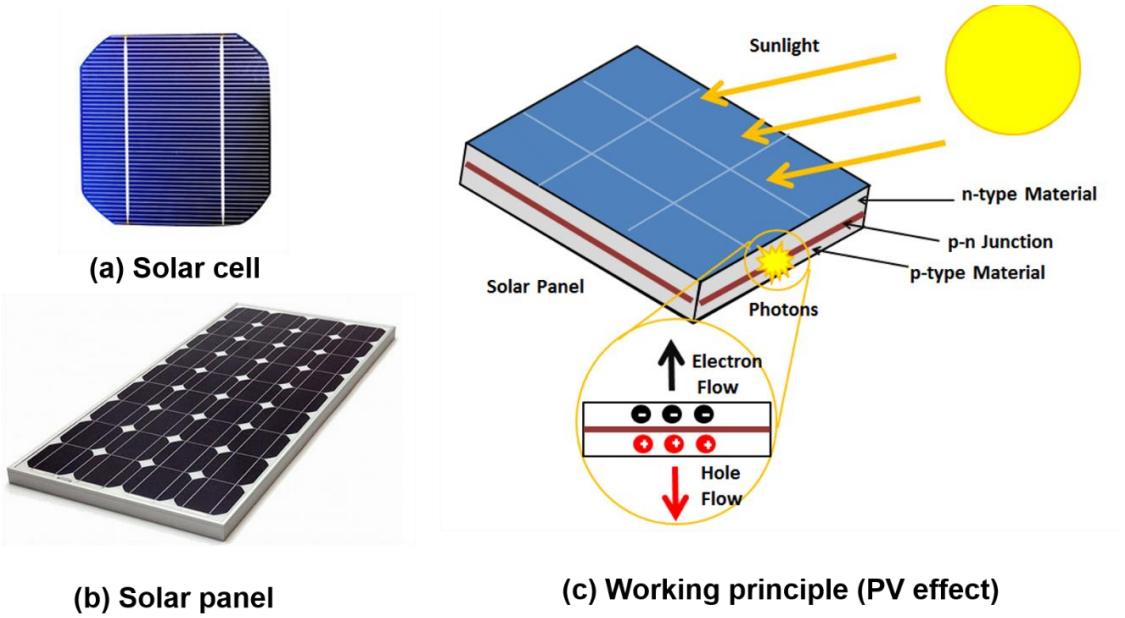

Figure 9. (a) Single cell, (b) panel, and (c) working principle of first generation monocrystalline silicon solar cell [28]

The most common type of solar cell is made of crystalline silicon. This is because silicon is abundant, non-toxic, has an appropriate bandgap of 1.1 eV, and respective process technology has been intensively investigated and developed for microelectronics [29]. Higher efficiencies have been achieved in the laboratory, 26.7% for sc-Si and 28.8% for GaAs [22]. The use of GaAs solar

cells is typically restricted to space applications or to concentrator solar cells, due to their high cost. Owing to the low absorption coefficient of crystalline silicon, thick layers of active material are used [30].

The major bottleneck of silicon is its relatively weak absorption of light, forcing silicon to be used in a relatively high thickness in order to absorb sufficiently. Silicon is generally doped with boron or phosphorus, but this must be done in a clean environment to control impurities. Also, silicon is a brittle material, which limits the lower bound on its thickness. Because of these thickness limitations, the material cost of silicon solar cells is high and can be lowered only to a certain extent [29].

5.3.4. Second generation solar cells

Second generation solar cells are based on thin film technologies such as amorphous silicon (a-Si), cadmium telluride (CdTe) and copper- indium- gallium-selenide (CIGS), with thicknesses that are usually 1-2 orders of magnitude lower than those wafer-based crystalline silicon solar cells. As a result of the small amount of active material needed, lower manufacturing cost and shorter energy payback times are achieved. In addition, thin film solar cells offer the possibility to be used with flexible substrates. Best laboratory efficiencies are close to 20% for CdTe and CIGS and are around 10% for amorphous silicon [19].

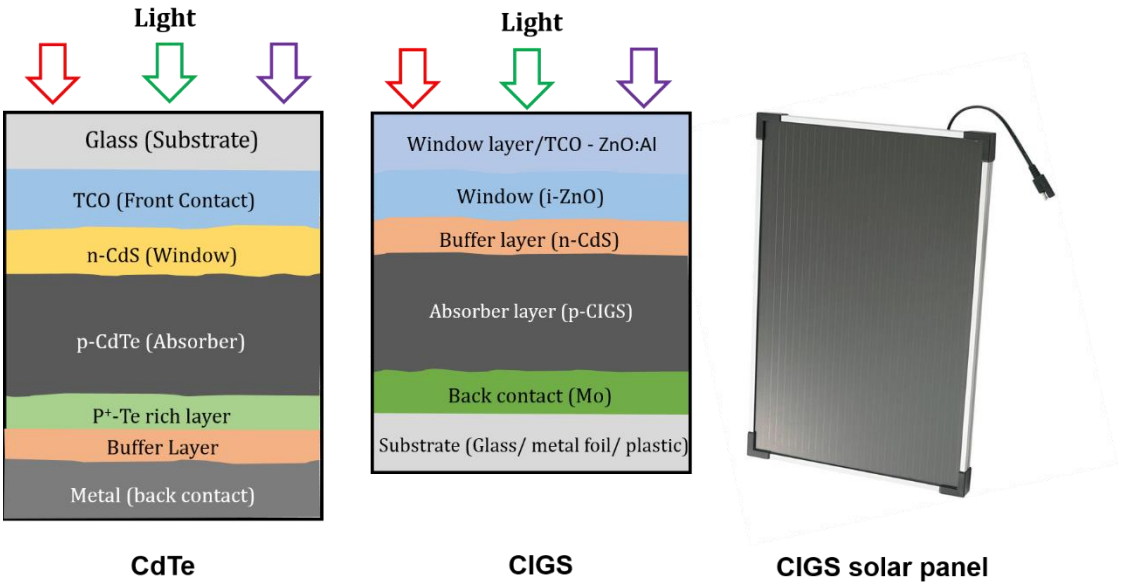

Figure 10. Schematic architecture of second generation CdTe, CIGS solar cells [29]

A thin film solar cell is composed of several layers of different elements. In addition to the absorbing layer there is a transparent conducting oxide (TCO) layer, a window layer, and rear metal contact layer, etc. The properties of each of these layers, the structure of the solar cell and the properties of the interfaces between different layers are important factors that influence the actual efficiency of the thin film cell [31]. In recent years, the conversion efficiency of thin film a-Si solar cells has been improved by a number of technologies. The earliest amorphous silicon solar cells were used in calculators and digital watches [32].

CdTe and CIGS solar cells are the other types of commercialized thin film solar cells. Figure 10 shows a schematic of the structure of a CdTe thin film solar cell. CdTe has an excellent theoretical energy conversion efficiency of 29% due to its bandgap of 1.5 eV. Because the optical absorption coefficient is 105 cm^{-1}, a CdTe layer with a thickness of several μm can absorb 90% of incident photons, making it attractive for use in a thin film solar cell [29].

The polycrystalline semiconductor materials of CdS and CdTe have the advantage of high chemical stability. Up to 21% energy conversion efficiency has been achieved for a laboratory CdTe thin film solar cell. The efficiencies of commercial CdTe thin film modules are typically 10–11%. A major advantage of the CdTe thin film solar cell over the a-Si and CIGS cells is the simple and low-cost deposition process required for fabrication of the cell elements. The main issue of the CdTe cell is the toxicity of cadmium, which can cause environmental problems [33].

CIGS has the best optical absorption coefficient spectrum. Due to its large absorption coefficient of up to 105 cm^{-1} and wide bandwidth, a CIS or CIGS layer with a thickness of 1 or 2 μm can absorb most of the photons over almost the entire sun light spectrum [29]. Figure 10 shows a schematic of a CIGS thin film solar cell. Differing from the a-Si and CdTe cells, the CIGS cell employs a substrate configuration. This provides CIS/CIGS cells with flexibility in selection of substrate materials because there is no requirement on the light permeability of the substrate. For this reason, low-cost substrates can be employed for CIS/CIGS cells, which contribute to cost effectiveness of the CIS/CIGS cell. The CIS/CIGS cell also employs the heterodyne-junction structure, which consists of a substrate, a molybdenum (Mo) back contact film, a CIS/CIGS absorber p-type layer with a thickness of 1 μm, a CdS n-type layer with a thickness of 50 nm, and a TCO layer. The CIS/CIGS absorber p-type layer and a CdS n-type layer form the heterodyne junction. Soda-lime glass is often used as the substrate for the CIS/CIGS cell. In addition to its cost effectiveness, the sodium atoms in the soda-lime glass diffusing from the glass into the CIS/CIGS layer improve the doping concentration in the CIS/CIGS absorber layer during the fabrication process. The best energy conversion efficiency of a CIGS cell is reported to be 22.9%, and that

of a CIGS module is 17.4%. Since the CIS/CIGS cell is composed of much more material elements than a-Si and CdTe cells, more attention toward process control is necessary during their fabrication [34].

The energy conversion efficiency of a solar cell is mainly determined by the properties of the PV material. Among the thin film PV materials mentioned, CdTe has the highest theoretical efficiency of about 29%, followed by a-Si (about 26%) and CIGS (22.9%). A large portion of the overall light energy is lost instead of being converted to electrical energy [35]. There are several reasons for such energy loss. Which has been explained by Shockley-Queisser limit and will be discussed in section 1.4 .

Although the amount of thin film cells is growing, there is a downside to the growth of some of the cells. The materials used in some thin film solar cells, such as Gallium, Indium, and Tellurium, are rare-earth materials and therefore expensive. If these cells become popular, the prices will rapidly increase because of the diminishing amounts of these rare materials. Continuing research on using more common materials in thin film cells and improving their conversion efficiencies will allow these cells to become more efficient and less expensive [19,29].

5.4. Maximum conversion efficiency- Shockley-Queisser limit

As discussed earlier, the maximum achievable solar energy conversion efficiency for a single absorber material was derived by Shockley and Queisser in 1961 [14] and is shown in Figure 11. Their calculation was based on the detailed balance between incoming radiation, emission by radiative recombination and generated photocurrent, assuming an ideal semiconductor with a sharp optical absorption edge and infinite carrier mobilities. Under 1.5 G illumination, a maximum

conversion efficiency of 33.8% can be obtained using a material with a bandgap of 1.34 eV. Several losses contribute to this maximum efficiency limit. The most important is due to the trade-off between the number of absorbed photons (defining the current generated by the solar cell) and the energy of the photogenerated carriers in the absorber (related to the photovoltage of the cell). A semiconductor with a bandgap (E_g) absorbs only photons with energy $h_v \geq E_g$ and the generated carriers rapidly thermalize to the lower energy configuration. Therefore, a small bandgap absorber is desirable for harvesting a large fraction of the solar spectrum, but most of the energy of the photons is lost in the material. A large bandgap semiconductor, on the other hand reduces these thermalisation losses, but captures less photons. The maximum efficiency based solely on this process for all the materials used in solar cells is shown in Figure 11 [15,19] .

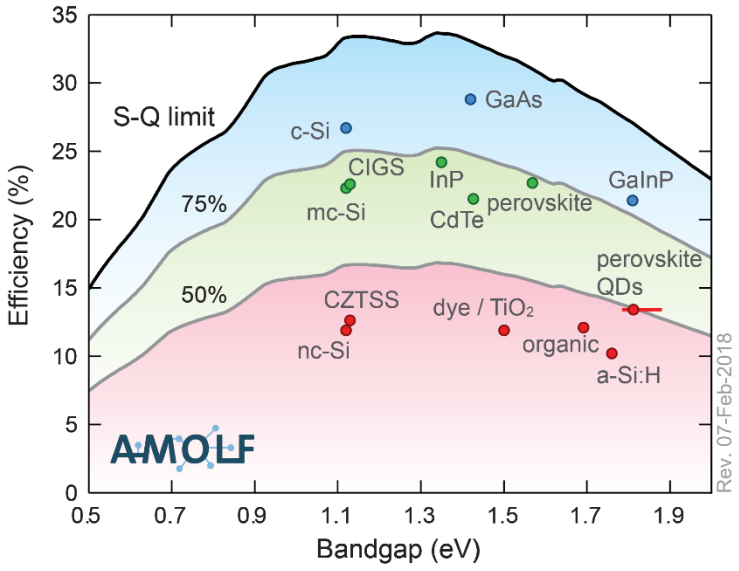

Figure 11. Fraction of the Shockley-Queisser detailed-balance limit (black line) achieved by record cells, grey lines showing 75% and 50% of the limit [36]

5.5. PV market

According to the recent report (shown in Figure 12), first and second generation solar cells (mono-si, multi-si and thin film PV) leading the photovoltaic production market [37]. The commercial and domestic adoption of photovoltaics as an energy source depends on its costs to consumers, and on how it compares with that of conventional energy sources. While recent cost reductions of modules are a step in the right direction, it is believed that the costs are not yet low enough to guarantee substantial uptake of photovoltaics by consumers.

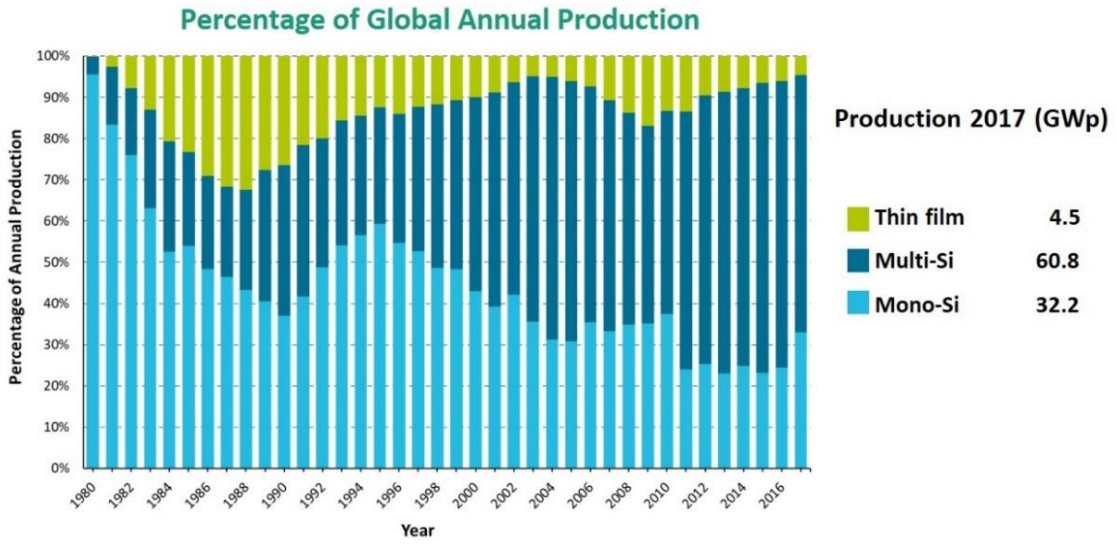

Figure 12. PV production by technology [37]

According to Figure 13, for widespread adoption of solar, the costs (in USD) of next-generation photovoltaics should probably be reduced to a half or a third of the average grid costs (that is, 0.05 to 0.03 USD/kWh; shaded region in the Figure 13). This can be achieved, for example, by a module with an efficiency of 40% and a cost per unit module area of 160 USD/m^2, or a PCE of 30% with a module cost of 120 USD/m^2. Figure 13 shows the relationship between cost/m^2, rated module PCE and cost/kWh. These targets assume long-term stability (10–15 years) and no environmental degradation or negative impact [38].

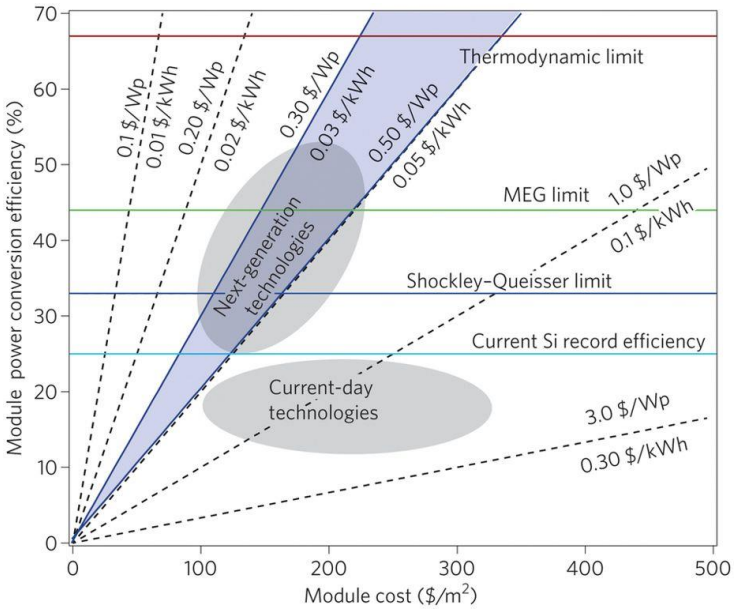

Figure 13. Power conversion efficiencies and module costs for current and new generation photovoltaic technologies [38]

According to the Shockley–Queisser detailed balance analysis [14], the PCE of photovoltaic devices with a single light-absorbing component is capped at ~33%. The first silicon-based solar cell, had PCE of less than 1% [39]; since then, owing to advances in materials processing/quality and device configurations, PCEs have asymptotically approached the Shockley–Queisser limit. The current laboratory record efficiencies for Si is 26.7%, while for GaAs it is 28.8% [22]. These record efficiency cells employ bulk crystalline semiconductors.

Nanoscale systems exhibit different properties than bulk or thin films of the same compounds and have allowed new ways of approaching solar energy conversion for electricity generation or fuels. The large surface-to-volume ratio of nanomaterials can provide various benefits, and, furthermore, objects with a size of ~1–20 nm can also exhibit quantization effects, which become more pronounced with decreasing size. Two broad approaches based on

nanostructures are being explored for photovoltaics: (1) significant reduction in material usage and/or associated final costs; (2) photovoltaic devices with a higher limiting efficiency than that determined by the Shockley–Queisser analysis. Both approaches, individually or in combination, can lead to significantly lower costs per kWh as illustrated in Figure 13. The light blue line represents the current laboratory record efficiency for bulk crystal silicon while the blue horizontal line is the Shockley–Queisser limit for single-junction devices. Current technologies are limited by these efficiencies. Third-generation device concepts increase the limiting efficiency (the limit for MEG is indicated as the green line). For next-generation technologies, the goal is to reach 0.03–0.05 USD/kWh, denoted by the blue shaded region.

A given cost/Wp (dashed black lines) can be achieved at a lower efficiency if the module costs also decrease, and higher module costs can be tolerated if the module PCE also increases. Nanoscale objects provide opportunities to revolutionize the conversion of solar energy by enabling highly efficient and low-cost devices. Challenges associated with demonstrating high efficiency and stability are now being addressed in the research community [22].

5.6. Third generation solar cells

The category of third generation solar cells originally comprised of technologies that allow achieving ultra-high efficiencies above the Shockley-Queisser limit. Examples are tandem or multi-junction cells, intermediate band solar cells, hot-carrier cells, photon up-or down conversion and concentrator solar cells [40]. Emerging technologies with the potential of significantly reducing the cost per Watt peak, such as organic solar cells, dye-sensitised solar cells and perovskite solar cells, are usually included into the category of third generation solar cells [41]. These cells are considered as promising technology especially in building-

integrated PV market for the future due to its transparency, easy process, low production cost, flexibility and high efficiency, but their long-term stability is not yet high enough to be competitive. However, they have the potential to become more efficient than silicon cells through better light trapping and material selection [42].

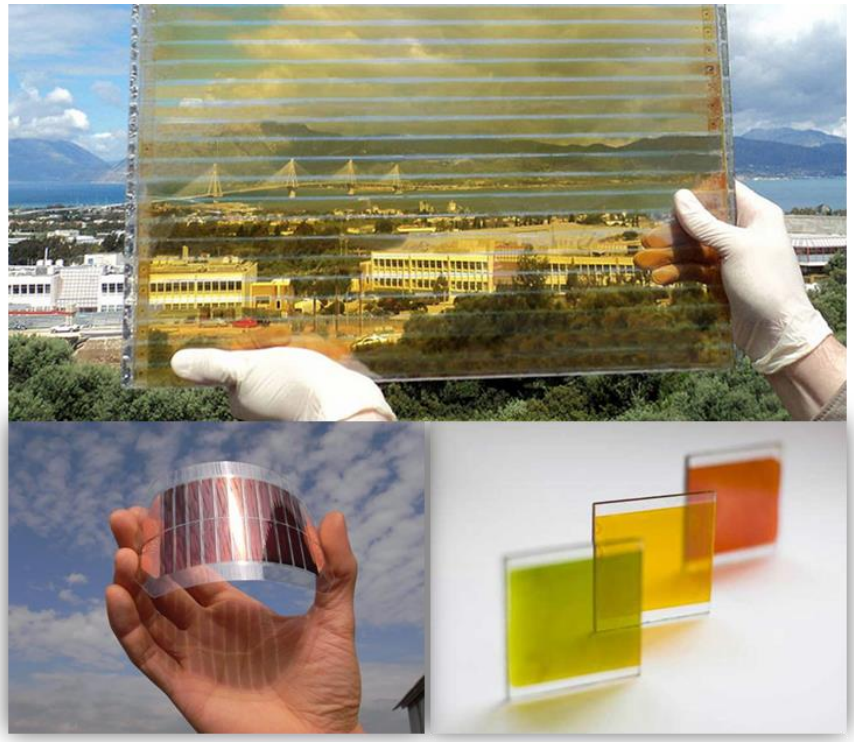

Figure 14. Transparent, flexible and multi-colour third generation solar cells [43]

5.6.1. Organic Solar Cell

A typical organic photovoltaic device consists of one or several photoactive materials sandwiched between two electrodes. Figure 15(a) depicts a typical bilayer organic photovoltaic device. In a bilayer OPV cell, sunlight is absorbed in the photoactive layers composed of donor and acceptor semiconducting organic materials to generate photocurrents. The donor material (D) donates electrons and mainly transports holes and the acceptor material (A) withdraws electrons and mainly transports electrons [44]. As depicted in Figure 15(b), those

photoactive materials harvest photons from sunlight to form excitons, in which electrons are excited from the valence band into the conduction band (Light Absorption). Due to the concentration gradient, the excitons diffuse to the donor/acceptor interface (Exciton Diffusion) and separate into free holes (positive charge carriers) and electrons (negative charge carriers) (Charge Separation). A photovoltaic is generated when the holes and electrons move to the corresponding electrodes by following either donor or acceptor phase (Charge Extraction) [45].

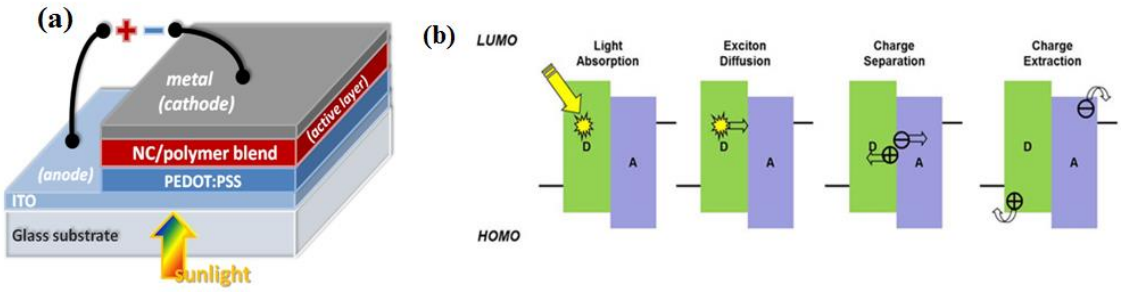

Figure 15. Schematic representation of (a) a typical bilayer organic photovoltaic device and (b) electricity generation [46] [47]

A primary advantage of OPV technology over inorganic counterparts is its ability to be utilized in large area and flexible solar modules, specially facilitating roll-to-roll (R2R) production. Additionally, manufacturing cost can be reduced for organic solar cells due to their lower cost compared to silicon-based materials and the ease of device manufacturing. However, to catch up with the performance of silicon based solar cells, both donor and acceptor materials in an OPV need to have good extinction coefficients, high stabilities and good film morphologies. Since the donor plays a critical role as the absorber to solar photon flux, donor materials require wide optical absorption to match the solar spectrum. Another basic requirement for ideal donor/acceptor is a large hole/electron mobility to

maximize charge transport [48]. The significant improvement of OPV device performance has been accomplished by introducing various OPV architectures, such as bulk-heterojuction (BHJ) and inverted device structures, and developing low band gap conjugated polymers and innovative organic small molecules as donor materials.[46]

As DSSCs are the major focus of this work, they will be covered in more detail including the device architecture, working principle, research trend, applications in different sectors and different challenges in commercialisation are discussed in the upcoming sections.

5.7. PV technologies: A state-of -the-art

Table 1 summarizes the state-of-the-art for the different photovoltaic technologies.

Table 1. Types of single-junction terrestrial cell and submodule efficiencies measured under the global AM1.5 spectrum (1000 W/m^2) at 25°C (IEC 60904-3: 2008, ASTM G-173-03 global) [22]

Type of solar cell		**PCE (%)**	**Active area (cm^2)**	**V_{oc} (V)**	**J_{sc} (mA/cm^2)**	**FF (%)**
First Generation						
Silicon	**Crystalline cell**	26.7 ± 0.5	79.0	0.738	42.65	84.9
	Multicrystalline cell	22.3 ± 0.4	3.92	0.67	41.08	80.5
	Sub-module	21.2 ± 0.4	239.7	0.687	38.50	80.3
	GaAs (cell)	28.8 ± 0.9	0.99	1.122	29.68	86.5

III-V cells	**GaAs (multicrystalline cell)**	18.4 ± 0.5	4.01	0.994	23.2	79.7
	InP (crystalline cell)	24.2 ± 0.5	1.00	0.939	31.15	82.6
Second Generation						
CIGS	**Cell**	22.9 ± 0.5	1.04	0.744	38.77	79.5
CdTe	**Cell**	21.0 ± 0.4	1.0623	0.875	30.25	79.4
CZTS	**Cell**	10.0 ± 0.2	1.113	0.708	21.77	65.1
Silicon	**Amorphous cell**	10.2 ± 0.3	1.001	0.896	16.36	69.8
	Thin film mini-module	10.5 ± 0.3	94.0	0.492	29.7	72.1
Third Generation						
Perovskite	**Cell**	20.9 ± 0.7	0.991	1.125	24.92	74.5
	Mini-module	17.25 ± 0.6	277	1.070	20.66	78.1
	Sub-module	11.7 ± 0.4	703	1.073	14.36	75.8
Dye-sensitised	**Cell**	11.9 ± 0.4	1.005	0.744	22.47	71.2
	Minimodule	10.7 ±0.4	26.55	0.754	20.19	69.9
	Sub-module	8.8 ±0.3	398.8	0.697	18.42	68.7
Organic	**Cell**	11.2 ± 0.3	0.99	0.780	19.30	74.2
	Mini-module	9.7 ± 0.3	26.14	0.806	16.47	73.2

5.8. Dye sensitised solar cells (DSSCs)

The invention of the dye-sensitised solar cells has opened new prospects to the photovoltaic applications. The structure, working principle, different types, charge transport mechanism, efficiency limitations and research progress are discussed in this section.

5.8.1. Structure and working principle

The conventional dye-sensitised solar cell (DSSC), first reported in 1991 by O'Regan and Grätzel, takes its inspiration from the natural process of photosynthesis [49]. The structure of a dye sensitised solar cell mainly consists of three major components, namely: the working electrode which is usually a dye molecule coated nanocrystalline porous oxide film (usually TiO_2) deposited on a transparent conductive oxide coated substrate, the counter electrode which is often a platinum-coated TCO deposited substrate and an electrolyte containing usually an I^-/I_3^- redox couple. Figure 16 illustrates the components in a typical DSSC [50].

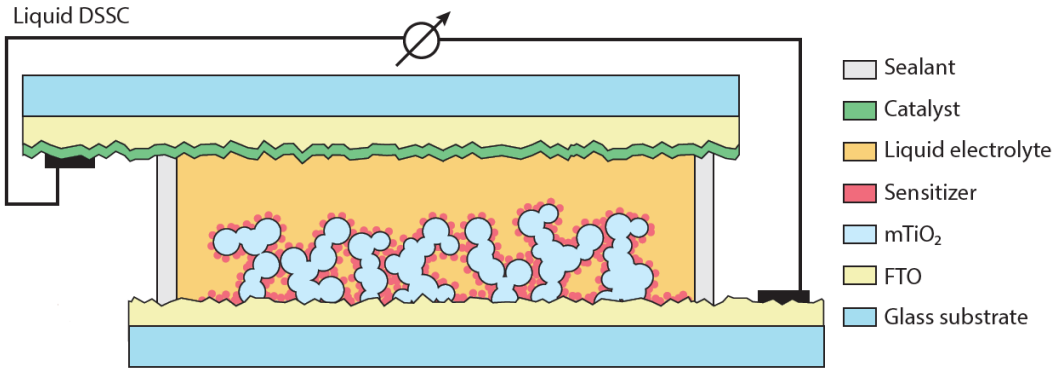

Figure 16. Schematic representation of the device configuration for a liquid DSSC [25]

The working principle of the DSSC is based on the absorption of photons and excitation of the dye, followed by fast electron injection in to the conduction band (CB) of the TiO_2 surface. Dye molecules absorb the incident photons and get excited from a low-energy state (HOMO) to a high-energy state (LUMO). The excited state of the dye molecule is capable of injecting electrons in to the CB of the TiO_2 particle [51]. The oxidized dye is then regenerated and becomes ready for the next excitation by obtaining electrons from the redox electrolyte converting

iodide (I^-) into tri-iodide (I_3^-). The electrons injected to the CB of TiO_2 percolate through the TiO_2 particles in the film until they are collected at the TCO contact of the photoelectrode and are fed into the external circuit. The tri-iodide species (I_3^-) are converted back to iodide (I^-) via the platinum catalyst at the counter electrode by the electrons travelled through the external circuit [50]. Dssc working mechanism is given below,

$Dye + photon \rightarrow Dye^*$ (Excitation process)

$Dye^* + TiO_2 \rightarrow e^-_{(TiO_2)} + Dye^+$ (Injection process)

$e^-_{(TiO_2)} + C.E \rightarrow e^-_{(C.E)} +$ electrical energy (Energy generation)

$Dye^+ + \frac{3}{2} I^- \rightarrow Dye + \frac{1}{2} I_3^-$ (Dye regeneration)

$\frac{1}{2} I_3^- + e^-_{(C.E)} \rightarrow \frac{3}{2} I^- + C.E$ (Electron regeneration)

5.8.2. Charge Transport in DSSC

As discussed earlier, energy level and device operation of DSSCs is given in Figure 17. The sensitizing dye absorbs a photon (energy hv), the electron is injected into the conduction band of the metal oxide (titania) and travels to the front electrode. The oxidized dye is reduced by the electrolyte, which is regenerated at the counter-electrode (not shown) to complete the circuit. V_{OC} is determined by the Fermi level (E_F) of titania and the redox potential (I_3^-/I^-) of the electrolyte [52].

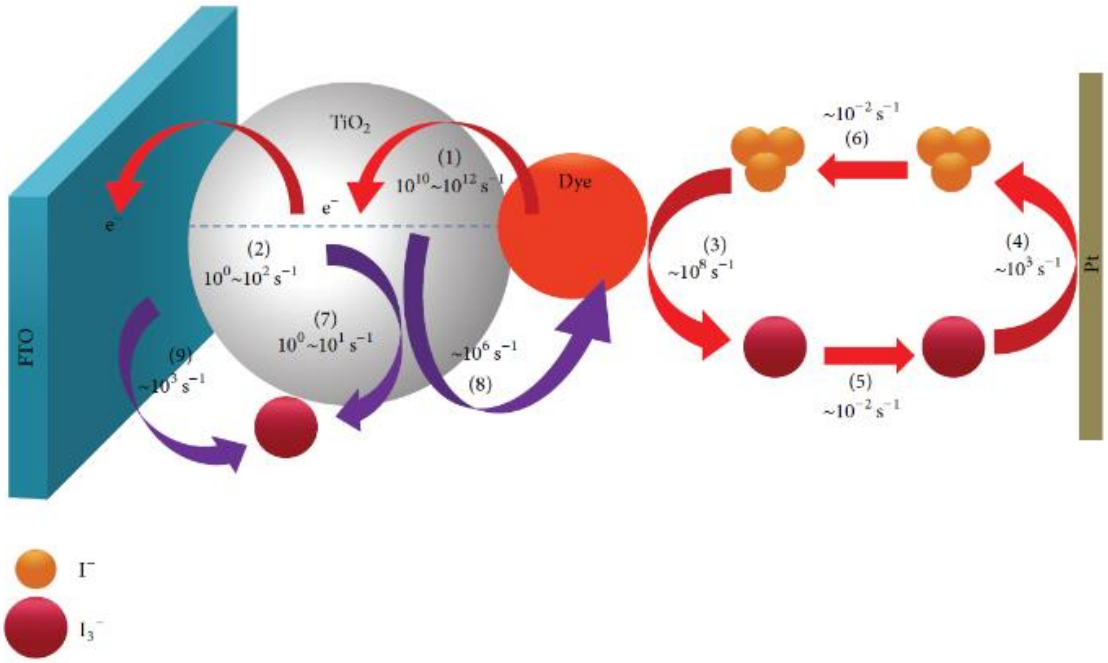

Figure 17. Charge transfer kinetics in DSSC [53]

The electron injection from Ru-sensitiser into the TiO_2 conduction band is taken place in femtoseconds up to 150 picoseconds, compared with decay of excited state of the dye to the ground state, which is given by the excited state lifetime of the dye, typically 20-60 ns for Ru-based DSSCs. The regeneration of the oxidized dye by the electron donor (mostly iodide in electrolyte) is in the microsecond time domain. For a turnover number, that is, the cycle life of the sensitiser in the DSSC device, to be above 10^8, which is required for a DSSC lifetime of 20 years in outdoor conditions, the lifetime of oxidized dye must be >100 s if the regeneration time is 1 µs. The back-electron-transfer process (recombination via dye) from the conduction band of TiO_2 to the oxidized sensitiser occurs on a microsecond to millisecond time scale [54], due to the electron density in the semiconductor and thus the light intensity. Recombination of electron in TiO_2 via acceptors in electrolyte (tri-iodide) is normally referred to as the electron lifetime, which is very long (1-20 ms under 1-sun light intensity)

for iodide/triiodide system compared with other redox system used in DSSC, explaining the success of this redox couple.[16]

5.8.3. Solid-state DSSC

In the solid-state counter part of the DSSC, the liquid electrolyte of the conventional liquid based DSSC is replaced by a solid-state hole-transport material (HTM) and as a result of there are some structural differences in the device design (see Figure 18). The basic principles of device operation remain identical, where the oxidized dye is regenerated by hole injection into the solid HTM, which transports the holes to the back contact completing the external circuit.

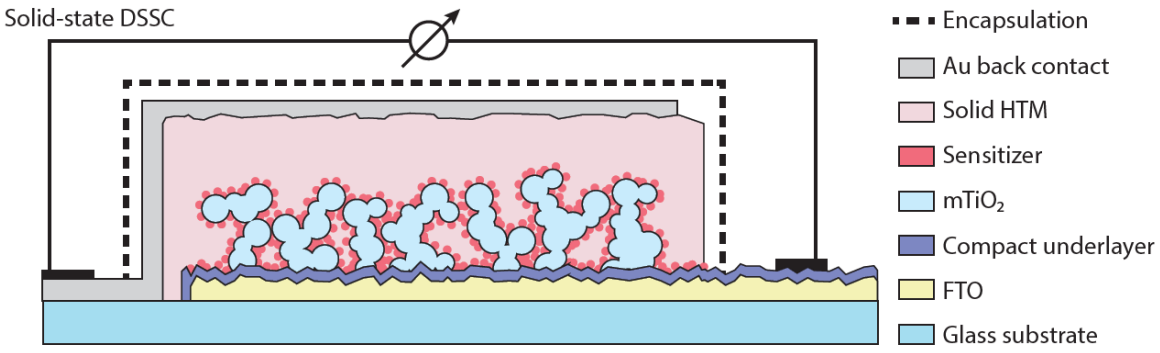

Figure 18. Schematic representation of the device configuration for a solid-state DSSC [25]

Unlike a liquid DSSC which has a sandwich configuration between two separate TCO substrates as electrodes, ssDSSCs are based on a monolithic design built on a single TCO substrate with the back contact deposited by thermal evaporation of silver or gold directly on the solid HTM layer. An additional advantage of separating the processes of light absorption and charge separation from charge-transport has allowed the individual components making up the DSSC to be optimized and improved. This has lead to significant improvement in the solar-to-electrical power conversion efficiencies (PCE) of devices over the

years as a direct result from the Implementation of new and tailored materials [25]. For the conventional DSSC configuration, the highest PCE of 12.3% have been achieved so far. DSSCs with different architectures have been made and their landmarks are given in the Figure 19.

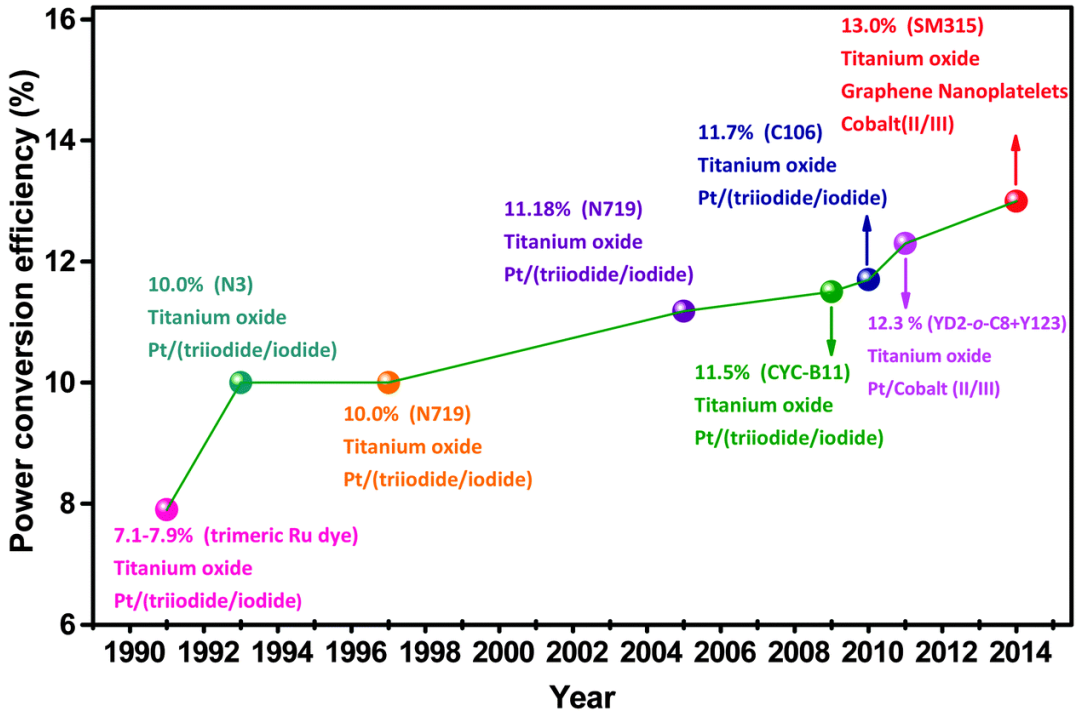

Figure 19. Different laboratory scale DSSCs and their landmarks [55]

5.8.4. Flexible DSSCs

Although DSSCs fabricated on TCO coated glass have achieved efficiencies over 12%, there is a great deal of interest in cheaper, flexible solar cells using transparent indium tin oxide (ITO) coated plastic (usually polyethylene naphthalate (PEN) and polyethylene terephthalate (PET)) and thin metal foil based substrates in place of the glass [50]. Table 2 demonstrates flexible DSSCs configurations and their performance. Liquid and quasi solid electrolytes have been used for the fabrication of flexible devices. Moreover, different substrates such as Ti foil, PEN, and Stainless steel have been used and their power

conversion efficiencies have been reported as 7.2%, 8.1% and 8.3% respectively (Table 2).

Table 2. Flexible DSSCs with their performance parameters

Device configuration	**Electrolyte**	**Solar Cell Parameters**				**Ref.**
		J_{sc} [mA/cm^2]	**V_{oc} [volts]**	**FF [%]**	**PCE [%]**	
Ti/TiO_2/N719/electrolyte/ Pt/ITO	redox iodide electrolyte	13.6	0.78	68.0	7.2	[56]
PEN/ITO/TiO_2/N719/ electrolyte/Pt/ITO	redox iodide electrolyte	14.5	0.75	75.0	8.1	[57]
StS/ITO/TiO_2/N719/ electrolyte/Pt/ITO	redox iodide electrolyte	16.4	0.75	67.9	8.3	[58]
PET/StS/TiO_2 nanoparticle/dye/ TiO_2 fiber/electrolyte/ PPy nanoparticle/StS foil	gel electrolyte	5.1	0.74	73.0	2.8	[59]

5.8.5. Efficiency limitations of DSSCs

The theoretical maximum of output photovoltage, V_{OC}, in typical DSSCs is determined by the potential difference between the conduction band bottom of semiconductor photoelectrode and the potential of the redox species in electrolyte. In the case of TiO_2 and iodide/tri-iodide, this energy difference is near

0.9 V. An overpotential of 0.2 V is believed to be least for an efficient injection of electron from exited dye into the conduction band of TiO_2 film, and another 0.3 V over-potential is estimated for the regeneration of the oxidized dye [60]. Hence the energy gap of the dye greater than 1.4 eV can provide a sufficient driving force for the generation of high J_{SC}. Supposing 90% of the incident photons with energy larger than the energy gap are absorbed, J_{SC} of 30 mA/cm^2 could be achieved and an energy conversion efficiency of 18% is expected to be obtained by current available technology to realize V_{OC} of 0.8 V and FF of 0.75, simultaneously [61]. For further improvement of the efficiency, one way is to develop tandem DSSCs by tuning each junction to convert UV-visible light and NIR light into charges, respectively, which can utilize high-energy photons more efficiently.

5.8.6. DSSC research trend

Since 1991, different DSSCs have been tried with different components to improve the efficiency, cost effectiveness and long-term stability. It can be seen from the Figure 20 that a rapid increase in number of publication since its introduction in 1991. Especially in this decade, the scientific community has realised the multifunctional applications of DSSCs.

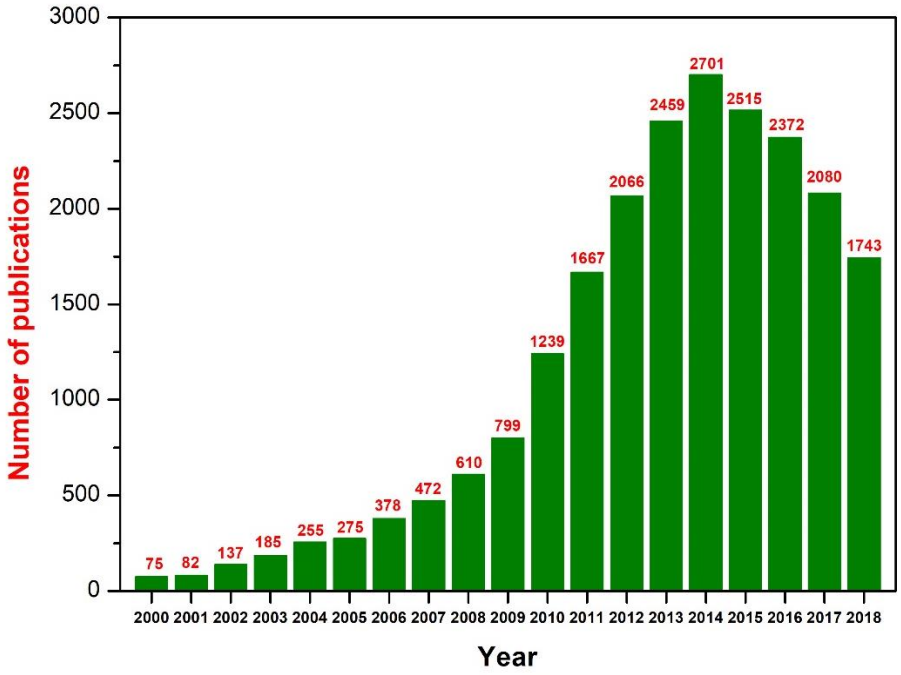

Figure 20. A statistical graph of the number of publications related to the DSSCs per year since 2000 (*2018- till 17th December). Data were obtained from the web of knowledge using the keyword “dye sensitised solar cells”)

Research is still intensive with several research groups working in the fields of electrical, chemical, material, and metal engineering in order to find the proper set of materials and the best DSSC architectures [61]. Despite the commercialisation of DSSCs, still there are issues need to be solved to make this cost-effective technology more competitive with other generation PV technologies in the market. For that reason, these devices need to be studied for more applications, one such application is building integrated photovoltaics.

The advantage of transparent DSSCs over opaque cells is, these transparent DSSC modules can be used for building integrated applications to provide electricity and daylighting simultaneously. A semi-transparent PV material is used for the windows to allow natural lighting while keeping the solar gain low.

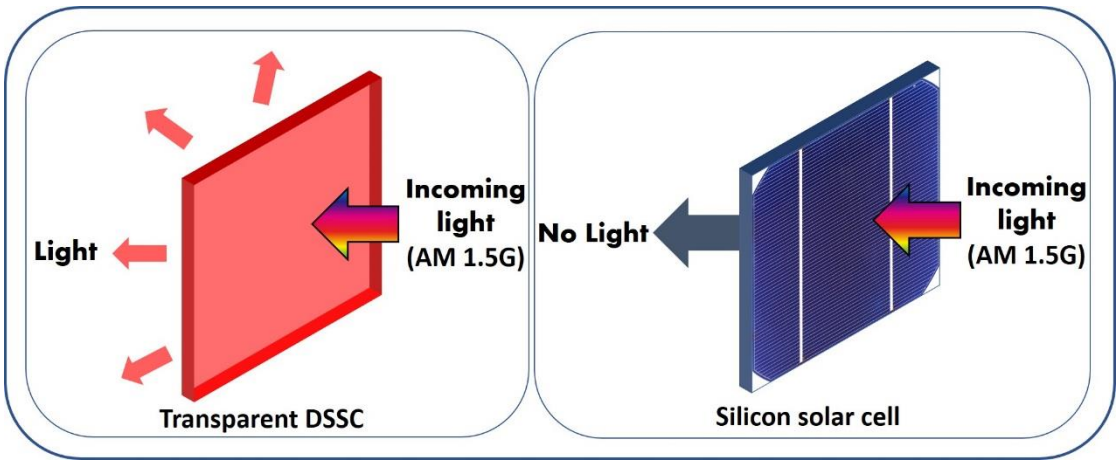

Figure 21. Schematic illustration of the advantage of transparent dye-sensitised solar cell over silicon solar cell

5.9. Building integrated photovoltaic technologies

PV systems used on buildings can be classified into two main groups: building-applied PVs (BAPVs) and building integrated PVs (BIPVs).

5.9.1. Building applied photovoltaics

BAPV systems are regular solar cell systems that are generally installed on top of roofs. BAPVs are added to a building and have no direct effect on the structural functions [62]. Moreover, the BAPV panels make the buildings lose their aesthetics and they mask the beautiful of the building design. Figure 22 shows an example of BAPV systems. The amount of electricity production is reduced due to the limited roof space. To overcome these challenges, the systems which could be integrated into the building architecture have been identified. These systems are known as building integrated photovoltaics (BIPV). The overall cost of installing BIPV system is lower to a typical PV system [63].

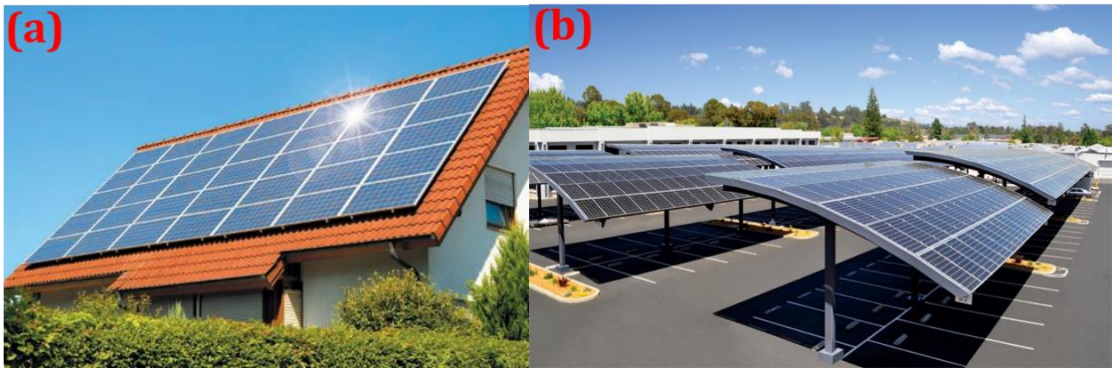

Figure 22. Building Applied Photovoltaic systems (BAPV) [64]

5.9.2. Building integrated photovotovoltaics

The general principle of Building Integrated Photovoltaics (BIPV) is that PV modules are integrated into the building envelope, substituting standard glass and other cladding materials with glass/glass laminates encapsulating PV cells within. These BIPV modules generate electricity at the 'point of use' thereby maximizing energy efficiency and eliminate transmission losses. The electricity generated using this system is directly feed into the building, making the source of energy the sole point of its consumption. However, they stand a very tough competition from the standard silicon panels. Any increase in the electricity prices improves the viability of semi-transparent photovoltaic systems. By becoming an integral part of the building architecture BIPV can enhance the building energy efficiency through electricity generation but also can provide daylight transmission and improve the thermal properties of the building facades [65].

The key features expected of a Building Integrated Photovoltaic system include:

- Natural integration in the building architecture
- Modularity
- Aesthetically pleasing design
- Conformity with building design and standards

BIPV systems can be integrated into different building architectures these include windows, vertical glazing, canopies, green houses, curtain walls, roofs, window awning, etc. The use of BiPV systems has several advantages and are as follows:

- Reduction in the investment for displacing the façade
- Requires little or no energy storage as the point of electricity generation becomes the point of consumption
- Embeds into the building architecture and therefore minimises any land use
- Can form part of communication system for cellular communication
- Improves the thermal insulation

The potential market for Building Integrated Photovoltaics is both new constructions and refurbishment of existing buildings by retrofitting. The flexibility and modularity BIPV products offer makes it easy for them to be applied in any kind of building architecture. There is a great need of glass for the growing photovoltaic industry [66].

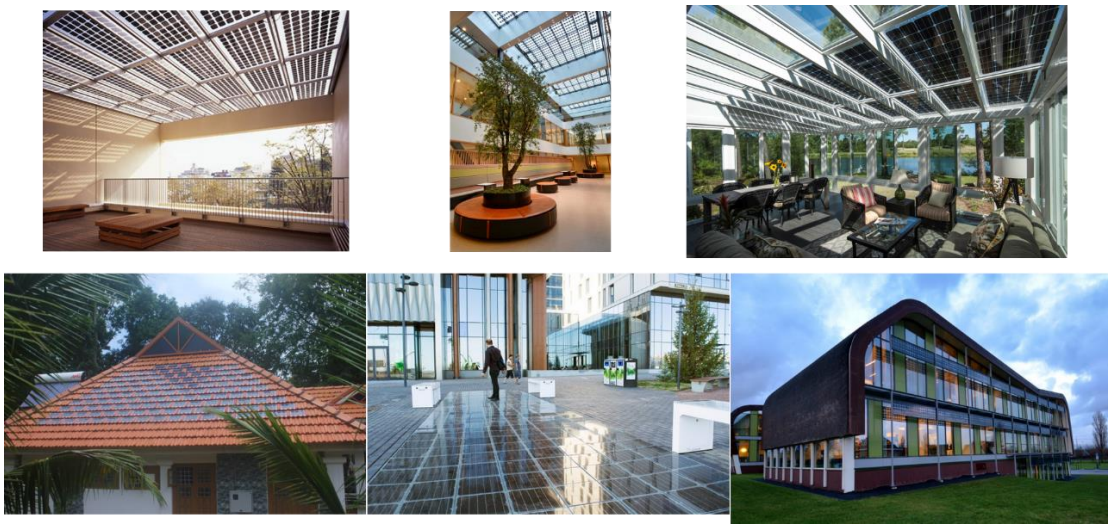

Figure 23. Different types of BIPV architectures [67–72]

Among the various BIPV products, BIPV windows have been proposed as an emerging technology for use in the construction industry [63,73,74].

5.9.3. Building-Integrated Photovoltaic Windows (BIPW)

Building-Integrated Photovoltaic Windows (BIPW) are expected to be an innovative glazing technology, which apart from electricity production, are linked with the building heating or cooling loads and artificial lighting [75]. The solar cell application in BIPV windows can be divided into two types. The first is to make BIPV windows using a non-transparent solar cell. In such a case, there is a method for producing BIPV windows with a spacing between solar cells to achieve transparency. Secondly, there is a method of fabricating BIPV windows using a cell with light transparency [76].

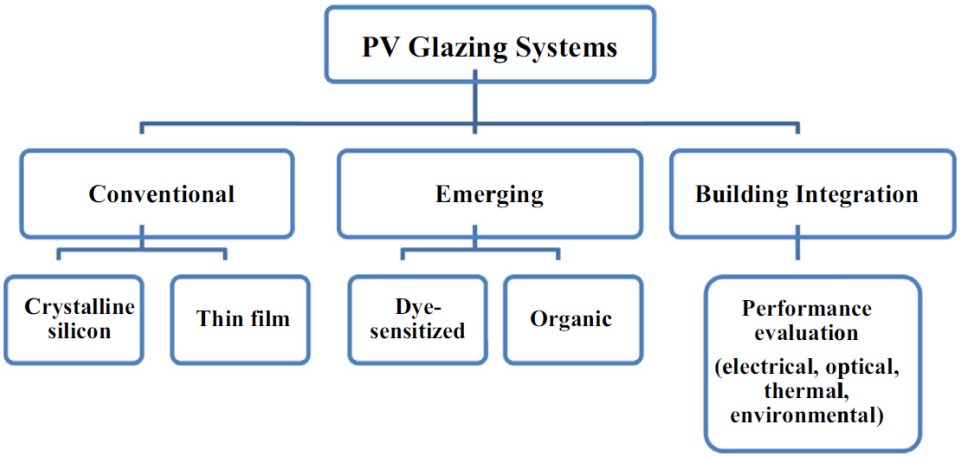

Figure 24. PV glazing systems in building integration [77]

5.9.4. Limitations in current BIPW materials

For glazing application, semitransparency is a precondition [78], as natural daylight penetrating through this semi-transparent PV makes the indoor environment comfortable. Available PV types for glazing application include crystalline silicon, CdTe, a-Si, CIGS, DSSC and perovskite. c-Si has higher absorption which restricts light to pass through. There are many studies in the

literature where c-Si PV was used to replace traditional glazing at homes or buildings. Since these cells are typically opaque, there are also important compromises in terms of lighting (shadows in the building interior) and limited external view [77,79–81]. Regular distribution of opaque c-Si can offer daylighting, however this structure blocks the natural viewing [82]. Thin film second generation CdTe [83], a-Si [84] and CIGS are other options for PV glazing application. With thin film incorporation in a glass–glass construction, commercial products with a transparency up to 50% are available in the market. The introduction of this technology provided more homogeneous daylighting of the interior spaces compared to crystalline solar cells. However, light induced defects, shortage and toxicity of materials used in a-Si, CIGS, and CdTe technologies have limited the opportunity to apply them in glazing application [85]. Moreover, the power conversion efficiency is connected to its visual transmittance and therefore extensive performance optimization should be considered [86–88].

5.9.5. Advantages of DSSC glazing

Third generation DSSC is a potential candidate for BIPV applications due to the following advantages,

- DSSCs are insensitive to environment contaminants, which offer them to prepare under ambient temperature. Thus, easier fabrication process can be adopted such as roll-to-roll, which involves continuous, low-cost manufacturing method to print dye-sensitised solar cells on flexible substrates [89–91].
- DSSCs work even in low light (400-800 W/m^2)conditions. Thus for northern latitude area where diffuse sun lights are majority over direct sunlight,

DSSC based windows are excellent choice for building applications [89–93].

- DSSCs are superior than a-Si:H based PV as the transparency can be increased by making use of highly transparent photoanodes and counter electrodes. Selecting proper dyes for these devices can provide low eye sensitive factor [94–96].
- DSSCs have positive temperature effect [97,98].

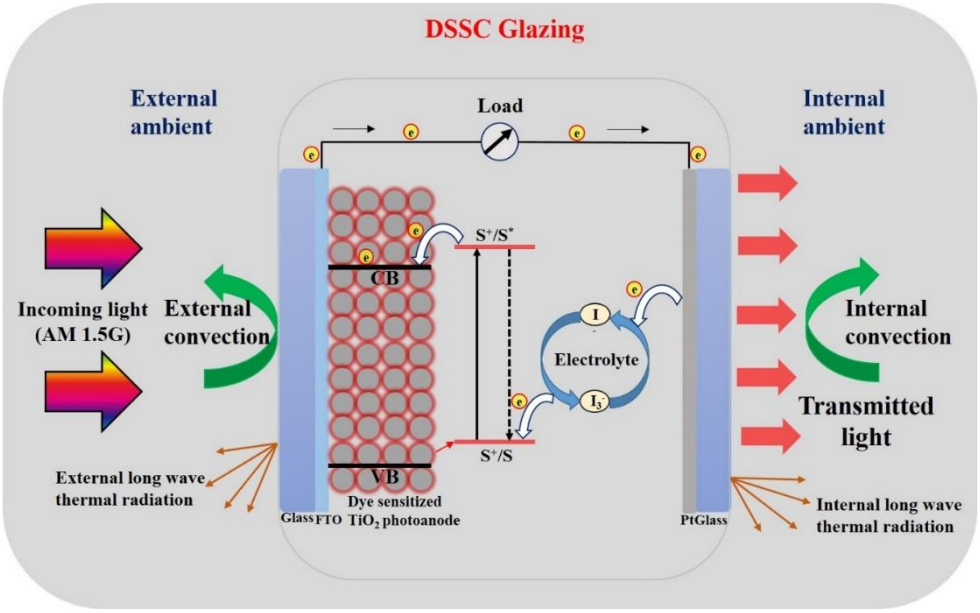

Figure 25. Schematic representation of DSSC glazing

While many research groups investigate the working principles of DSSCs and new developments have been achieved concerning their efficiency and large-scale applications, new companies founded in the meanwhile try to carry DSSC technology in market place evaluating all process steps are needed for industrial production.

5.9.6. Recent progress in DSSC glazing

The first report on scale-up of the DSSC was in 1996 by Gratzel's group, in which they reported a solar mini-module with a total surface area of 21.06 cm^2 and an efficiency of 5.65% with respect to its active area [99]. There are various reports on reproducibility, stability, TiO_2 deposition methods, and configuration of solar modules as mentioned earlier.

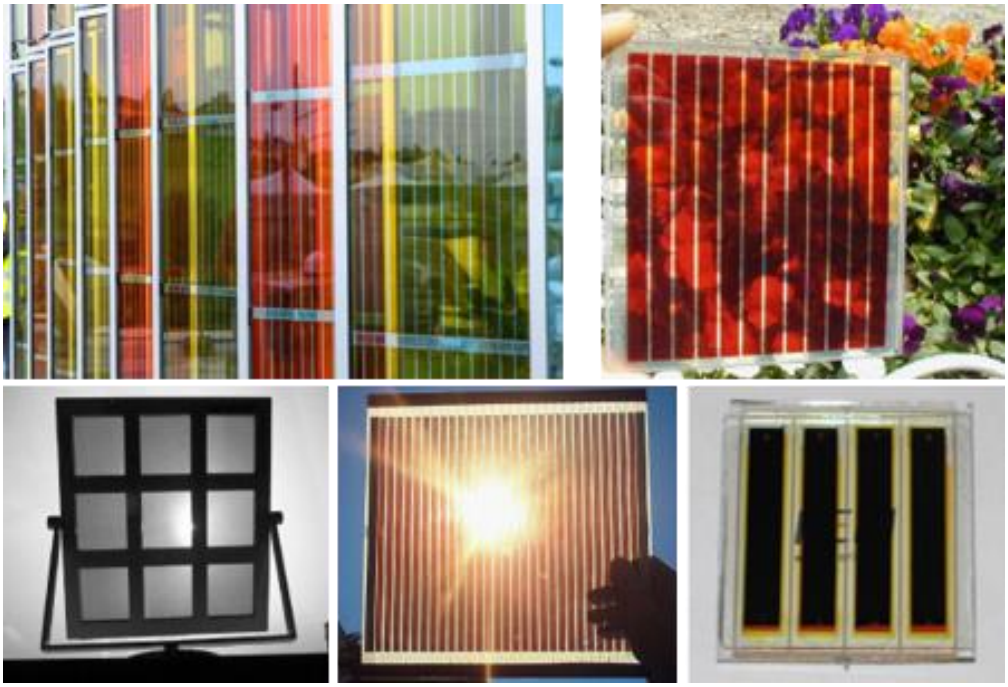

Figure 26. Previously investigated DSSCs for BIPV windows [100–104]

First ever DSSC glazing was fabricated by series connected 9 unit (80× 80 mm^2 active area) solar cells which offered 60% average transmission between 500-900 nm [101]. Thermo-optical behaviour of DSSCs made of green and red dyes were investigated using WINDOW software, which showed 60% reduction of solar gain [105]. Thermo-opto-electrical characteristics of DSSC were investigated by Zemax, WINDOW and COMSOL softwares [106]. To evaluate the occupant comfort due to the colour property of transmitted solar light, correlated colour temperature and colour rendering index for DSSC glazing was evaluated [107]. Recently, DSSC glazing was monitored for two years in outdoor

exposure at Hanbat National University, Republic of Korea (36.20° N, 127.18° E), showed promising outcomes [108]. Another outdoor experiment was also performed to study the thermal performance for DSSC glazing which showed overall heat transfer coefficient and solar heat gain coefficient for this glazing were 3.6 W/m^{2}K and 0.2 respectively [109].

Most recently, an analysis of the power performance and the power generation characteristics of DSSC (Dye-Sensitised Solar Cell) BIPWs applied to a full-scale mock-up at two different installation angles was conducted by Hyo Mun Lee et.al. [108]. It was found that, the power performance of the DSSC module was similar to that of general PV (Photovoltaic) systems. On the other hand, it showed lower power efficiency than the a-Si, c-Si, or CIGS modules. Therefore, DSSC requires more installation area to have the same power generation as other solar cells.

Figure 27. Power performance analysis of a transparent DSSC BIPV window based on 2-year measurement data in a full-scale mock-up [108]

5.9.7. Colour properties of glazing

Spectral power distribution (SPD) of solar radiation in the visible range of 380 nm to 780 nm is considered as daylight. SPD of natural daylight changes with local latitude, weather, season, time of day, air bound dust and pollutant [110]. SPD of transmitted light into the interior of a room influence the visual comfort and colour perception. Glazing transparency, thickness, solar heat gain coefficient and overall heat transfer coefficient are the most common investigated parameters while colour properties such as correlated colour temperature and colour rendering index evaluations are often overlooked.

Colour of transmitted daylight through glazing is an influential factor on indoor comfort. Correlated colour temperature and colour rendering index are the two major components to understand the SPD of transmitted light through glazing [111,112]. CCT and CRI are the most aesthetic criteria as they show whether the spectrum coming inside through the glazing is suitable for occupant or cross the comfort level. They are used to characterize the illumination quality of white light [113]. Good quality lighting is an important feature, as the quantity and quality of lights are required for wellbeing, health, interpersonal relationships and aesthetic taste [114,115]. CRI of a glazing indicates the colour of entering daylight into an interior before and after placing a glazing. CRI values can be from 0 to 100 [116] where between 80 and 90 are considered to be acceptable [117]. CRI close to 100-represents true colour perception inside the building, thus, indicates perfect visual quality [118,119]. A CCT needs to be equivalent to that of a blackbody source at temperatures between 3000 and 7500 K [120]. CCT offers to understand whether light is neutral, bluish white or reddish white. CCT for various daylight sources are listed in Table 3.

Table 3. Correlated colour temperatures for various daylight sources of Washington DC USA [121].

Daylight source	**CCT (K)**
Sunlight – sunrise or sunset	2,000
Sunlight – one Hour After Sunrise	3,500
Sunlight – early Morning	4,300
Sunlight – late Afternoon	4,300
Overcast sky	6,000
Summer skylight	9,500 to 30,000

The spectrum of transmitted daylight into an interior space changes due to the presence of DSSC glazing. CRI and CCT characterization of DSSC glazing is required as these parameters assess human response to colours [110]. For glazing, transmission is a dominant parameter which is not constant but varies with solar incident angle. The incident angle of sunlight varies with the time of day and season. Therefore, building integrated vertical plane DSSC glazing's transmission is significantly different from their normal incidence value. For building energy simulation, this variable transmission evaluation is essential to predict accurate energy saving calculation. Glazing transmittance also has a

strong correlation with clearness index, and knowing this value helps in building energy calculation. To evaluate clearness index, the only measured parameter is global horizontal solar radiation. As DSSC is considered to be in wide future as one of the future PV glazing materials, its angular transmission behaviour variation with clearness index evaluation is essential. [122].

Table 4. Examples of the developed DSSC modules for window applications

DSSC module type	**Transparency (%)**	**Module performance (%)**	**Active area**	**Benefits**	**Issues**
Nine cells in series[101]	60	-	64 cm^2	maximum transmittance of 67%	Poor fillfactor
Twenty-nine cells in series [100]	Semitransparent	3.5 PCE	505.5 cm^2	Cost effective	Loss in efficiency/ Sealing issue
Manual screen printing (Plain type) [123]	Opaque	1.02 PCE	12.25 cm^2	Easy process, Low cost	Low efficiency
Series interconnected module of 12 cells [102]	Semitransparent	12x larger V_{oc} than a single cell	90.25 cm^2	High stability up to 2000h	-

Glass frit-sealing technology - a facade panel based on DSSC [124]	Semitransparent	4.5% PCE	672cm^2	Successful in outdoor test	Low FF and photocurrent density

There are challenges to overcome but the potential benefits are worth the efforts. One of those common challenges found from the literature is scaling up of DSSCs.

5.10. Challenges in scaling-up of DSSCs

Experimental results for small size solar cells cannot directly applied in large scale DSSCs as the efficiencies measured for small size solar cells cannot be repeated in large scale [125]. Several research groups have tried to overcome the challenges of DSSC industrialization,

Below are referred some of the main issues which have to be taken into account before DSSCs go to a production line [125] :

- Large area deposition of TiO_2 layers. The layers have to be homogeneous and uniform.
- New methods for dye staining and electrolyte filling.
- Electrical interconnection of individual cells. A major factor for limited efficiency of the DSSC is the ineffective contacts on FTO glass. The external connections of the individual cells are also a problem.
- Sealing process for modules in case of liquid electrolytes.

- Long-term stability of at least 10 years for outdoor use.
- Evaluation costs, which is believed to be approximately 10% of that needed for silicon solar cells.

Therefore, in order to apply the BIPV system to the elevation of a building, performance loss should be reduced by considering a method that can avoid reducing transparency of the system. An effective way to improve the performance of such systems is to concentrate the incoming light.

5.11. Building integrated concentrating photovoltaics (BICPV)

Concentrating photovoltaic (CPV) systems make use of optical components which concentrate the incoming sunlight and focus it on solar cells. The concentrated light reaching the solar cell magnifies the production of energy several times. These optical components often referred to as concentrators, make use of reflective/ refractive principles of optics, individually or in combination for concentrating the sunlight. Incorporating the concentrating photovoltaics into any part of the building architecture is referred to as building integrated concentrating photovoltaics (BICPV) [65].

5.11.1. Reflecter based concentrator system

Low concentration photovoltaic modules use mirrors to concentrate sunlight onto a solar cell. Often, these mirrors are manufactured with silicone-covered metal. This technique lowers the reflection losses by effectively providing a second internal mirror. The angle of the mirrors depends on the inclination angle and latitude as well as the module design, but is typically fixed. Figure 28 shows a simple V-shaped trough inclined at a certain angle. Some part of energy is lost from the incoming light when the reflecting mirrors redirect the light to the solar

cell. This is commonly specified as specular loss. Based on this concept, several CPV systems have been developed.

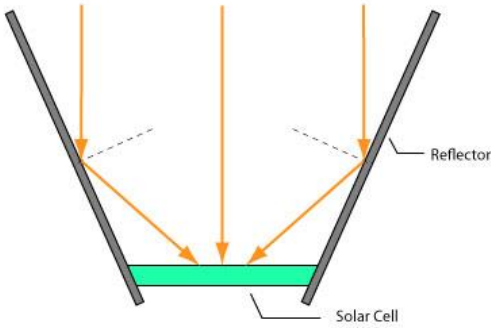

Figure 28. Reflective optics concept of CPV system [126]

5.11.2. Classification of CPV systems

The most common classification of CPV modules is by the degree of concentration, which is expressed in number of "suns". E.g. "3x" means that the intensity of the light that hits the photovoltaic material is 3 times than it would be without concentration [126].

Table 5 Classification of CPV systems basen on the degree of concentration

	Low concentration	**Medium concentration**	**High concentration**
Degree of concentration	2-10	10-100	>100
Tracking need	No tracking	1-axis tracking	Dual axis tracking
Cooling need	No cooling	Passive cooling	Active cooling
PV material	Crystalline Si	Silicon/thinfilm	Multijunction cells (InGaP)

5.11.3. Development of concentrator systems for BIPV

In the last few decades number of such applications have been demonstrated using silicon solar cells [127–129]. But there have been little studies carried out on the influence of concentrating light on the DSSC performance. The application of an optical lens-based solar concentrator system mounted on top of DSSCs still poses several challenges in terms of efficiency, cost-effectiveness of optical design, and the provision of uniform and concentrated illumination on a DSSC [130]. Furthermore, various complex phenomena including light scattering, recombination of electron-hole pairs, and dye degradation in the photoactive layers of DSSCs can occur when the intensity of incident light is increased by a solar concentrator [131].

Figure 29. Current BICPV technologies (a) solar CPV farm and (b) recently designed solar squared glass block [132,133]

5.11.4. Concentrating systems for DSSC

A considerable amount of research has been conducted recently on increasing the electrical efficiency of DSSCs and their modules [134–136]. Moon et al. [137] employed concentrated illumination using a condenser lens up to 3.72 suns on a DSSC and it was found that an increase in photocurrent and efficiency values. Choi et al. [138] used condenser lens for a vertical stacked- cell

configuration DSSC in to increase the efficiency and at 8 mm separation distance between the lens and the cell, the device efficiency increased from 2.5% to 8.3%. Barber et al.[139] proposed a concentrator for a hybrid silicon-DSSC system with two different optical filters for visible and IR absorption to achieve about 20% efficiency. More recently, Sacco et al.[140] demonstrated the application of a solar concentrator both in indoor and outdoor working conditions. The outdoor results show a linear behaviour for solar concentration factors up to 1.5. However, the LCPV has not been used on DSSC before.

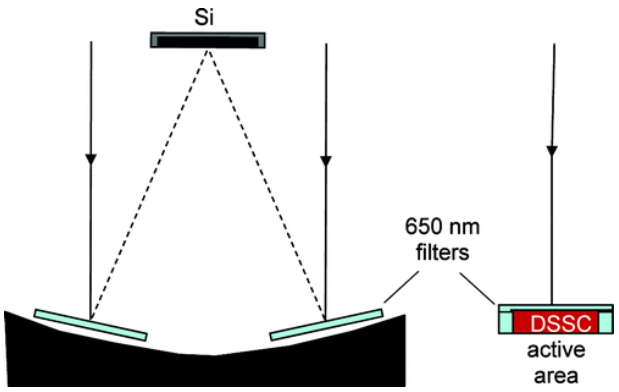

Figure 30. Hybrid concentrator arrangement used in outdoor testing by Barber et.al [139]

Based on the knowledge acquired from the literature, it was found that the concentrator system could be coupled on the DSSC to improve the performance of the device to solve the scale up issue for building integrarated applications.

5.12. Research question

Considering the knowledge gaps identified in the literature, A few major research questions were raised as follows:

- Can DSSCs be used as BIPW material? Can their colour properties be compared to the available commercial glazing materials?
- How much optical concentrators can improve DSSC performance? How does the charge transfer properties change under high light intensity?

This thesis covers several separate disciplines and the structure of the thesis shows the consideration given to each of these and the progression of the work through them.

5.12.1. Structure of the thesis

Chapter 2 provides a detailed account of the materials and methods which were used in the experimental work to fabricate DSSCs. This includes the synthesis and characterization of the new materials, solar cell fabrication and measurement of photovoltaic performance of the devices.

Chapter 3 introduces three simple and low cost approachs for cost effective DSSCs 1. Mesoporous TiO_2 as photoanode material, 2. m-HRD-1 as sensitiser, and 3. CZTS thinfilm as counter electrode. The material properties and PV performance in DSSCs of the new materials are studied and compared with the devices made from commercial materials in this chapter.

Chapter 4 reports the possibilities of using semi- transparent DSSCs as building integrated photovoltaic windows. DSSC glazing transparency, correlated colour temperature and colour rendering index, solar heat gain coefficient, clearness index and daylight glare analysis in different climatic conditions are evaluated and compared with standard double and vacuum glazing systems in this chapter.

Chapter 5 introduces a low solar concentrator with 3× optical concentration and 4× geometrical concentration unit for DSSCs. PV performance, charge transfer parameters of the concentrator coupled transparent devices are investigated and compared with their bare counterparts. Moreover, performance of the low concentrator- DSSC system under low light conditions is also studied.

Chapter 6 offers the summary of the key findings in the present work along with recommendations for the future work.

As this thesis is focused on analysing the nano structured new generation solar cells for building applications and enhancing the device efficiency, findings and contribution from this thesis to this technology will be useful in developing zero energy buildings with low costs and less environmental impacts.

Chapter 2: Experimental methods

This chapter is divided into two parts: the first section introduces the employed materials and their synthesis as well as characterization techniques. The second section describes the device fabrication and its characterization methods. This chapter also lists the equipment used to carry out this work, this includes the software packages as well.

2.1 Materials

All materials were purchased from commercial suppliers and used as received, unless stated otherwise.

2.1.1. Photoanode materials

Substrates

The substrate of the photoanode serves as a collector for the photogenerated electrons and has therefore to be well conducting. It should also form an ohmic contact with the dye adsorbed semiconductor layer but should show a large overvoltage for reduction of the redox electrolyte to minimize the dark current [141]. For this work, Fluorine – doped transparent conducting SnO_2 (FTO) glass substrates obtained from Pilkington (TEC) [142] or Solaronix [143] were used as glass substrates. Substrate glass parameters are given in Table 6.

Table 6. Parameters of the TCO glass used for fabricating DSSCs

Glass code	Thickness (mm)	Resistance (Ω/sq)	Transmission @550 nm (%)
NSG TEC™ A7	2.2	13	82
TCO22-15	2.2	15	81

FTO glass substrates were cut and rinsed in distilled water. The substrates were purified by subsequent sonification in various solvents (1 x Hellmanex® (2 % in water), 2 x ethanol, 2 x DI water, 2 x ethanol) for 15 min in each solvent. Finally, the cleaned substrates were stored in pure ethanol.

TiO_2 pastes

Mostly two types of TiO_2 pastes were used having 20 nm TiO_2 nanoparticles and 400 nm TiO_2 microcrystalline particles respectively as the transparent and the light-scattering layers of the working electrode. Both transparent (18NR-T) and active opaque (18NR-AO) pastes were purchased from Greatcell Solar (Dyesol) Ltd [144].

Figure 31. Transparent (left) and active opaque (right) pastes from Dyesol

In section 3.2, titania paste was prepared and printed on the photoanodes. The following synthesis procedure was used.

TiO_2 nanoparticle synthesis

Titanium isopropoxide (98%), absolute ethanol (99.99%), cetyl trimethylammonium bromide (CTAB), sodium dodecyl sulfate (SDS), α-terpineol, ethylcellulose, tetrabutylammonium iodide (TBAI), iodine, N-methylbenzimidazole (NMB), acetonitrile (ACN) and 3-methoxypropionitrile (MPN) were purchased from Sigma-Aldrich. Dodecyl trimethylammonium bromide (DTAB) was purchased from Fisher scientific.

The mesoporous TiO_2 samples were synthesized using a soft template method with titanium isopropoxide as a titanium source. Various cationic surfactant molecules like CTAB, SDS, and DTAB were used as templates. CTAB, SDS, DTAB, titanium isopropoxide (TTIP) and ethanol were of high pure grade and obtained from Sigma-Aldrich. P25, a commercial titania powder with a grain size of 21 nm was used for comparison purposes. I present here the synthetic methodology for a representative case of CTAB-templated mesoporous TiO_2. A definite weight (3.64 gm) of the cationic surfactant CTAB was taken in a round-bottomed flask and was dissolved in a mixture of de-ionized water and absolute ethanol in a volume ratio of 4:1. To this solution, 14.31 ml of TTIP was added dropwise with continuous vigorous stirring. The resulting gel was then continuously stirred for several hours. The precipitate was then filtered by centrifugation process using water then finally ethanol. The powder was taken out and calcination was done at 450 °C for 5 h to remove the soft template and to increase the cross-linking of the inorganic framework [145]. A similar procedure was followed for the synthesis of SDS and DTAB templated mesoporous TiO_2 in the same molar ratios.

TiO_2 paste preparation

The paste was prepared by the addition of the organic agents α-terpineol as a dispersant, ethyl-cellulose as a binder in synthesised TiO_2 nanoparticles. The exact composition of the paste was as follows: synthesised mesoporous TiO_2 (2g), α-terpinol (1 ml), ethyl-cellulose (0.20 g). First ethyl cellulose was added with ethanol and heated at 80°C to get gel form, then gel was added to TiO_2 powder in a mortar, finally α-terpinol was added dropwise while grinding the paste [146]. For comparison purpose, 21 nm P25 commercial titania powder was received from Sigma Aldrich and the same paste composition was followed.

Photoanode preparation

Firstly, to make blocking TiO_2 layer, cleaned FTO substrates were dried and immersed into 40 mM aqueous $TiCl_4$ solution at 70 °C for 30 minutes then washed with distilled water and ethanol. After drying in the air, a layer of 20 nm transparent TiO_2 paste was coated on the FTO glass by a manual screen printer (Mascoprint Developments Ltd, 120T mesh/inch) and dried for 6 min at 125 °C. This screen printing procedure (coating, storing and drying) was repeated (4 layers) to get an appropriate thickness of 10-12 µm for the working electrode. Then one layer of TiO_2 paste containing 400 nm sized anatase particles was screen printed, resulting in a light-scattering TiO_2 film of 2.5–3 µm thickness on transparent titania layers [147]. In order to get crystallization and to remove the organic particles, prepared thin films were annealed rapidly at 150, 250, 350 and 450°C for 10, 10, 10 and 30 minutes respectively. The TiO_2 “double-layer” film thus produced is once again treated with 40 mM $TiCl_4$ solution, as mentioned previously, then rinsed with water and ethanol and sintered at 500 °C for 30 min. The electrodes were cooled to 80 °C and ready for dye sensitization process.

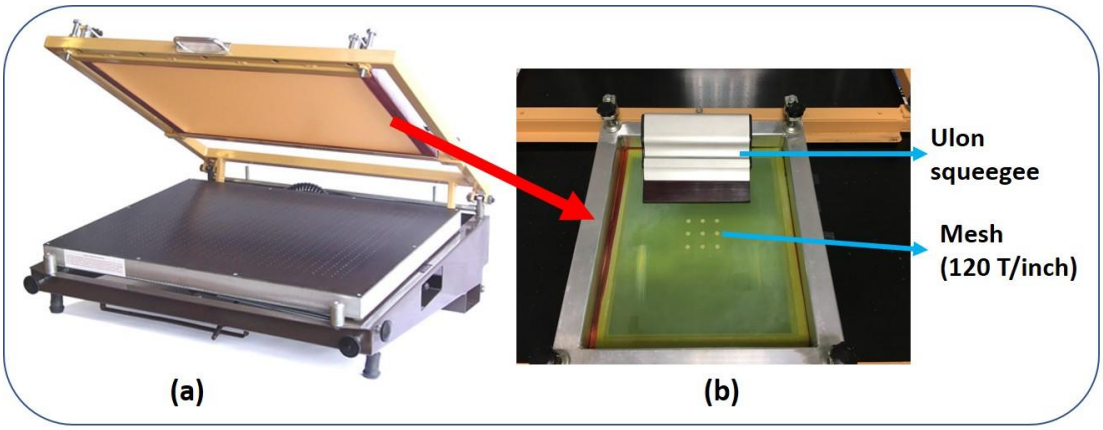

Figure 32. Mascoprint manual screen printer (b) screen used in this work

For transparent DSSC fabrication, $TiCl_4$ solution treatment was not used in order to minimize the photoanodes transparency loss. The screen printing procedure of 20 nm transparent titania paste was also repeated (2-7 layers) to get different thicknesses for the working electrode (Devices labelled as L2-L7). Finally, the transparent electrodes were annealed as mentioned above.

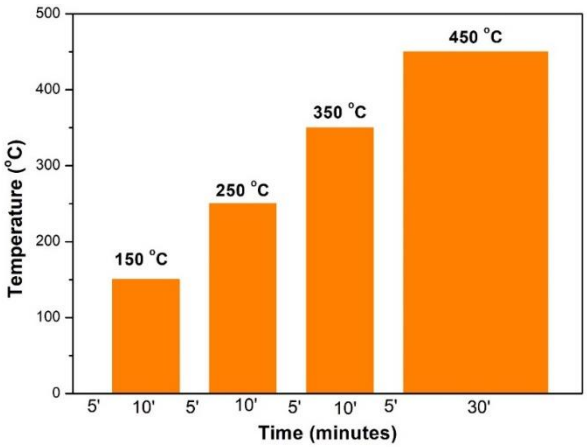

Figure 33. Temperature program used for sintering titania electrodes

2.1.2. Sensitiser

As discussed earlier, the sensitiser is a key component of the dye solar cell, which captures energy from the incoming light and injects electrons into the conduction band of the metal oxide [148]. Two types of sensitisers are used in this work.

Ruthenium (N719)

Dyes from the ruthenium family have been found to be ideally suited for the sensitization of TiO_2 in dye solar cells. Mostly ruthenium sensitiser (N719) was used in this work. The molecular structure of N719 is given in Figure 34. Ruthenizer 535 bis-TBA sensitiser was received in solid form from SOLARONIX [149]. The dye solution (0.2 mM) was prepared in absolute ethanol.

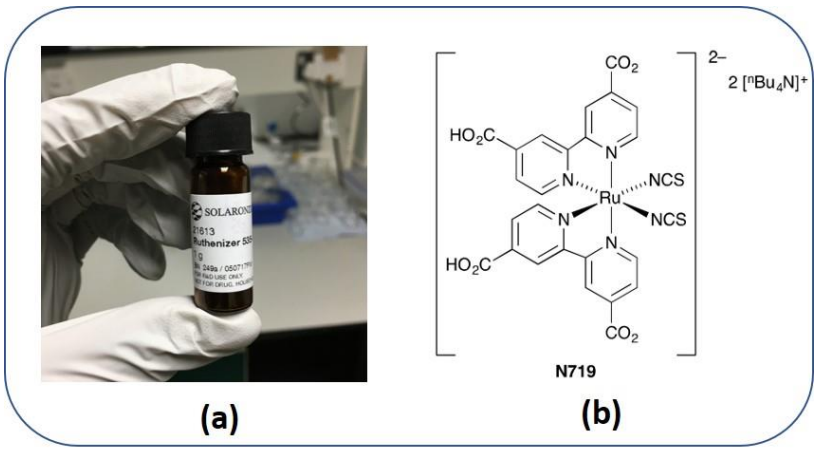

Figure 34. (a) Ruthenizer 535 bis-TBA from solaronix, and (b) Molecular structure

A new heteroleptic Ruthenium(II) polypyridyl complex having an extended π-conjugation (m-HRD-1)

The new sensitiser m-HRD-1 was designed and synthesised by Dr. Giribabu's group (CSIR-IICT, India) and used as received in one part (section 3.3) of this thesis. The synthesis molecular structure of the newly designed complex is presented here.

Synthesis of 5-(3,5-di-tert-butylphenyl)thiophene-2-carbaldehyde (1)

3,5-di-tert-butyl bromobenzene (942 mg, 3.5 mmol) was dissolved in 40 ml of dry toluene, to which $CsCO_3$ (393.6 mg, 1.2 mmol), $Pd(PPh_3)_4$ (0.25 equivalents) and 5-(4,4,5,5-tetramethyl-1,3,2-dioxaborolan-2-yl)thiophene-2-carbaldehyde (1.86 g, 7.8 mmol) were added. The reaction mixture was then refluxed under nitrogen atmosphere for 12h. After cooling to RT, the crude mixture was purified using silica gel column EtOAc/Hex (1:4 v/v) to provide the desired product (90% yield). Anal. Calcd. For: $C_{19}H_{24}OS$ % (300.460): C, 75.95; H, 8.05; N, 5.32. Found: C, 75.92; H, 8.03; N, 5.30. ESI-MS (m/z): $C_{19}H_{24}OS$ [300.460]: M 301 (100%). ^1H NMR ($CDCl_3$, δppm): 9.85 (s, 1H), 7.70 (m, 1H), 7.45 (m, 3H), 7.35 (m, 1H), 1.35 (s, 18H).

Synthesis of 4,4'-bis-2-(5(3,5-di-tert-butylphenyl)thiophene-2-yl)vinyl)2,2'-bipyridine (3)

This ligand was synthesized by using Wittig-Horner's reaction [150]. NaH (360 mg, 15 mmol) was added to a solution of 2,2'-bipyridine-4,4'-diphosphonate (1.5 g, 3.5 mmol) and 5-(3,5-di-tert-butylphenyl)thiophene-2-carbaldehyde (1) (0.51 g, 7.8 mmol) in 150 ml of dry tetrahydrofuran (THF). The resulting mixture was refluxed overnight under nitrogen atmosphere. The reaction mixture was allowed to cool to room temperature and filtered the compound. The filtrate was concentrated and the solid was washed with methanol and dried to obtain the desired product in pure form of 75% yield. Anal. Calcd. For: $C_{50}H_{56}N_2S_2$ % (749.132): C, 80.17; H, 7.54; N, 3.74. Found: C, 80.20; H, 7.52; N, 3.70. ESI-MS (m/z): $C_{50}H_{56}N_2S_2$ [740.132]: M 750 (100%). ^{1}H NMR ($CDCl_3$, δppm): 8.65 (d, 2H), 8.50 (s, 2H), 7.55 (d, 2H), 7.42 (s, 4H), 7.35 (s, 2H), 7.32 (d, 2H), 7.20 (d, 2H), 7.15 (d, 2H), 6.95 (d, 2H), 1.42 (s, 36H).

Synthesis of Ru(L)(p-cymene)$(Cl)_2$

A mixture of 3 (0.38 g, 1.25 mmol) and $[Ru(Cl)_2$-(p-cymene)$]_2$ in ethanol:chloroform (8:2 v/v) was refluxed for 4 hours under nitrogen atmosphere. Evaporation of the solvent under reduced pressure produced the pure complexes as an orange solid.

Synthesis of m-HRD-1

The above p-cymene complex (1.24 mmol) and 4,4'-dicarboxy-2,2'-bipyridine, (**L**) (0.303 g, 1.24 mmol) in anhydrous DMF (75 ml) were heated to 140 ^{o}C for 4 hours under nitrogen atmosphere and in the dark. NH_4SCN (1,5 g, 19.7 mmol) was then added to the mixture and heating was continued for 4 h. After cooling to room temperature, DMF was evaporated and water was added. The resulting purple solid was filtered and washed with water. The crude complex in basic

methanol [with tetrabutyl ammonium hydroxide (TBAOH)] was further purified on a Sephadex LH-20 column with methanol as eluent. The main band was collected, concentrated, and precipitated with dilute acidic methanol to obtain pure desired complex. Anal. Calcd. For: $C_{80}H_{99}N_7O_4RuS_4$ 1(TBA) % (1452.02): C, 66.17; H, 6.87; N, 6.75. Found: C, 66.20; H, 6.20; N, 6.72. ESI-MS (m/z): $C_{80}H_{99}N_7O_4RuS_4$ 1(TBA) [1452.02]: M+1 1453 (5%).

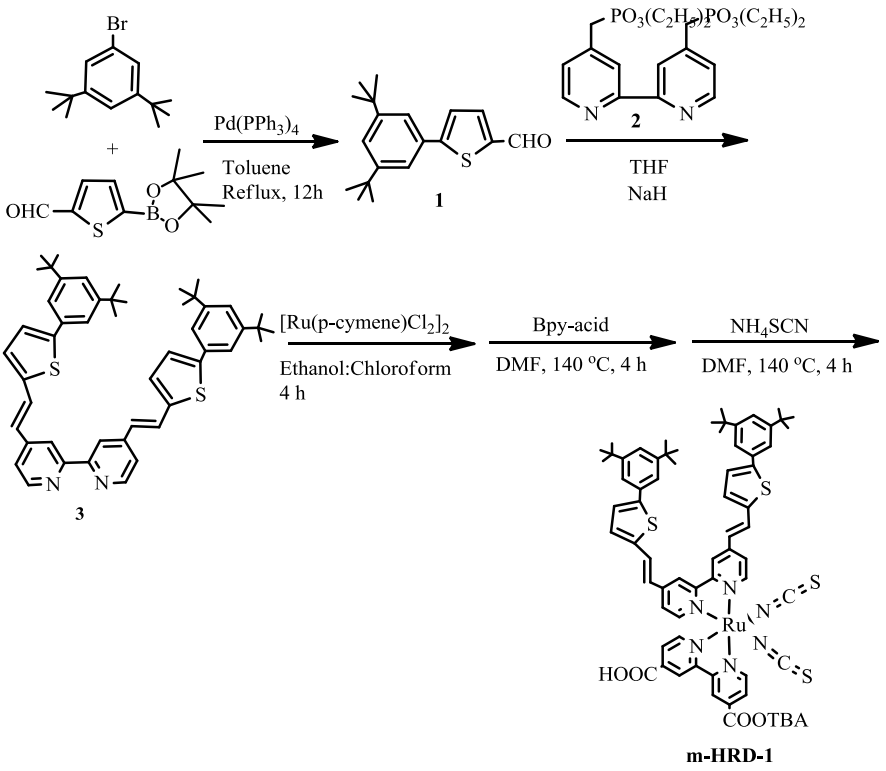

Figure 35. Synthetic scheme of m-HRD-1.

The details of the synthetic strategy adopted for the synthesis of m-HRD-1 are shown in Figure 35. The compound 5-(3,5-di-tert-butylphenyl)thiophene-2-carbaldehyde was synthesized by adopting Suzuki coupling between 3,5-di-tert-butyl bromobenzene and 5-(4,4,5,5-tetramethyl-1,3,2-dioxaborolan-2-yl)thiophene-2-carbaldehyde [151]. Bpy-phosphonate was synthesized as per the literature methods [152]. I have adopted Wittig-Horner's reaction for the introduction of C=C double bond was introduced at 4, 4’ positions of the bipyridine

ligand using Bpy-phosphonate [150]. The ligand Bpy-thio-butyl (L) was characterized by various spectroscopic techniques that includes elemental analysis, Mass, IR and ^{1}H NMR spectroscopies. The ligand L and [RuL(p-cymene)Cl_2]$_2$ complex by refluxing in ethanol : chloroform mixture to get the chloro derivative of m-HRD-1 complex. Finally, the m-HRD-1 complex was synthesized by refluxing chloro derivative with Bpy-acid and aq. ammonium thiocyanate in DMF and following by spehadex column purification. Preliminarily, m-HRD-1 was characterized by elemental analysis and ESI-MS spectroscopies. The presences of a molecular ion peak at 1453 (m/z) in ESI-MS spectrum confirms one TBA molecule in its molecular structure.

Dye sensitization process

Dye solution was prepared in organic solvents. For N719 dye, ethanol was used as a solvent and 0.1 mM dye solution was prepared. For m-HRD-1 acetonitrile solvent was used. Once the prepared photoanodes were cooled down to 80°C, they were immersed into the dye solution at room temperature for 16-24 hours in dark condition to assure complete sensitiser uptake [153].

If not used directly after preparation, the TiO_2 films were stored in a desiccator until the final assembly of the solar cell. Before the dye uptake TiO_2 layers were again heated to 450 °C for 15 min. The firing leads to a partially dehydroxylated, highly activated surface for dye adsorption.

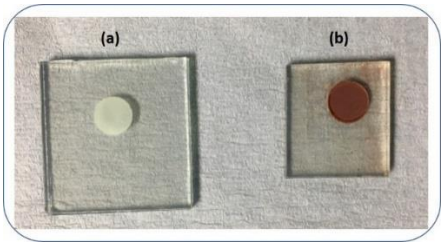

Figure 36. Photos of the prepared photoanodes (a) before, and (b) after dye-sensitisation process

2.1.3. Spacer

The back contact of a dye sensitised solar cell requires a spacer to separate photo anode from the counter electrode. The spacer also serves as a medium for the transfer of ions between two electrodes. In this work, 25 µm thick plastic film from Solaronix (Meltonix 1170-25PF) was used as a spacer [154]. The sealing temperature of this spacer is ~100 °C.

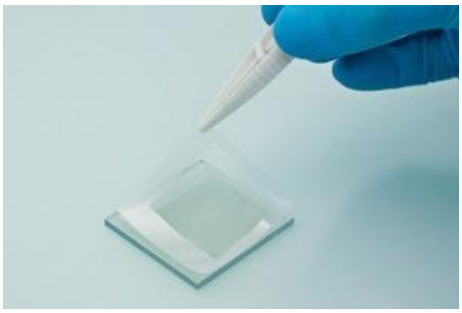

Figure 37. Meltonix 1170-25PF spacer from Solaronix

2.1.4. Electrolyte

For this work, the iodide/tri-iodide electrolyte comprising 0.4 M lithium iodode (LiI), 0.4 M tetrabutylammonium iodide (TBAI), and 0.04 M I_2 dissolved in 0.3 M N-methylbenzimidazole (NMB) in acetonitrile (ACN) and 3-methoxypropionitrile (MPN) solvent mixture at a volume ratio of 1:1 was prepared and stirred for 24 hours at room temperature and used [155].

2.1.5. Counter electrode

Platinum

Thermally sputtered platinum electrodes from Solaronix were used as counter electrodes in DSSCs. For a few experiments, platisol platinum paste from Solaronix was used to prepare the counter electrodes by screen printing or doctor blading or spin coating on the FTO glass [156]. After coating, the electrodes were dried in air and annealed at 600°C for 30 minutes then cooled down.

CZTS

Copper zinc tin sulphide (CZTS) counter electrode was used in one of the sections. Jet nebulizer assisted spray (JNS) coating technique was used to deposit the CZTS film on FTO glass. The electrode was coated by Dr. Ravi Dhas's group (Bishop Heber College- India). The experimental procedure of the newly coated counter electrode is presented here.

CZTS film deposition

Precursor solutions copper chloride, zinc chloride, tin (II) chloride, and thiourea were taken in the ratio of 2:1:1:8 and dissolved in 35 mL of distilled water then stirred constantly under room temperature for 30 min. The filtered precursor solution was taken in the pocket size nebulizer and spraying was carried out on FTO substrates for 5 min. The temperature of the spray coated substrates was 250°C, 300°C, 350°C, and 400°C which are labelled as CZTS1, CZTS 2, CZTS 3 and CZTS 4 respectively [157].

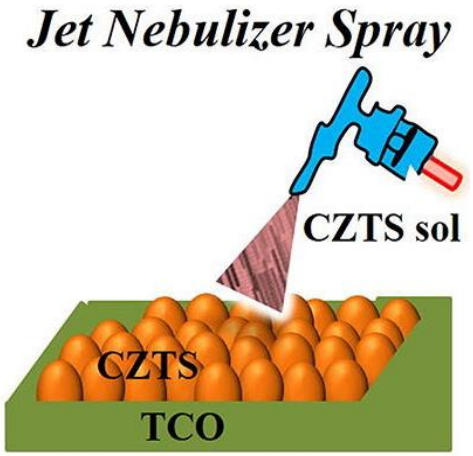

Figure 38. JNS spray coating technique used for depositing CZTS films

2.2. Characterization of synthesised materials

2.2.1. Structural properties

The structural properties of dried TiO_2 powder were characterized using X-ray diffraction (XRD) analysis on an X'pert pro MPD X-ray diffractometer by PAN analytical with Cu Kα radiation (λ = 1.5406 Å).

2.2.2. Morphological studies

FESEM images and elemental energy dispersive X-ray analysis (EDAX) of the coated films were checked on a field emission scanning electron microscope (Supra 35VP, Carl Zeiss). A JEM-2100 LaB6 200 kV TEM instrument was used to obtain the high-resolution transmission electron microscopy (HRTEM) images of the samples to investigate the morphology and the selected area electron diffraction (SAED) of meso-TiO_2 to confirm the nature of crystallinity. For these experiments, the mesoporous-TiO_2 was subjected to ultrasonication in acetone medium to disperse the fine powder onto the copper grids. The particle size calculation from the microscopic images (SEM/TEM) was carried out by using the "ImageJ" software. This is an open source Java image processing program inspired by NIH Image .

2.2.3. Optical properties

The ethanol dispersion of the synthesized TiO_2 was prepared to measure the absorption spectrum using a UV-Vis-NIR Spectrophotometer (Shimadzu Corporation, Kyoto, Japan) in CSIR-Central Glass and Ceramic Research Institute, Kolkata, India. Zeta potential measurement of synthesized TiO_2 in water was performed using Horiba (SZ-100) analyser.

Dye Loading

The number of dye molecules adsorbed on the semiconductor surface was measured by the dye desorption method. To desorb the dye molecules, dye loaded TiO_2 electrode was immersed in a known volume of tetrabutylammonium hydroxide (TBAOH) in a respective solvent at a known concentration. The UV-vis spectrum of the resulting dye solution was measured. The Beer-Lambert law (A = abc) relates the absorbance A of the solution with its concentration c.

Where, a is a wavelength-dependent absorptivity coefficient (sometimes called ε, also known as molar absorptivity), b is the optical-path length, and c is the absorbing species concentration. The number of adsorbed dye molecules can be calculated from this. Knowing the thickness of the TiO_2 layer, surface area, pore size, porosity, and the concentration of dye molecules on the surface of the mesoporous TiO_2 was also estimated.

2.2.4. Thermal properties

Thermogravimetric analysis (TGA) was carried out on a Mettler Toledo TGA/SDTA 851e instrument at a heating rate of 10 $^oC\ min^{-1}$ with 10 mg of sample under N_2 atmosphere.

2.2.5. Surface area measurements

Nitrogen physisorption measurements of all the samples were carried out by using a Quantachrome (iQ3) instrument after evacuation at 150°C for 4h. The specific surface area was calculated by the BET method, whereas desorption cumulative pore volume and pore size distribution were calculated by the BJH method.

2.2.6. Thickness of the electrodes

Thickness of the semi-transparent TiO_2 electrodes was measured using Dektak 8 Advanced Development Profiler. During the optimisation stage, Ambios XP100 stylus surface profiler was used to align the screen printed TiO_2 layers and get the optimum thickness for the photoanode.

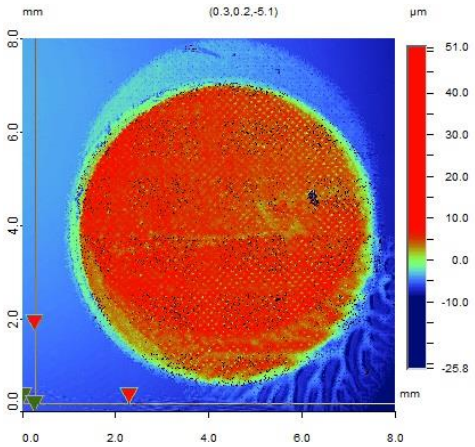

Figure 39. Alignment of the screen printed TiO_2 electrodes from Ambios XP100 stylus surface profiler

2.2.7. Cyclic voltammetry

To understand the catalytic activity of the counter electrodes, the cyclic voltammetry was performed. An electrolyte having 10 mM lithium iodide (LiI), 1 mM iodine (I_2) and 0.1 M lithium perchlorate ($LiClO_4$) in acetonitrile (ACN) was prepared and stirred for 30 minutes at room temperature [158]. Prepared sample

as a working electrode, Ag/AgCl as reference electrode and a Pt wire as a counter electrode were kept in a container with prepared electrolyte as a medium as described in Figure 40. Metrohm autolab was used to perform the CV analysis.

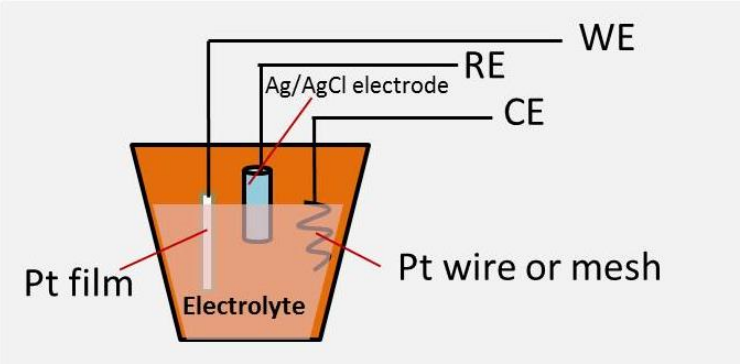

Figure 40. Schematic illustration of the electrochemical setup used in CV analysis

2.3. Device fabrication

To fabricate a DSSC device, the dye loaded photoanode was rinsed with ethanol. Two kinds of DSSC were made: open cells and closed cells.

For open cells,

Pt counter electrode was placed over the dye-sensitised photoanode and a plastic spacer was kept in between those two electrodes. Prepared redox electrolyte was introduced into the device. Two binder clips were used to keep the glass slides in place. The active area of working electrode was 0.28cm^2 [159].

For closed cells,

Pt electrode was placed over the dye-adsorbed TiO_2 electrode with a 25 µm hot-melt spacer between two electrodes and heat pressed at 100 °C. The internal space was evacuated by using a vacuum pump. Finally, the prepared iodide/tri-iodide electrolyte was introduced into the cell through the small hole drilled in the

counter electrode. Active area of the device was 0.28cm^2. The hole in the counter electrode was sealed by a round Surlyn sheet and a piece of cover glass.

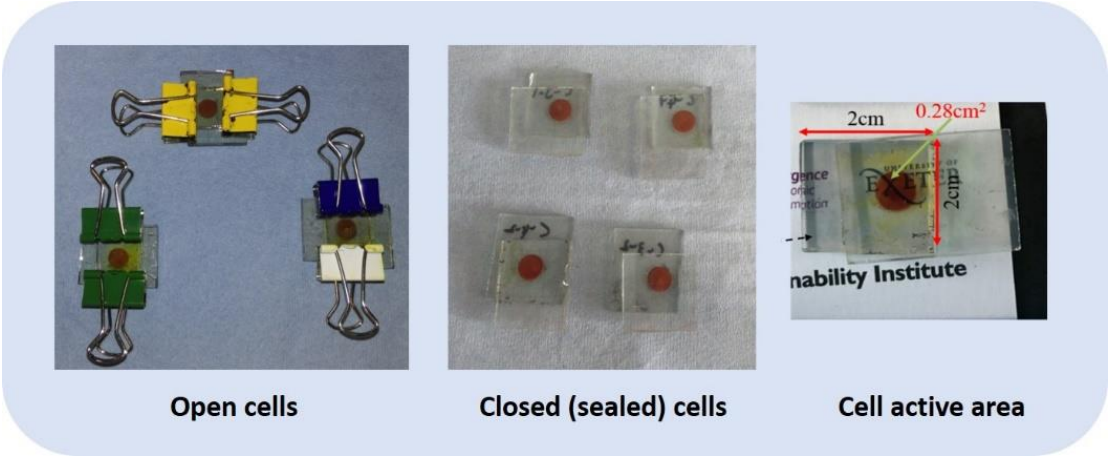

Figure 41. Fabricated open and closed devices

2.4. Device characterization

The basic photovoltaic characterisation of DSSC are carried out under steady-state conditions where the charge density does not change with time.

2.4.1. Photovoltaic parameters

Current-voltage measurement is a simple method to evaluate photovoltaic parameters of the solar cells under both light and dark conditions. Figure 42 shows a typical I-V curve for a solar cell under illumination. The following parameters can be extracted from the I-V curve [160].

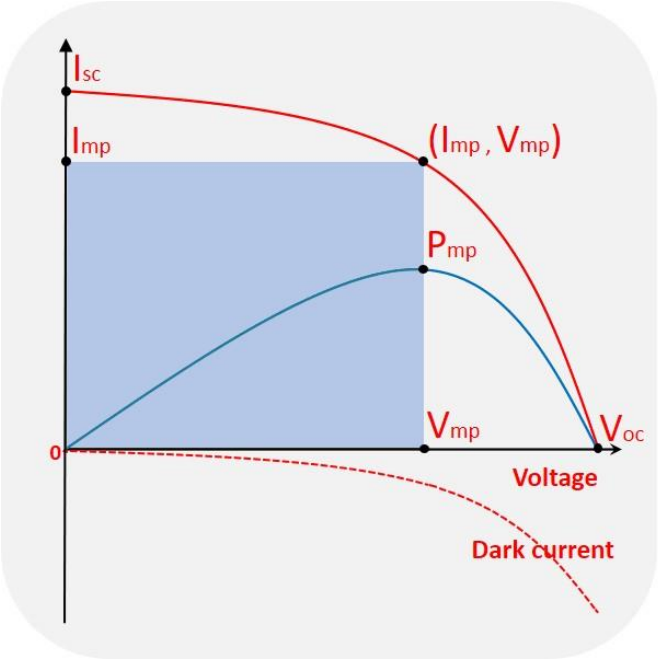

Figure 42. Current-voltage characteristics of a solar cell, in dark (red dotted curve) and under illumination (red solid curve). The power curve (product of current and voltage, blue curve) is also presented as a function of the applied voltage bias. The maximum achievable power from the solar cell is given as the rectangular shaded area (in blue)

Short circuit current (I_{sc}): Solar cell current measured at an applied potential of zero volt, I_{sc} increases linearly with light intensity.

Open circuit voltage (V_{oc}): Solar cell potential measured when there is no external load. Under these conditions there is no external electric current between the terminals.

Fill Factor (FF): The fill factor is defined as the ratio

$$FF = \frac{Imp \times Vmp}{Isc \times Voc}$$

The F.F. describes how a maximum power rectangle fits under the I-V characteristics. It is influenced by the series resistance (R_s) following from the internal resistance and shunt resistance (R_{sh}) from the leakage of current [161].

A simplified equivalent circuit for a DSC including R_s and R_{sh} is shown in Figure 43. To obtain high F.F. R_s should be small, while R_{sh} needs to be as large as possible (Figure 44).

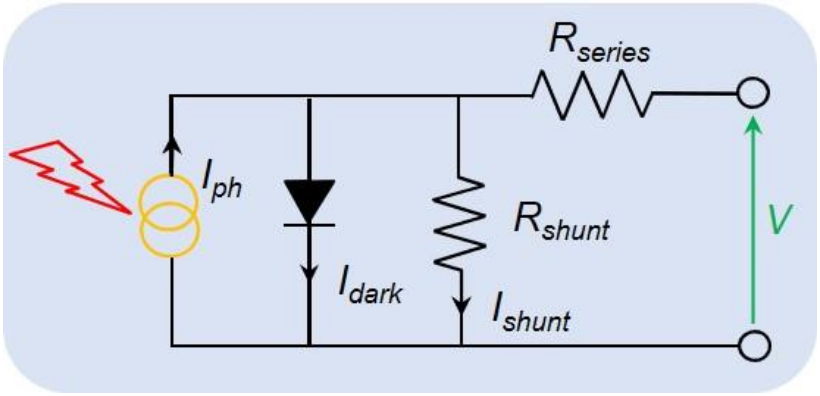

Figure 43. A simplified equivalent circuit of a solar cell with series and shunt resistances

Power conversion efficiency (η): The PCE is defined as the ratio of the maximum power output from a cell (P_{max}) to the incident radiation power (P_{in}) [162].

$$\text{Power conversion efficiency} = \frac{\text{Voc Isc FF}}{\text{Pin}}$$

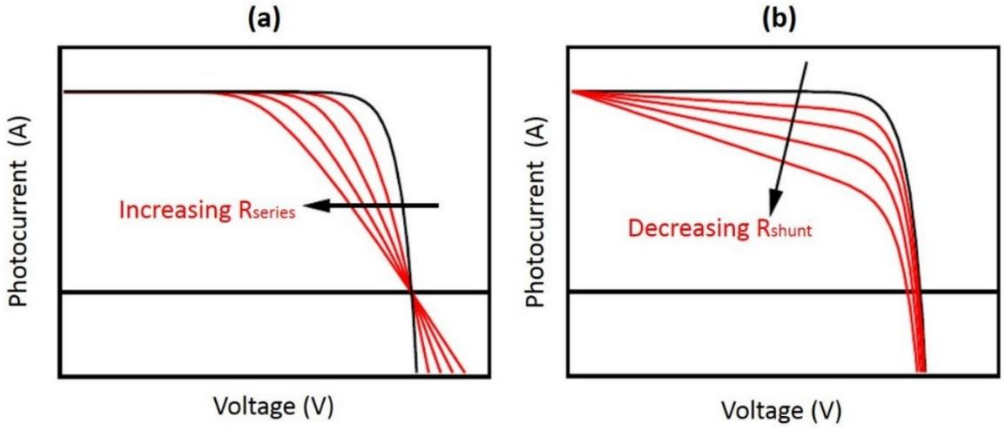

Figure 44. Influence of (a) increasing the series resistance R_{series} and (b) decreasing the parallel shunt resistance R_{shunt} on the shape of the J–V curve [25]

This parameter is equated to the performance of the DSSC device. In order to compare different results, standard test condition should be used for measurements of all the devices. The standard condition specifies AM 1.5 spectrum illumination with an incident power density 1000 W/m^2 at 298K. The Air Mass (AM) is the ratio of the path length of the sun light through the atmosphere when the sun is at a given angle θ the zenith, to the path length when the sun is at its zenith. This relation can be approximated by

$$AM = \frac{1}{\cos\theta}$$

The standard condition is AM 1.5, which corresponds to a solar incident angle of 48.2° relative to the surface normal.

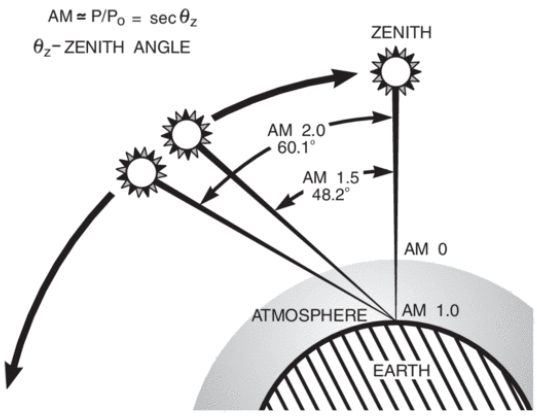

Figure 45. Illustration of the “air mass” concept [163]

Experimental Set up

Solar Simulator

In an indoor controlled environment, the photovoltaic performances of the assembled devices were measured under 1000 W/m^2 of light from a Wacom AAA continuous solar simulator (model: WXS-210S-20, AM1.5G). The simulator is

equipped with a 5000W DC Xenon Lamp, which yielded a high non- uniformity and a temporal instability lower than 2% on an irradiated surface of 300mm×300mm. The lamps used in the simulators needed time after being switched on to reach a steady energy flux. For this reason, after switching the simulators on, a one-hour delay was used before starting the calibration. A calibrated silicon photo-diode was used to tune the solar simulator before each test: the current flowing into the photodiode was the trusted parameter to calibrate the instrument.

I-V tracer

The I–V characteristic of the devices was recorded using an EKO MP-160i I–V Tracer. This instrument operated in the range between 0.5V and 1V and 0.1 mA and 30 mA according to the current output of the devices. A four-wire configuration was used to extract the electrical outputs from the cell. It was coupled to a software tool able to calculate several parameters, such as the open-circuit voltage, the short circuit current, the maximum power and the fill factor. Moreover, the system gave in output the I-V curve of the cell.

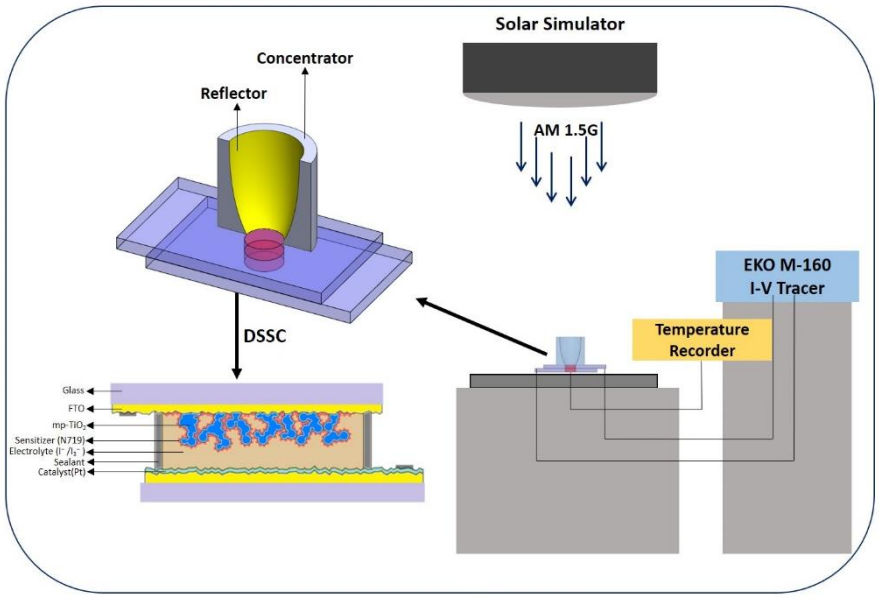

Figure 46. Schematic representation of the experimental set up

Temperature recorder

The temperature of the devices was recorded using an OMEGA RDXL 12SD temperature recorder. Type K thermocouples were used in this work. The thermocouples were calibrated according to the temperature of melting ice at atmospheric pressure (0°C).

For the low concentrator work, the concentrator unit was placed on the DSSC and the same procedure was followed.

2.4.2. Spectral performance of the devices

The optical properties of the fabricated DSSCs was measured using a UV-VIS-NIR spectrometer (PerkinElmer, Lambda 1050). This instrument could scan a material's transmittance, reflectance and absorbance in the range between 175nm and 3300nm, with a resolution that can be set down to 0.5nm. A deuterium and tungsten halogen lamp were used as light source: the light passed through a monochromator and some filters before reaching the sample. The sample was placed in a sample holder: transmittance and absorbance were measured with reference to air, whereas the reflectivity with reference to a calibrated reflective white surface (Labsphere SRS-99-020 AS-01161-060, certificate reflectance between 250-2500nm: 99%). The Perkin Elmer Lambda 1050 used a PMT, InGaAs and PbS 3-detector module [164].

For the spectral measurements of the aged DSSCs, the devices were kept inside a box and the measurements were carried out again.

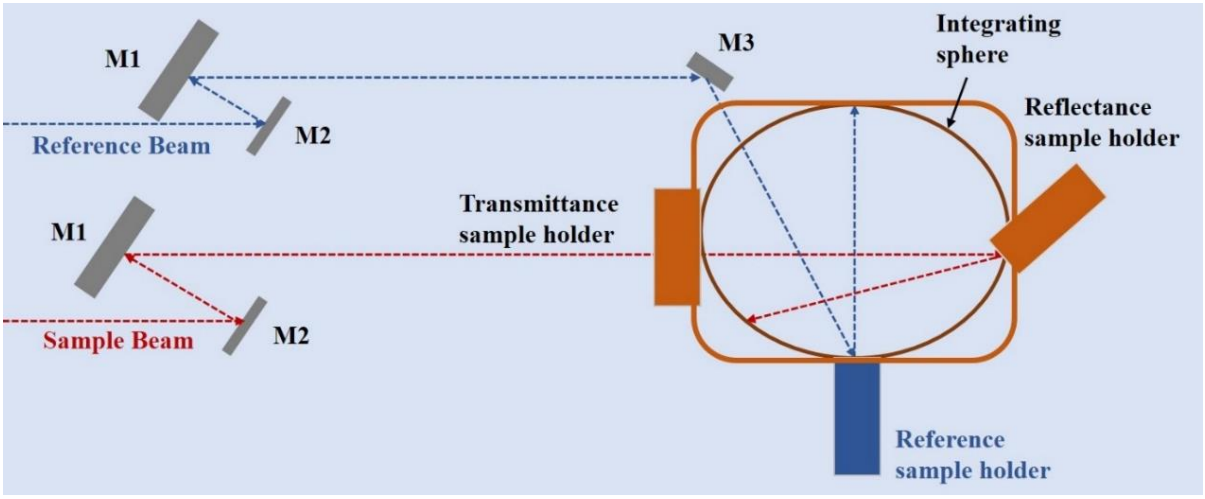

Figure 47. Schematic representation of the UV/vis/NIR spectrophotometer used for optical measurements

2.4.3. Electrochemical impedance spectroscopy

Even though I-V characterisation is an important tool to determine the overall solar cell performance, it gives little insight to the interfacial processes taking place within a device. Electrochemical impedance spectroscopy (EIS) has been established in recent years as a standard technique for the analysis of the individual processes within the interfaces of DSSCs. Since the dye solar cell behaves as an electrical circuit, this EIS technique is to measure the current response to the application of an AC voltage as a function of the frequency. An important advantage of impedance spectroscopy over other characterisation techniques is the possibility of applying an AC voltage with small amplitudes to perturb the systems.

To measure EIS parameters, DSSC is perturbed by an external potential bias with a harmonically modulated small-amplitude voltage $\Delta U = U_A e^{i\omega t}$. A small voltage perturbation causes a current flow $\Delta I = I_A e^{i(\omega t - \theta)}$ with a phase delay by angle θ. The impedance of the device is given by,

$$Z = \left|\frac{\Delta U}{\Delta I}\right| = \left|\frac{U_A}{I_A}\right| e^{i\theta}$$

A more elaborative equivalent circuit that considers the different interfaces of the DSSC is shown in Figure 48.

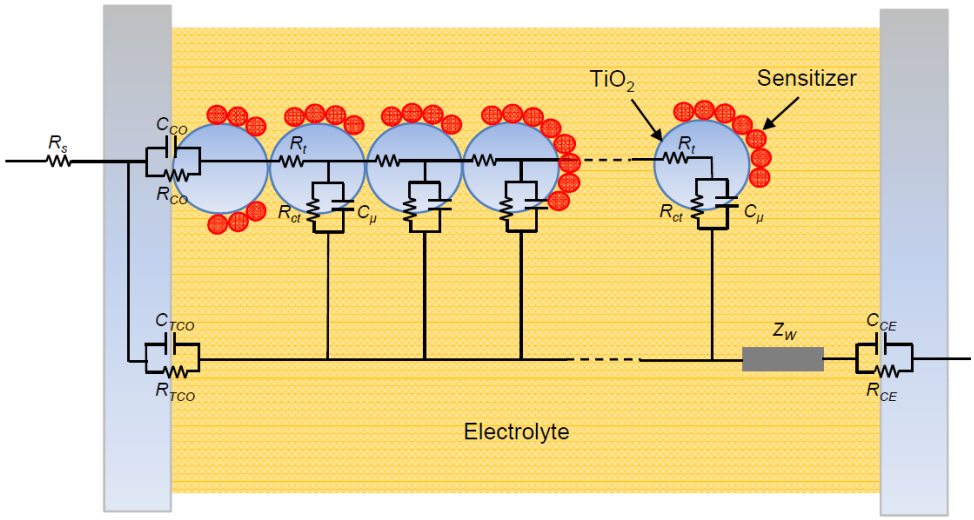

Figure 48. A general equivalent circuit of the liquid DSSC for impedance fitting

The large surface area interface between the TiO_2/ sensitiser/ electrolyte is considered as the heart of the DSSC device.

- R_t is the electron transport resistance in the TiO_2 surface. R_{ct} is the charge transfer (recombination) resistance at the TiO_2/redox couple interface. Cu is the total chemical capacitance of the TiO_2 nanoparticles.
- R_s is the series resistance including the sheet resistance of the TCO substrate, electrolyte resistivity and electrical contacts of the device.
- R_{TCO} is the charge transfer resistance, for the reduction of tri-iodide at the uncovered part of the FTO and C_{TCO} is the corresponding chemical capacitance.

- FTO-TiO_2 interface resistance and capacitance are given as R_{CO} and C_{CO} respectively.
- R_{CE} and C_{CE} are the charge-transfer resistance and capacitance at the counter electrode/redox electrolyte interface
- Warburg (Nernst diffusion) impedance of the redox liquid electrolyte is given as Zw [165].

When a small forward bias is applied, electrons are injected from the dye into the TiO_2 particles and then transferred through TiO_2 to the FTO. This process is measured as R_t. Some of the electrons recombine with the oxidized species in iodide electrolyte, that is measured as R_{ct} and the corresponding capacitance as C_μ. When the electrons reach the FTO, some of them recombine with the oxidized species in electrolyte, they are characterized as R_{TCO} and C_{CO}. The iodide ion diffusion process is measured as Warburg impedance (Zw). R_{CE} and C_{CE} are the measurement of the reduction of the iodide electrolyte [16]. Relate these components of the equivalent circuit to get the physical or chemical characteristics of the electrochemical system.

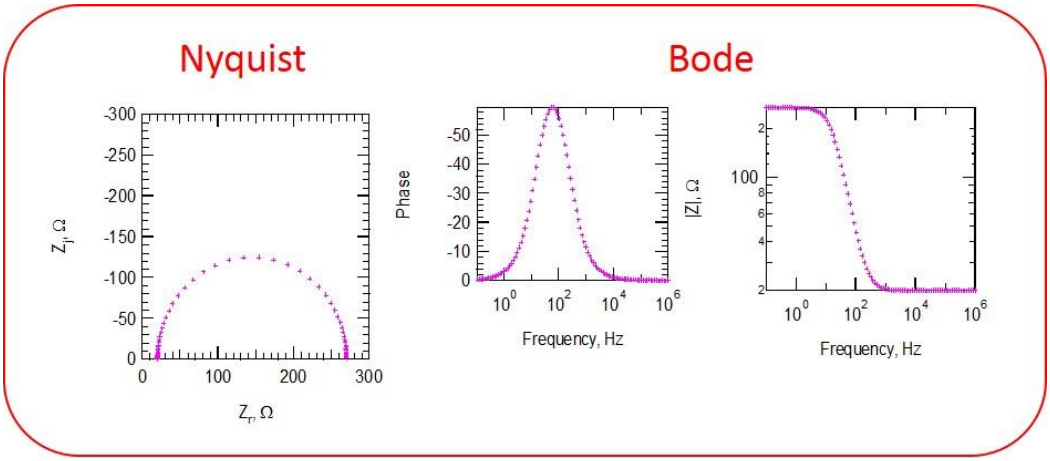

Figure 49. Nyquist and Bode plots obtained from EIS measurement

The experimental data in the form of Nyquist and Bode plots are fitted to obtain the impedance parameters of DSSCs.

Measurement setup

EIS measurements were carried out with an autolab frequency analyzer setup equipped with an Autolab PGSTAT 10 and a Frequency Response Analyzer (FRA) Module. The TiO_2 electrode of the DSSC was connected to the working electrode, and the Pt electrode was connected to the reference and counter electrodes of the instrument. The measurements were performed under dark and light condition with the frequency range from 0.1Hz to 100kHZ. For the measurements under light, the EIS experiment setup was moved to the solar simulator room and the devices were kept under the light. All the devices were measured at the respective open circuit voltage of the devices and the magnitude of the alternative signal used was 10mV. The experimental data were fitted with the Z-view software (version 3.4d, Scribner Associates, Inc., USA) using appropriate equivalent circuits. Figure 50 shows the experimental setup used for Impedance characterization.

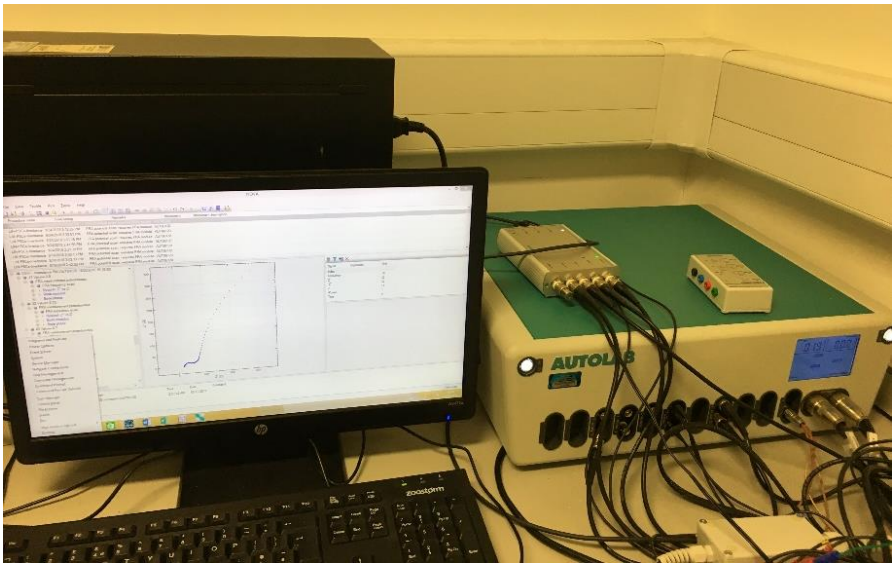

Figure 50. NOVA- Autolab- Electrochemical Impedance Spectroscopy station

2.5. Summary

All the different materials, methods and equipment used to carry out the research works in this thesis had been presented in this chapter. All the device fabrication and characterisation were done in the solar laboratory at the University of Exeter. Parts of material characterisation were done at our collaborators laboratories. A simple summary of fabrication and characterization of the DSSCs in this thesis is presented here.

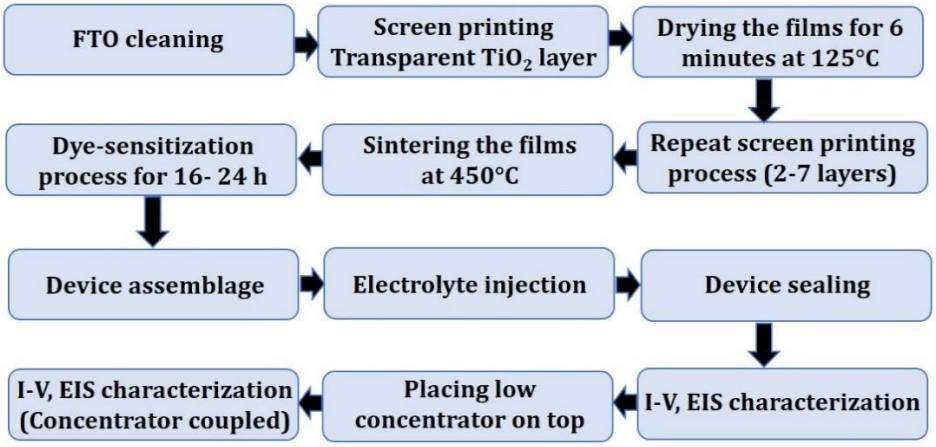

Figure 51. Summary of DSSC fabrication and characterisation

The data achieved from the experiments was analysed and the results are discussed in the upcoming chapters.

Chapter 3: Alternative materials for cost effective dye-sensitised solar cells

Dye-sensitised solar cell (DSSC) is a good example of where the quality of the materials and their interfacial properties are important to device performance. To be more competitive in the solar cell markets, improving the device efficiency, finding the suitable abundant materials, enhancing the device durability and further reducing the cost of production are needing to be considered. In this chapter, systematic optimization of key parameters and processing steps to produce low cost and high efficiency DSSCs is studied.

This chapter is based on the following published articles

1. **P. Selvaraj**, A. Roy, H. Ullah, P.S. Devi, A. Tahir, T.K. Mallick, S. Sundaram, *Int J Energy Res*, **2019**, 43, 523–534.
2. T. Jella, **P. Selvaraj**, H.M. Upadhyaya, T.K. Mallick, S. Senthilarasu, L. Giribabu, *O.A. Journal*, **2017**, *1*, 1.
3. D.D. Kirubakaran, S. Pitchaimuthu, C.R. Dhas, **P. Selvaraj**, S.Z. Karazhanov, S. Sundaram, *Mater. Lett.* **2018**, *220*, 122.

3.1. Introduction

The working principle of DSSCs differs substantially from that of the first generation and second generation solar cells and is closely related to natural photosynthesis where light absorption and charge carrier transportation are carried out by different substances. Concretely, the constituent components and fundamental processes of DSSCs are schematically illustrated in Figure 52.

The fundamental processes include:

(1) photoexcitation of the dye to produce excited state sensitiser

(2) electron injection into the conduction band of TiO_2 resulting in the production of oxidized dye

(3) electron transportation to the FTO and flow to the Pt electrode via an external circuit

(4) regeneration of the oxidized dye by accepting electrons from the reduced redox couple

(5) regeneration of the oxidized electrolyte at the pt electrode by accepting electrons

(6) electron recombination by donating electrons to oxidized dye

(7) electron recombination by donating electrons to the oxidized redox couple

(8) relaxation of the excited dye to its ground state by a nonradiative decay process [166]

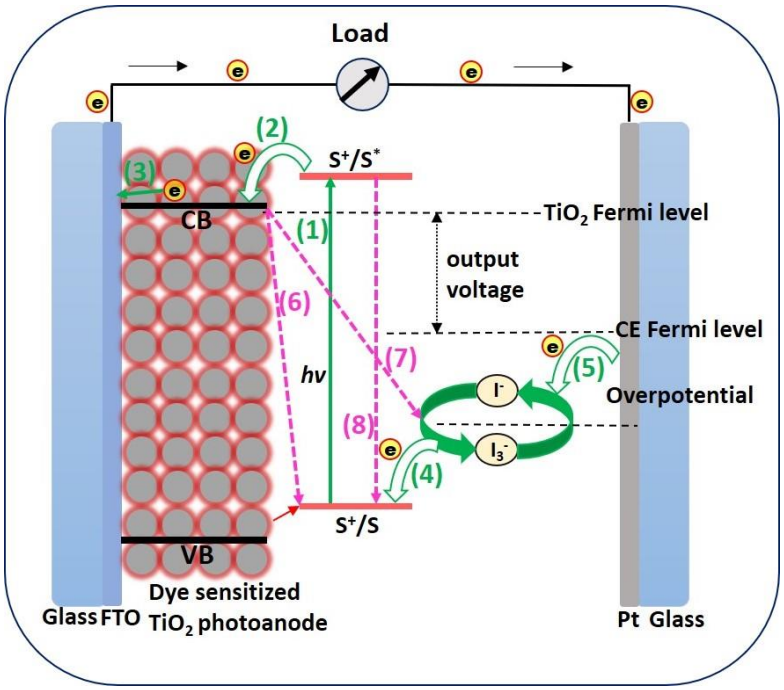

Figure 52. Schematic diagram of integral components and the fundamental processes of a DSSC

To achieve higher photovoltaic performance in dye-sensitised solar cells, the physical, chemical, optical and electrical properties of the four main components (Figure 52) of the device: (1) the metal oxide semiconductor, (2) the sensitised dye, (3) the redox couple electrolyte and (4) the counter electrode need to be modulated. For a high-effective DSSC, all components require more fine-tailoring.

3.2. High surface area mesoporous TiO_2 for DSSC

3.2.1. Introduction

As discussed in section 1.8, there are number of factors determining the photovoltaic performance of DSSCs but, the shape and structure of the photoanode material play an important role in photoelectric conversion efficiency [167]. A large number of research works have been conducted to study the influence of working electrode materials on device performance [168,169]. However, the power output of the DSSCs to become a competitive energy source has not yet been achieved [170].

Titanium dioxide (TiO_2) is the most commonly used of these semiconducting photoanode materials in DSSC [171]. TiO_2 nanoparticles with mesoporous nature offer a large internal surface area, which improves dye adsorption, leading to efficient light absorption and high photocurrent generation. Hence, high power conversion efficiency can be achieved compared to bulk TiO_2 material [172]. Moreover, this mesoporous structure offers rapid electron transport at the device interface, which improves the charge transfer properties of the DSSC [173,174]. There has been a considerable amount of research interest in synthesising mesoporous titanium dioxide with high surface area. Many simple methods such as sol-gel [175], hydrothermal, solvothermal and soft

template [176,177] have been used to synthesis mesoporous TiO_2 nanoparticles [178]. Due to the diversity of the employed template precursors, soft- template directed materials possess structural and morphological abundance [145,179]. Surfactants/templates are usually used to control the size of nanoparticles. The main disadvantage of nanocrystalline electrode materials is their low packing density. Systematic control synthesis of titania yields high surface area with high packing density nanopowder which can improve the dye-sensitised solar cell performance.

In this section, I discuss a simple and cost- effective method using soft template to obtain highly crystalline mesoporous TiO_2 nanoparticles. Cetyl trimethylammoniumbromide (CTAB), Sodium dodecyl sulfate (SDS), and dodecyl trimethylammonium bromide (DTAB) have been used as cationic surfactants. Structural, surface, and optical parameters of the synthesised TiO_2 powders have been characterized. The influence of various surfactants as soft-templates on the performance of utilizing them in DSSCs have been studied under 1 sun illumination. Moreover, electrochemical impedance spectroscopy of the fabricated devices has been investigated. All the results are compared with the commercial TiO_2 source (P25).

3.2.2. Experimental Section

Synthesis and characterisation of nanoparticles with device fabrication and photovoltaic characterisation methods are given in chapter 2.

3.2.2. Structural Properties

Figure 53 shows the XRD pattern of the TiO_2 samples synthesised using various surfactants (CTAB, SDS, and DTAB). It is clear that, the XRD patterns of these TiO_2 powders show well-resolved diffraction peaks at (101), (112), (200), (211),

(220) and (301) planes corresponding to the reflections of anatase TiO_2 material (JCPDS Card No 89-492). For the commercial P25 powder, the peaks at 25.28, 37.80, 48.04, 53.89, 62.68, 68.76, 70.30 and 75.02^o are matched with the anatase (A) (JCPDS Card No 21-1272) TiO_2 planes, also it contains a few rutile (R) peaks as well. In both cases no characteristic peaks of other phases can be detected and the diffraction peaks clearly suggest that all the products are of well crystalline [180]. This further recommends the decrease in particle size of the samples to a significant extent upon various surfactant treatments.

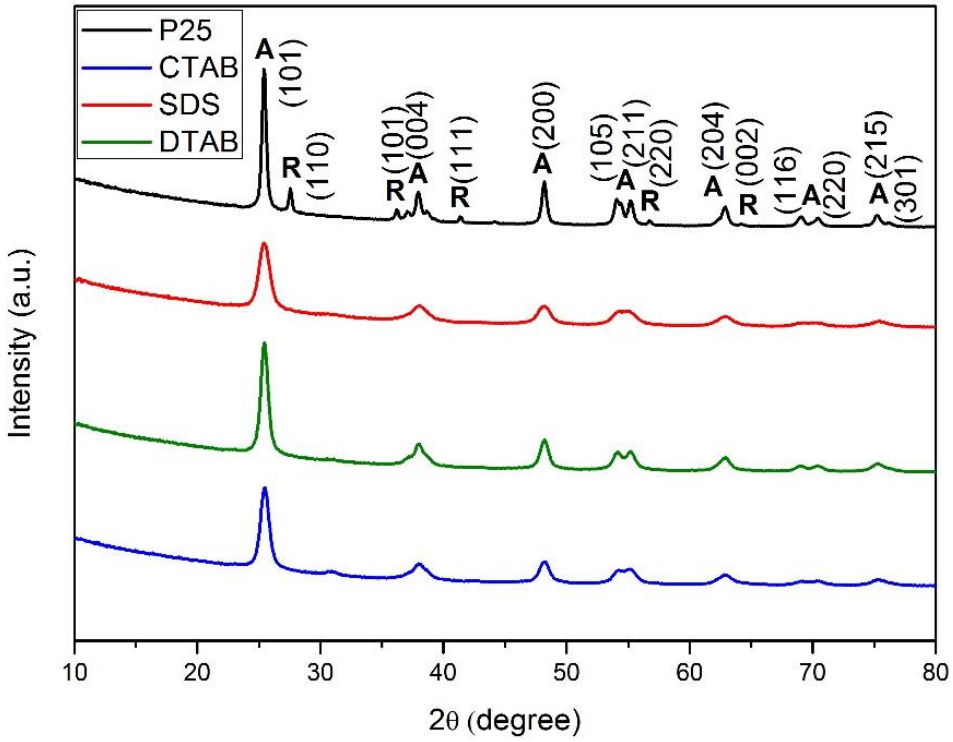

Figure 53. Powder XRD patterns of the meso-TiO_2 nanoparticles using various surfactants

3.2.3. Morphological analysis

To understand the morphology of the synthesized nanopowder, the samples were analysed using a scanning electron microscope. Figure 54 shows the FESEM images of TiO_2 nanoparticles calcined at 450°C and commercial P25

powder. All the samples are made of large irregular shaped particles formed due to aggregation of several spherical nanograins [181]. For the commercial P25, large aggregates of fine particles with an average particle size of about 23.22 nm (Figure 54 (d)) were found. Moreover, the samples prepared with the presence of different surfactants shows a similar aggregated structure to P25-TiO_2. However, mesoporous TiO_2 samples show smaller particle size distribution in the range between 8- 20nm (Figure 54 (a-c)), which indicates surfactant plays a crucial role to control the particle size reduction along with its distribution.

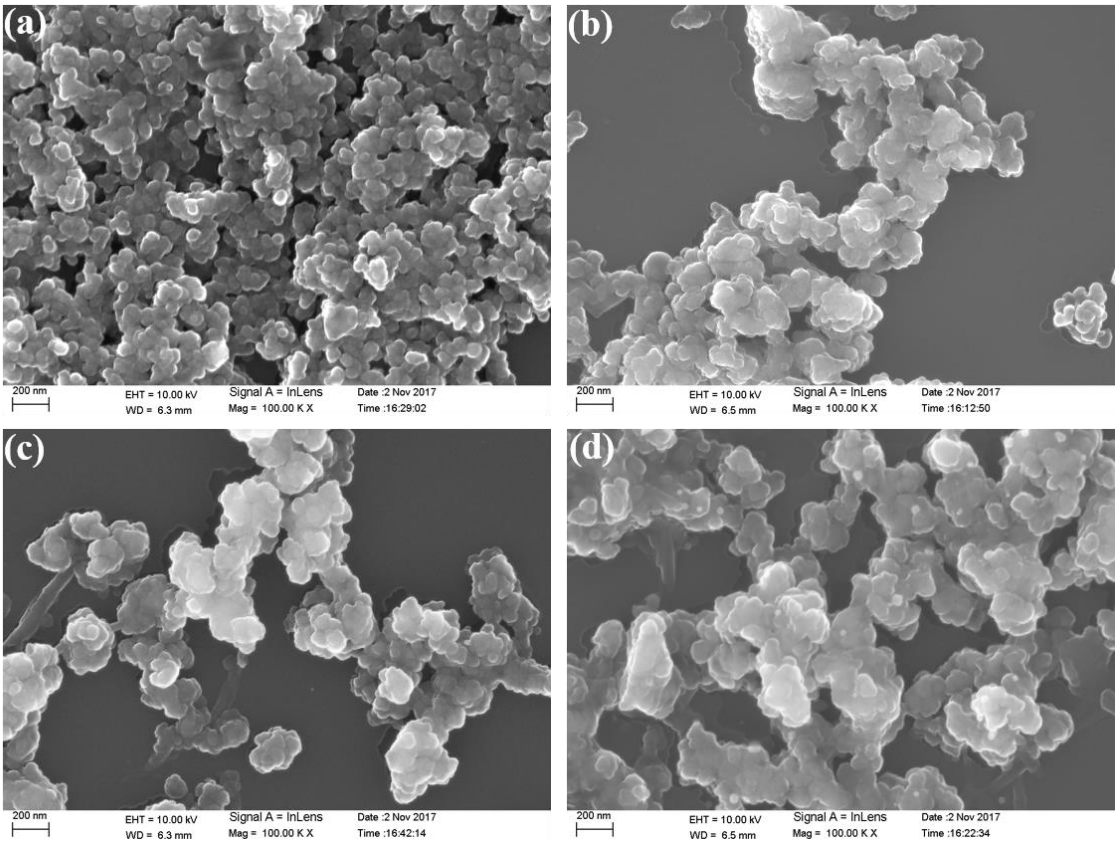

Figure 54. FESEM images of meso-TiO_2 nanoparticles (a) SDS, (b) DTAB, (C) CTAB (d) P25

Furthermore, the morphology and crystal orientation pattern of synthesized TiO_2 samples were investigated by transmission electron microscopy (TEM) and high-resolution transmission electron microscopy

(HRTEM). TEM images reveal that all the samples are highly crystalline in nature. Interestingly, the shape remains unaffected but a significant decrease in the particle size is observed in the order of P25>CTAB>DTAB>SDS. A comparative particle size plot has given as Figure 55, which indicates the particle size of P-25 is 23.2 nm, On the other hand, for SDS, DTAB and CTAB samples, particle size is 10, 12.5 and 14.6 nm respectively. Thinfilms consisting of larger particles have a smaller surface area, where less surface is available for dye adsorption, possibly reduce the amount of light absorbed and the number of electrons generated. On the other hand, films with smaller particles have a larger surface area and greater number of contact points between sintered colloidal particles or at the interface between the particles and the underlying substrate, which allow them to adsorb more dye molecules for electron generation.

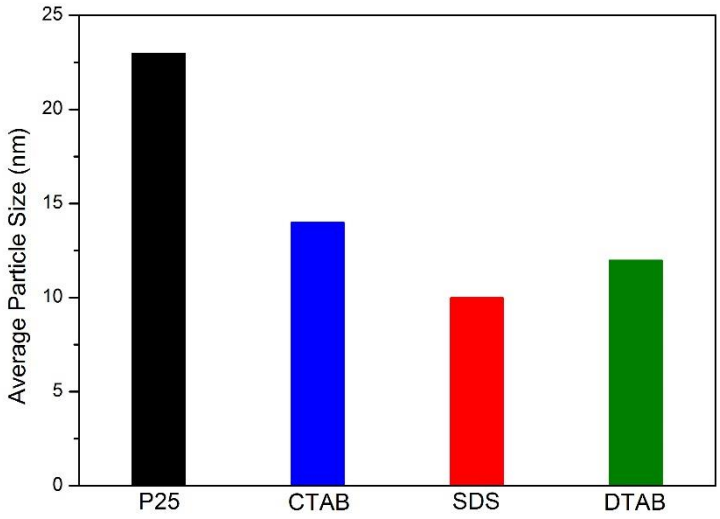

Figure 55. Particle size comparison of the synthesised nanoparticles

The HRTEM images resemble two sets of lattice fringes perpendicular to each other with distances to the d spacing of ~3.52 Å which strictly signifies the (101) crystal plane of the anatse TiO_2 for all the samples [182]. Besides, the SAED results confirm that these nanoparticles have highly polycrystalline planes corresponding to pure anatase phase of TiO_2.

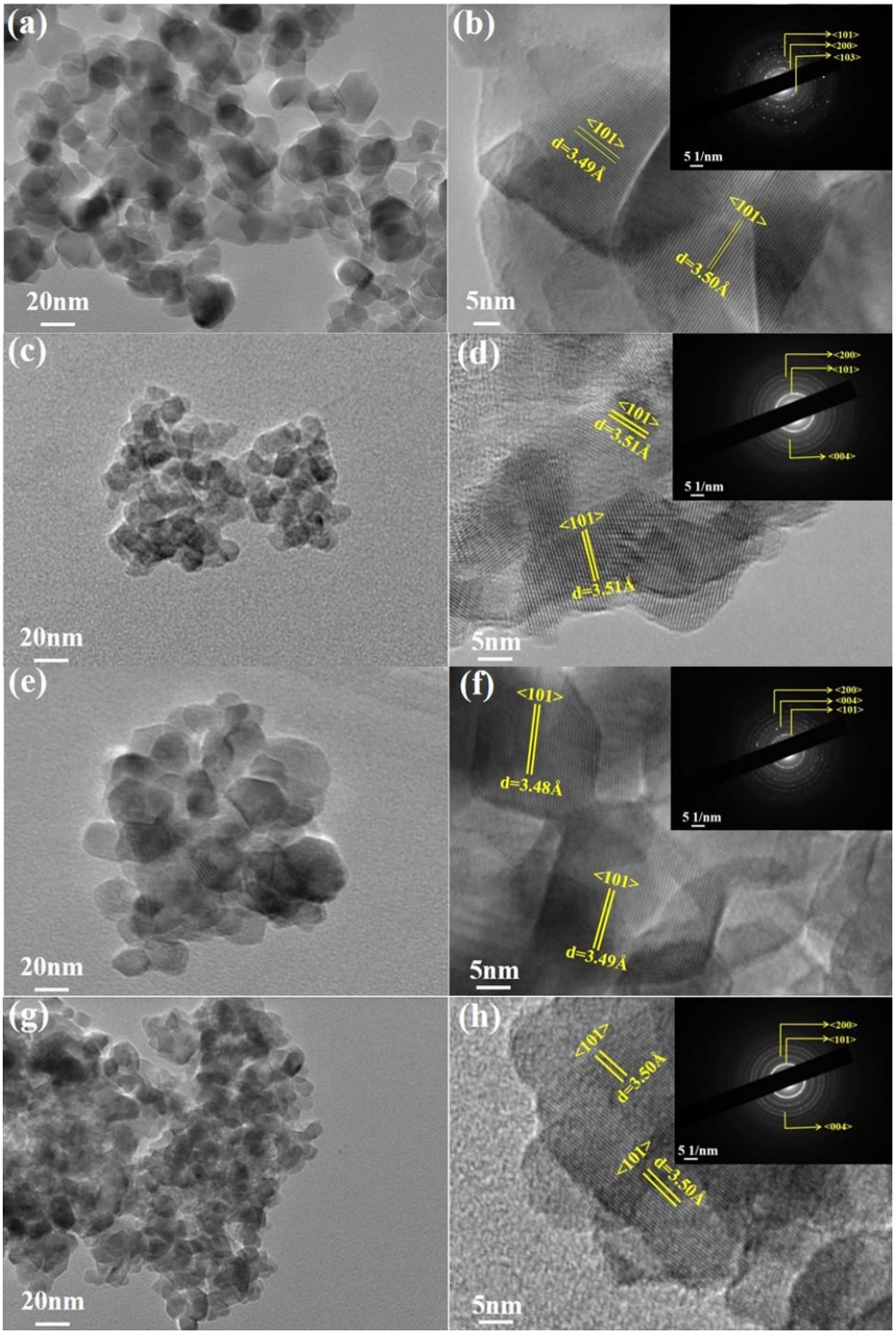

Figure 56. HRTEM and SAED images of TiO_2 nanoparticles P25 (a-b), SDS (c-d), CTAB (e-f), and DTAB (g-h)

3.2.4. BET surface area analysis

The surface area and porosity of the samples were calculated from N_2 adsorption-desorption and BJH pore size distribution experiments (Figure 57).

For the sample of P25 the BET specific surface area is 56.64 m^2/g with BJH pore size of 56.21 nm and the average pore volume is 0.767 cc/g. CTAB nanoparticles exhibits a BET surface area of 90.03m^2/g with BJH pore size of 19.27 nm and their pore volume is 0.370 cc/g. In the case of DTAB sample, the BET surface area increases to 110.81 m^2/g with BJH pore size of 13.01 nm and the pore volume is 0.295 cc/g. In comparison to all the samples SDS has the maximum BET surface area of 123.86m^2/g with the BJH pore size of 5.7 nm and the pore volume is 0.290 cc/g.

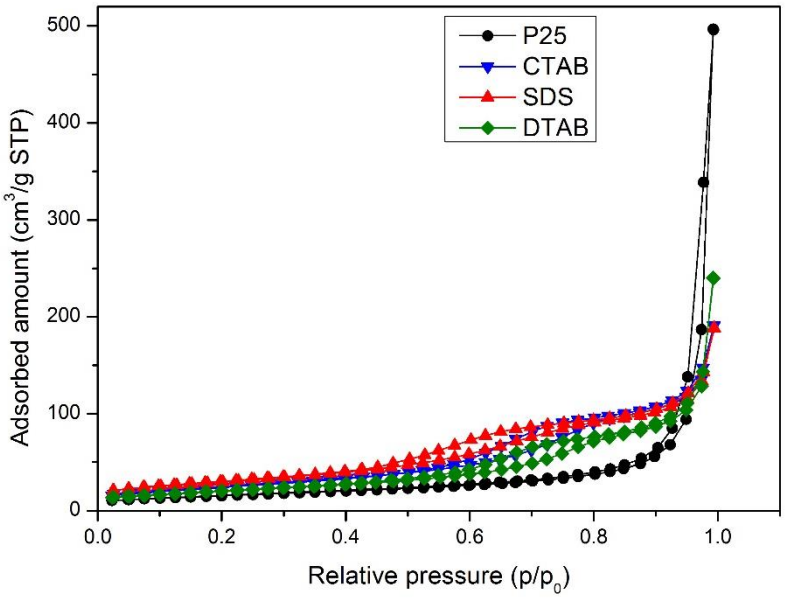

Figure 57. N_2 adsorption-desorption isotherms of the mesoporous TiO_2 nanoparticles

It is clear from the Table 7 that the surface area of SDS sample is more than two times higher than the commercial P25 powder. This surface area property could influence the photovoltaic performance of the dye sensitised solar cells fabricated form the synthesised nanoparticles [183].

Table 7. Surface parameters of the mesoporous TiO_2 nanoparticles from nitrogen physisorption measurements

Sample	Crystallite Size (nm)	BET Surface Area (m^2/g)	BJH Pore Size (nm)	BJH Pore Volume (cc/g)	Zeta Potential* (mV)	Polydispersity index (PDI)*
P25	23	56.64	56.21	0.767	-14.65	-0.82
CTAB	14	90.03	19.27	0.370	+11.47	2.31
SDS	10	123.86	5.7	0.290	-12.72	1.88
DTAB	12	110.81	13.01	0.295	+7.46	2.11
* In aqueous solution						

3.2.5. Optical Properties

Figure 58 shows the UV-Vis absorption spectra of P25, CTAB, SDS and DTAB. The curve of P25 shows the band edge at 325.45 nm and CTAB and SDS show the band edges at 333.52 and 334.53 nm, respectively. For DTAB the band edge appears to be a bathochromic shift to 339.14 nm [184].

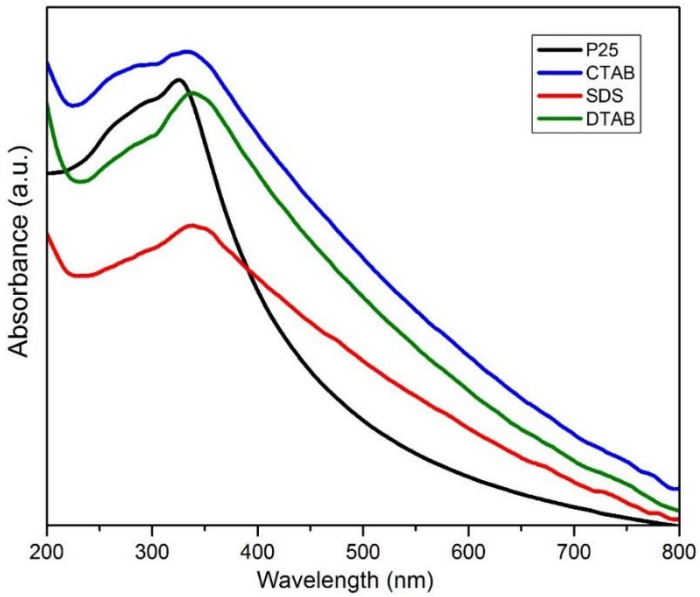

Figure 58. UV-Vis absorption spectra of P25, CTAB, SDS and DTAB samples,

Comparison of the volume occupied by the commercial TiO_2 (P25) and the prepared mesoporous titania nanoparticles is given in Figure 59. It is clear that all the synthesised nanopowders occupy less volume than the commercial one, even though they have high surface area. So, the packing density of the mesoporous TiO_2 is higher than the commercial titanium oxide powder. Generally high packing density slows the electron transport in TiO_2 nanoparticles. On the other hand, increase in packing density could improve the absorption, which can improve the electron generation in the PV device [185].

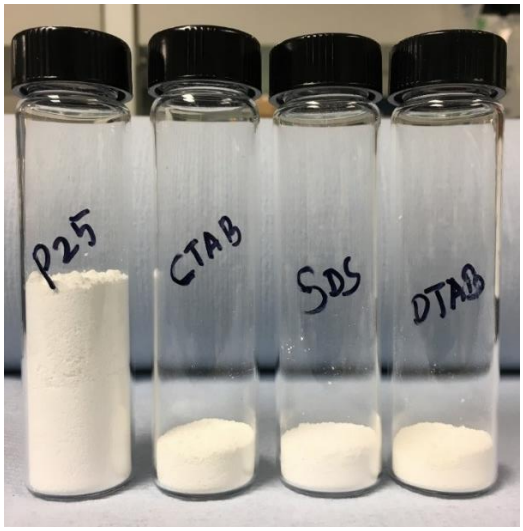

Figure 59. Comparison of synthesised mesoporous and commercial TiO_2 samples (2g each)

3.2.6. Dye loading properties

The amount of dye loading on the semiconductor surface was measured by the dye desorption method. Table 8 compares the dye loading properties of the prepared electrodes using different TiO_2 powders. Mesoporous powder prepared using SDS has more number of dye molecules attached on the surface than other samples. High surface area of the SDS mesoporous titania increases the dye loading capacity which could improve the photocurrent generation of the device [186].

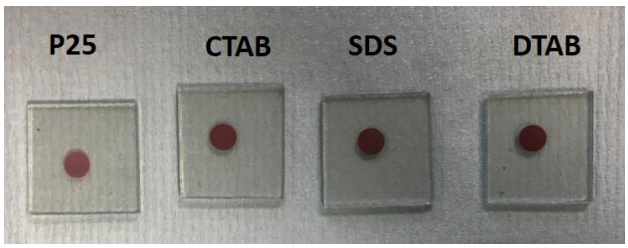

Figure 60. Digital image of the dye-sensitised photoanodes

Table 8. Dye loading properties of the sensitised TiO_2 electrodes

Sample	Absorbance @444 nm	Concentration	Moles	No. of dye molecules	Area of the dye	Dye area / 1cm^2 of TiO_2
P25	0.5619	$1.14E^{-05}$	$3.44E^{-08}$	$2.07E^{+16}$	704.37	2492.48
CTAB	0.7549	$1.54E^{-05}$	$4.62E^{-08}$	$2.78E^{+16}$	946.31	3348.59
SDS	0.9658	$1.97E^{-05}$	$5.91E^{-08}$	$3.56E^{+16}$	1210.68	4284.10
DTAB	0.8672	$1.76E^{-05}$	$5.30E^{-08}$	$3.19E^{+16}$	1087.08	3846.73

3.2.7. Photovoltaic performance

Figure 61 depicts the photovoltaic performances of the fabricated DSSCs using mesoporous TiO_2 nanoparticles synthesised from CTAB, SDS and DTAB soft templates and P25 for comparison. It is clear from Table 9 that the performance of the synthesised titania devices is much better than the P25 commercial powder cells.

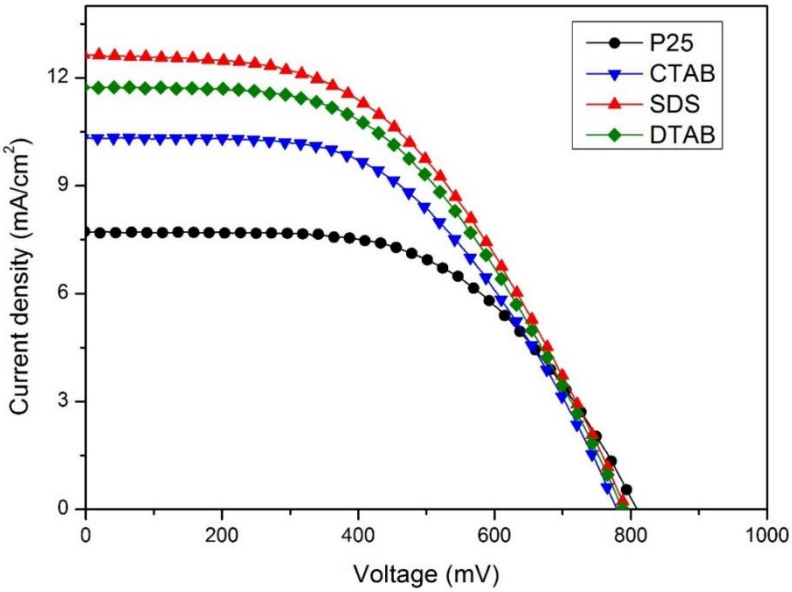

Figure 61. Photocurrent density-voltage curves of the DSSCs fabricated from the TiO_2 samples synthesized using CTAB, SDS and DTAB surfactants.

Eventhough P25 device gets the highest open circuit voltage and fill factor, the short circuit current density of the device is lower than the other devices. Bigger particle size and smaller surface area make the P25 dye adsorption less. On the other hand, the highest current density of 12.63 mA/cm2 is observed in the SDS based device. But the fill factor of 48.5% is the least for all the devices, still the overall efficiency is higher due to high current generation. Open circuit voltage is almost similar for all the devices, also not much difference in the fill factor for all the synthesised powder devices. Due to the small particle size and high surface area, the soft template TiO_2 devices show better current, so the overall device efficiency of the devices is higher than the P25 device [187].

Table 9. Photovoltaic performance parameters of the devices fabricated from meso-TiO_2 powders measured under 1000W/m^2 illumination

Device	J_{sc} [mA/cm^2]	V_{oc} [mV]	FF [%]	Efficiency [%]
P25	7.71	809	56.6	4.60
CTAB	10.31	780	52.0	5.23
SDS	12.63	793	48.5	6.08
DTAB	11.72	788	50.1	5.79

3.2.8. Charge transport properties

To understand the charge transport in DSSC interfaces, electrochemical impedance spectroscopic studies were performed. Generally, in Nyquist plots the first gap (Rs) is related to the sheet resistance on the transparent conductive oxide (TCO) substrate and the contact resistance between TCO and TiO_2. Moreover, maximum of three semi circles can be observed, first semicircle in high frequency region is attributed to the resistance at the counter electrode/electrolyte region (Rct-Pt), the second semicircle observed in the mid frequency region represents the charge transport at the TiO_2/dye/electrolyte interface (Rct(TiO_2/dye)), and the third semicircle at low frequency region corresponds to the diffusion in the iodide/tri-iodide electrolyte [188]. Figure 62 shows the Nyquist plots of the characterized devices, only two semicircles are observed for all the devices. As shown in Table 10, all the DSSCs show similar values of Rs, which is attributed to the use of the same Pt counter electrodes and I^-/I_3^- electrolyte in all the devices [189].

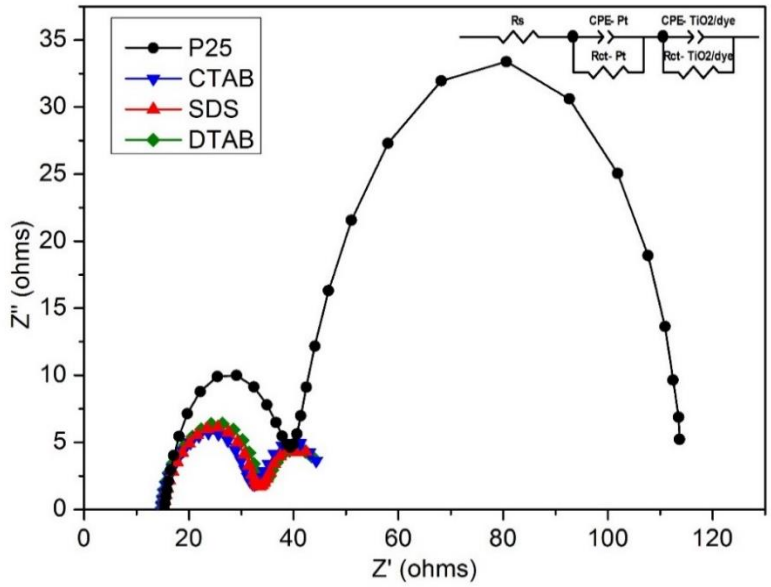

Figure 62. Nyquist plots and equivalent circuit (inset) of the DSSCs fabricated from the meso TiO_2 samples under dark condition in open circuit voltage. Experimental data are shown in the symbols, and the equivalent circuit fits are shown in the lines

On the other hand, resistance at the Pt/electrolyte interface is higher for the P25 device. Importantly, the charge transport resistance of 76.11Ω at the TiO_2/dye/electrolyte interface for the P25 device is much higher than 14.32Ω, 12.60Ω, and 12.61Ω for CTAB, SDS, and DTAB devices respectively. This shows that the bigger particle devices exhibit the higher charge transport resistance. The devices fabricated with smaller particles exhibit lower charge transport resistance. The lowest resistance of all devices is SDS device with 10 nm particles. So, the smaller the particle is the lower interfacial resistance, which reflects in better solar cell performance [190].

Table 10. The charge transport parameters of the devices under dark condition

Device	Rs (Ohms)	Rct (Pt) (Ohms)	Rct (TiO_2/dye) (Ohms)
P25	15.39	24.51	76.11
CTAB	14.65	17.99	14.32
SDS	15.09	18.51	12.60
DTAB	14.53	19.92	12.61

3.2.9. Summary

Highly crystalline mesoporous TiO_2 nanoparticles were synthesized using CTAB, SDS and DTAB surfactants as soft templates. As-synthesized mesoporous titanium dioxide samples were characterized by PXRD, FESEM, HRTEM, UV-Vis and surface area measurements, used as photo-electrode material in DSSCs. Meso-TiO_2 synthesized using SDS template exhibits high surface area of 123 m^2/g with 5.7 nm uniform pore with size. The highest power conversion efficiency of 6.08% and with photo current density of 12.63 mA/cm2 was achieved due to enhanced light harvesting, which is attributed to high surface area. The photovoltaic performance of the mesoporous TiO_2 is significantly higher than the commercial P25 titania electrode devices. The internal resistance of the cells was studied with EIS analysis, which shows smaller charge transfer resistance for the soft template prepared devices compared to the commercial P25 powder device. These results clearly suggest that simple soft template method used in this work to synthesize mesoporous TiO_2 can be an effective process for mass production in industries for various metal oxide applications.

3.3. An extended π-conjugated heteroleptic ruthenium(II) complex as a sensitiser in DSSC

3.3.1. Introduction

DSSCs have achieved encouraging power conversion efficiencies of >10% for metal free dyes, >11% for metal complex and 13% for porphyrin-based sensitisers [191–193]. As sensitisers take part in the absorption of solar radiation and injection of electrons into the conduction band of semiconductors, extensive research has been focused on the design of efficient and durable sensitisers. Several dyes have been investigated such as metal complexes, metal-free organic dyes, tetra pyrrolic porphyrin and phthalocyanine based sensitisers [194–196]. Among them, the most successful charge transfer sensitisers are ruthenium-based dye molecules, because of their strong and broad metal to ligand charge transfer absorption bands, the stability of their oxidized form and longevity of photo excited states. Grätzel and co-workers have reported >11% efficiency with cis-di(thiocyanato)-bis[2,2'-bipyridyl 4,4'-dicarboxylic acid] ruthenium(II)(N3) and trithiocyanato-4,4'4"-tricarboxy-2,2':6',2"-terpyridine ruthenium(II) (the black dye) as sensitisers [197]. Many efforts have been made to design the ligands of ruthenium complexes to improve the spectral response to near IR region and device performance.

By substituting the two long alkyl chains on the bipyridyl ligand (Z907), Zakeeruddin and co-workers achieved impressive stability under both thermal and light conditions [198]. However, the molar extinction coefficient of sensitiser is somewhat lower than that of the standard N-719 dye. Thus, extended π-conjugation has been introduced into the ligands to improve the molar extinction coefficient. For instance, Z910, which contains 3-methoxystyryl on bipyridine ligand exhibited 10.2% efficiency and remarkable stability [199]. Based on these

results several dyes have been developed using different substituents on styrene moiety of bipyridyl ligand- K19, K77, HRD and electron donors on bipyridine ligands such as triphenylamine, carbazole and coumarin etc [200–203]. By using electron donating substrates charge recombination decreased drastically, as these forms long charge separated state lifetimes. Wu and co-workers incorporated alkyl thiophene substituted bipyridine as an ancillary ligand on the ruthenium metal complex (CYC-B1, C101), as a consequence, the MLCT band has shifted to the red region and the energy levels of metal center can be raised for better charge injection and recombination [204,205].

The objective of this work is to re-design and synthesis HRD-1 complex by introducing thiophene moiety between the 3,5-di-tert-butyl phenyl group, also extending π-conjugation of bipyridine ligand to get heteroleptic Ru(II) (m-HRD-1) complex in order to further improve the absorption properties and also to tune the energy levels. Moreover, characterization of the complex by various spectroscopic techniques and it's DSSC performance using liquid I^-/I_3^- redox couple. The structure of m-HRD-1 and its ligand are shown in Figure 63.

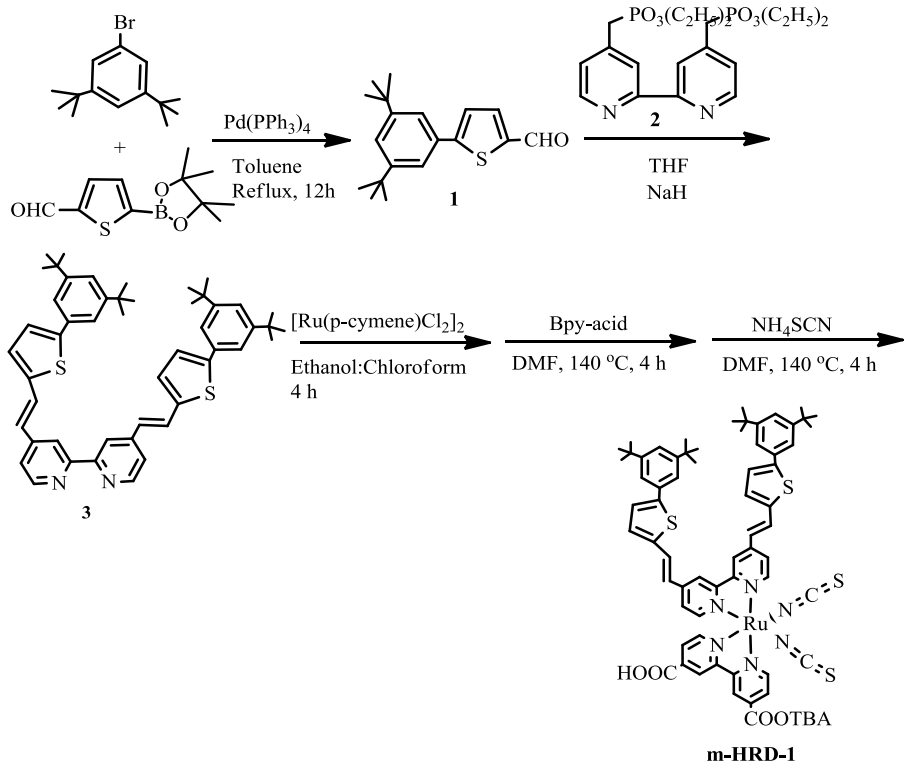

Figure 63. Synthetic scheme of m-HRD-1.

3.3.2. Experimental Methods

Synthesis of the sensitiser, device fabrication and characterization methods are given in chapter 2.

3.3.3. Optical Properties

Figure 64 reveals the absorption spectra of m-HRD-1 in ethanol and the corresponding data are presented in Table 11. The absorption bands between 450 to 550 nm regions can be attributed to the metal to ligand charge transfer transitions in singlet manifold (^{1}MLCT). The absorption maximum of m-HRD-1 is centered at 538 nm with a molar extinction coefficient of 15,338 M^{-1} cm^{-1}. The MLCT band of m-HRD-1 is bathochromically shifted when compared to HRD-1, probably due to the extended π-conjugation. Intraligand π-π* transitions bipyridine ligand are located at 300 nm. I have also measured absorption spectra of m-HRD-1 on an opaque TiO_2 film (6 μm thick). The absorption spectra in

solution and on TiO_2 were similar except for a slight red shift in absorption maxima due to the interaction of anchoring groups to the nanocrystalline TiO_2 surface. The emission spectrum of m-HRD-1 was measured in ethanol solvent at room temperature and presented in Figure 64. The complex m-HRD-1 shows emission maxima at 755 nm, when excited at MLCT band of m-HRD- complex. I have observed quenched emission spectra, when m-HRD-1 complex adsorbed on a 6 μm thick nanocrystalline TiO_2 layer, as a consequence of electron injection from the excited state of Ru(II) complex to the conduction band of TiO_2. From the absorption and emission spectra, it was found that the singlet state ($E_{0\text{-}0}$) energy of m-HRD-1 and HRD-1 are 1.94 & 1.90 eV, respectively. Quenched emission spectrum of m-HRD-1 was observed when adsorbed.

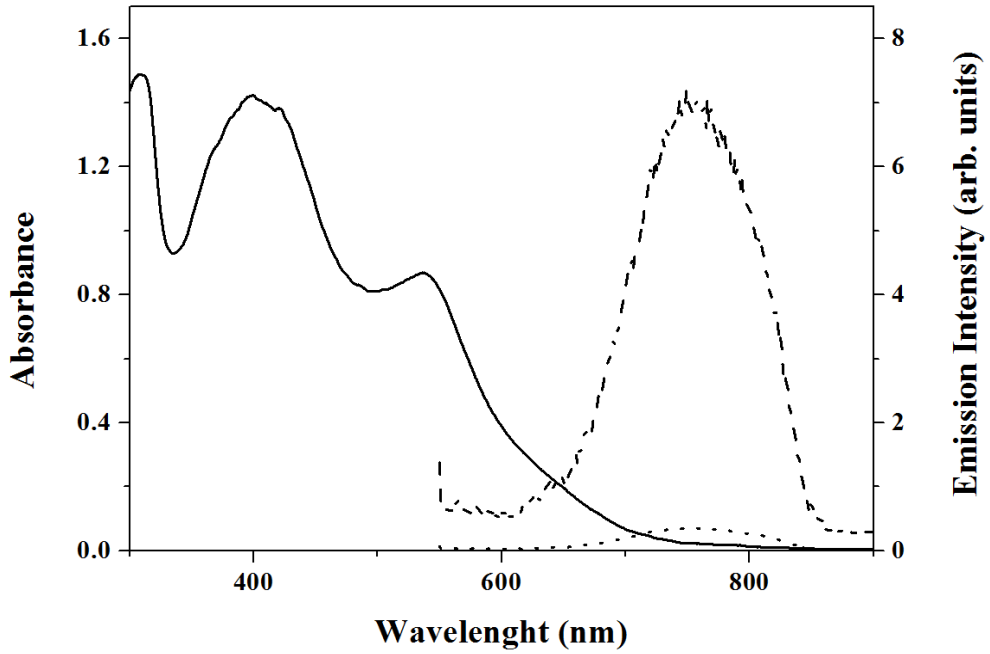

Figure 64. Electronic absorption (———) and emission (-------) spectra of m-HRD-1 in ethanol solvent. Emission (.....) spectra m-HRD-1 adsorbed onto a 2 μm thick TiO_2 film.

Table 11. UV-Visible, emission and electrochemical data for HRD-1 and m-HRD-1

Sensitiser	**λ_{max}, nm, ε (mol^{-1} cm^{-1})[a]**	**λ_{em}, nm[b]**	**$E_{1/2}$ V vs. SCE[c]**		**E_{0-0}, eV[d]**	**E_{ox}^{*}**
			Ox	**Red**		
m-HRD-1	538 (15,338)	755	0.67	-0.95	1.94	-1.27
HRD-1	543 (19,300)	720	0.75	-0.94	1.90	-1.15

3.3.4. Electrochemical Properties

The redox potential of m-HRD-1 was evaluated by using cyclic and differential pulse voltammetric techniques in DMF solvent with 0.1 M tetrabutyl ammonium perchlorate as a supporting electrolyte and their data was compared to the standard sensitiser HRD-1 in Table 11 (Figure 65). From the Table it is clear that m-HRD-1 undergoes one electron reversible oxidation at 0.67 V vs. SCE. The oxidation process can be readily assigned to the Ru(II)/Ru(III) redox couple. It also undergoes two reductions at -0.95, corresponding to the reduction of ancillary bipyridine ligands. The excited oxidation potential of m-HRD-1 is 1.27 V, which is above the conduction band of TiO_2 [206].

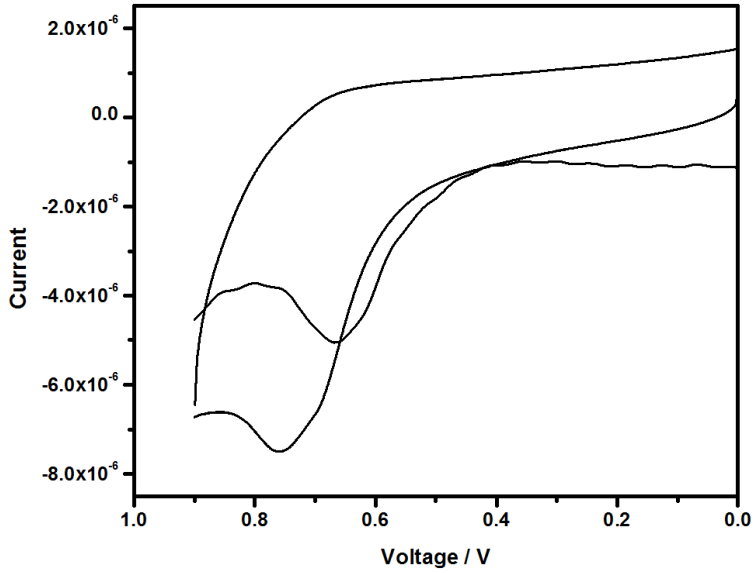

Figure 65. Cyclic and differential pulse voltammogramme of m-HRD-1.

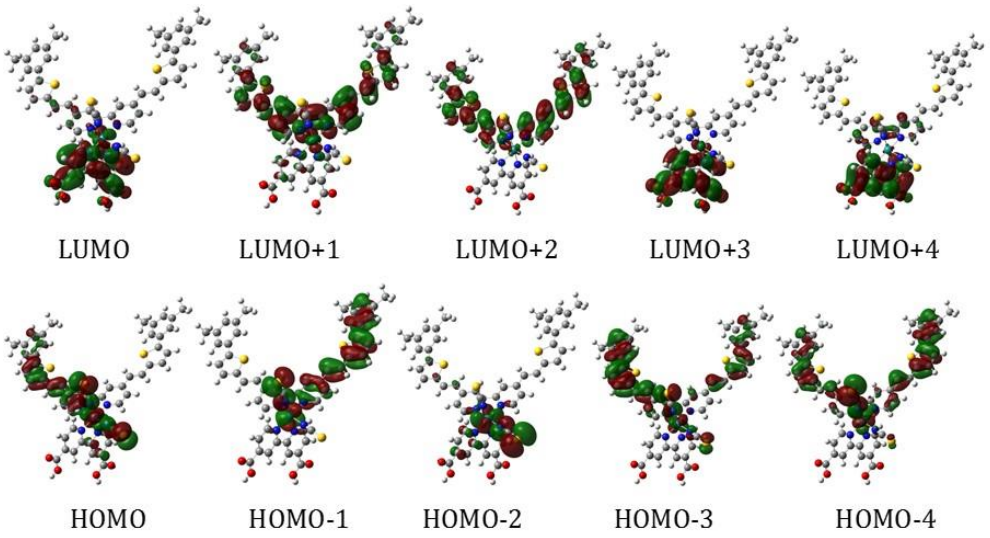

Figure 66. Molecular orbital and spatial orientation of m-HRD-1.

To identify the electronic distribution of the m-HRD-1 sensitiser, DFT calculations were performed of its electronic ground state using mPW1PW91 method for the geometry optimization with LANL2DZ basis function on Ru and 6-31g(d) basis function on C, H, N, O and S. It can be seen from Figure 66, HOMO, HOMO-1, HOMO-2, HOMO-3 & HOMO-4 are the electrons delocalized over the

Ru(II) metal and –NCS ligand. The LUMO, LUMO+1, LUMO+2, LUMO+3 & LUMO+4 are π* orbitals delocalized over the bipyridine carboxylic acid ligand facilitating electron injection from the excited state of the m-HRD-1 sensitiser to the conduction band of TiO_2. These results are in line with other ruthenium(II) polypyridyl complexes reported in the literature [207].

3.3.5. Photovoltaic properties

The performance of the DSSCs was evaluated based on their steady state current- voltage characteristics. Figure 67 depicts the photocurrent density versus photovoltage(J-V) curves of the DSSCs based on standard N719 and m-HRD-1 sensitisers. The photovoltaic parameters including the short circuit current density (J_{sc}), open circuit voltage (V_{oc}), fill factor (FF) and the power conversion efficiency (PCE) corresponding to the DSSCs are summarized in Table 12. It can be seen that DSSC based on m-HRD-1 dye shows higher photovoltaic performance than the standard N719 dye device. The observed power conversion efficiency is found to be 6.10% under 1.0 sun irradiation (J_{SC} = 18.15 mA/cm^2, V_{OC} = 705 mV, ff = 0.48) using m-HRD-1. Whereas, the device based on N719 sensitiser [J_{sc} = 14.07 mA cm^{-2}, Voc = 668 mV, and ff = 0.49] shows a photovoltaic conversion efficiency of 4.70%. The m-HRD-1 dye based device shows 20% increase in short circuit current due to the better anchoring of dye molecules and thus an increase in overall conversion efficiency.

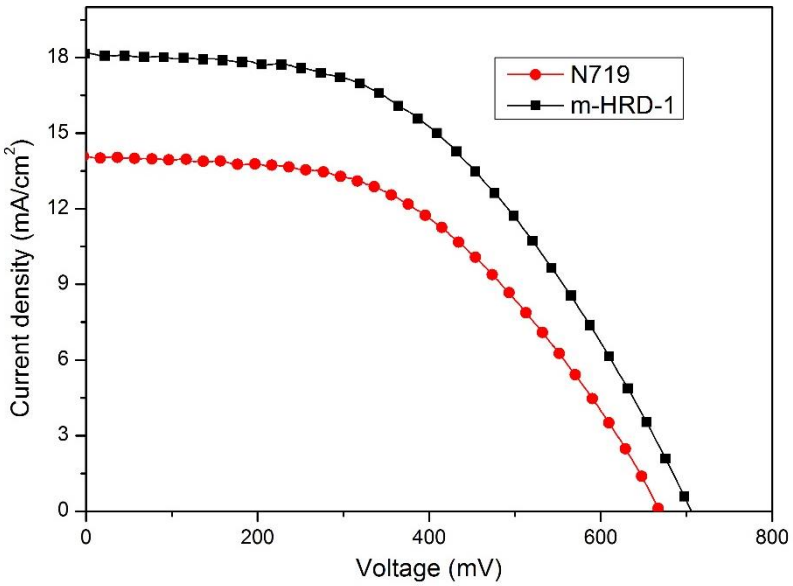

Figure 67. Comparison of J-V characteristics of DSSCs based on standard N719 and m-HRD-1 sensitisers.

Table 12. Photovoltaic parameters of the DSSCs based on N719 and m-HRD-1 sensitisers

Sensitiser	J_{sc} [mA/cm^2]	V_{oc} [mV]	FF [%]	Efficiency [%]
N719	14.07	668	49	4.7
m-HRD-1	18.15	705	48	6.1

3.3.6. Thermal Studies

The thermal stability of the new ruthenium(II) polypyridyl sensitiser is examined and compared to the thermal stability the standard sensitiser N719 using thermogravimetric analysis. Figure 68 shows the thermal behavior of m-HRD-1, clearly indicating that the sensitiser m-HRD-1 is stable up to 270 ^{o}C. The initial

weight loss between 250 to 290 ^{o}C is attributed to the removal of the carboxyl group. In contrast, the standard sensitiser N719 is stable up to 200 ^{o}C.

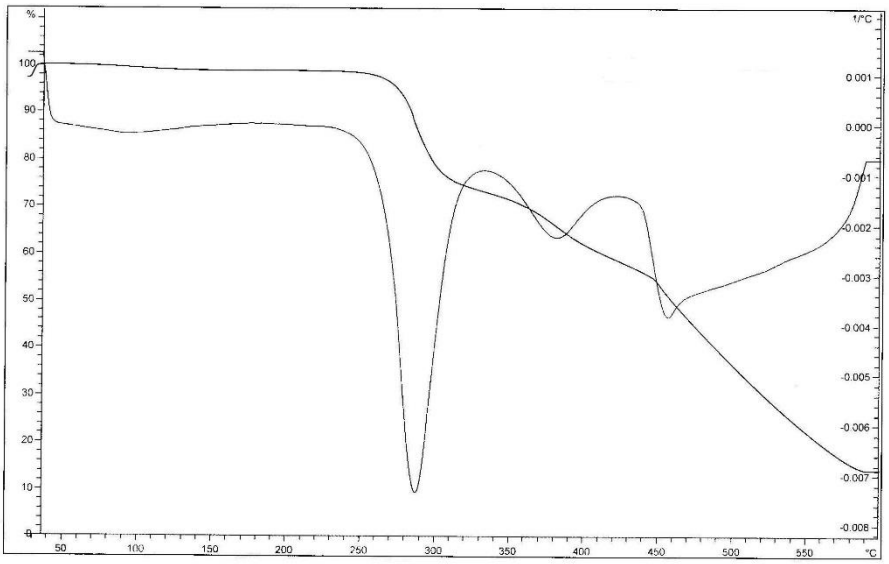

Figure 68. TG/DTG curves of m-HRD-1 with heating rate of 10^{o}C min^{-1} under nitrogen.

3.2.7. Summary

I designed and synthesized a new heteroleptic Ruthenium(II) polypyridyl complex having an extended π-conjugation. The complex m-HRD-1 was characterized by various spectroscopic techniques. Both elemental analysis and ESI-MS confirmed the presence of one TBA molecule in its molecular structure. MLCT band of m-HRD-1 was observed at 538 nm in DMF solvent. The emission spectra of m-HRD-1 quenched when adsorbed on TiO_2 film as a consequence of electron transfer. Finally, I tested the performance of m-HRD-1 in dye-sensitised solar cells using I^-/I_3^- redox couple and compared to that of the standard sensitiser N719. Thermal studies of m-HRD-1 complex suggested that it is stable up to 270^{o}C, which is better thermal stable than standard N719 sensitiser.

3.4. Copper zinc tin sulphide film as low cost platinum-free counter electrode in DSSC

3.4.1. Introduction

In DSSCs the photoelectrons or oxidative electron carriers collected from the photoanode are be transported to the cathode, which initiate catalytic reduction reactions with target electrolyte and thus sustain the electricity or fuel generation in the cell. This clearly implies that the electron driven catalyst platinum (Pt) is an indispensable component to demonstrate electrochemical process in DSSCs. However, availability and materials cost limits industrial deployment of Pt catalyst at large scale. The less expensive semiconductor materials are proposed as the Pt-free catalyst in DSSCs [208,209]. Compared to Pt, the cathode electrodes of transition metal oxides, sulphides, nitrides and carbides exhibited promising electrocatalytic performance in DSSCs. In particular, sulphide based electrocatalysts have the merits in easy synthesis, chemical stability, and excellent electrocatalytic property [210–212]. Recently, the quaternary semiconductor CZTS perceived profound attention as the Pt-free electrocatalyst in DSSCs owing to its abundance, low toxicity [213–216], and high hole concentration [217] of approx. 1.2 $x10^{15}$– 3.1$x10^{20}$ cm^{-3} providing high p-type electrical conductivity. This may anticipate high appealing class of electron-driven catalyst materials in electrochemical reduction reaction at DSSCs.

The CZTS films can be either synthesized directly on substrates or deposited from the already available nanocrystals. Among the available coating techniques, spray coating attracted much interest in catalyst and photoabsorber industry owing to its technical merits of low cost, the fabrication on large area, precise controllability of the electrode thickness, and possibility of doping and of hetero/multilayer formation. Compare to conventional spray coater, our recent

efforts on JNS coating showed more technical advantages on precise controllability in aerosol distribution, which results in smooth film surface and well-defined crystallite edges [218]. This may anticipate producing homogenous and highly reactive CZTS catalyst film. In this section, direct grown CZTS films using the JNS spray coating is demonstrated. The photocatalytic behaviour and PV performance of the CZTS films as counter electrodes in DSSCs are studied.

3.4.2. Experimental

Deposition and characterization of the thin films also DSSC fabrication and PV measurement are given in the chapter 2.

3.4.3. Photocatalytic behaviour

In order to examine catalytic activity of the synthesised CZTS electrode in tri-iodide reduction, CV of CZTS coated FTO electrodes (CZTS/FTO) was tested with iodide containing electrolyte. The resultant CV plot is compared with conventional Pt electrode (Pt/FTO) in Figure 69. The distinguished peak observed at negative potential region -0.34 V vs Ag/AgCl of CZTS 1 electrode demonstrates the catalytic activity in the trioxide reduction [158].

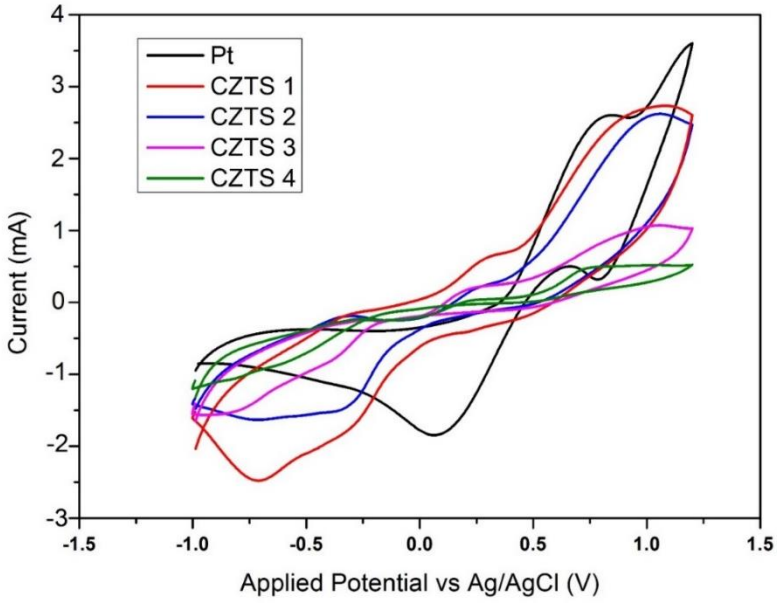

Figure 69. Cyclic voltammogram of CZTS and Pt counter electrodes measured using a three-electrode configuration

3.4.4. Photovoltaic performance

Furthermore, the photovoltaic performance of the CZTS films is tested in dye sensitised solar cells. The J-V measurements have been performed and results presented in Figure 70. The CZTS1 counter electrode based DSSC results in the photocurrent density of Jsc = 12.54 mA/cm^2, open circuit voltage Voc = 0.73 V, fill factor F.F = 43% and efficiency η = 3.91%. The DSSC with the Pt counter electrode results in the photocurrent density of Jsc = 13.95 mA/cm^2, open circuit voltage Voc = 0.79 V, fill factor F.F = 58% and overall efficiency η = 6.43%. The effective electronic conductivity and high electrocatalytic activity is responsible for the photocurrent generation by the CZTS based device. However, the smaller fill factor of (43%) this device as compared to the Pt-based cell (58%) might originate from larger electrical resistivity at the counter electrode/electrolyte interface [215]. The photovoltaic parameters of the other CZTS electrodes are given in the Table 13.

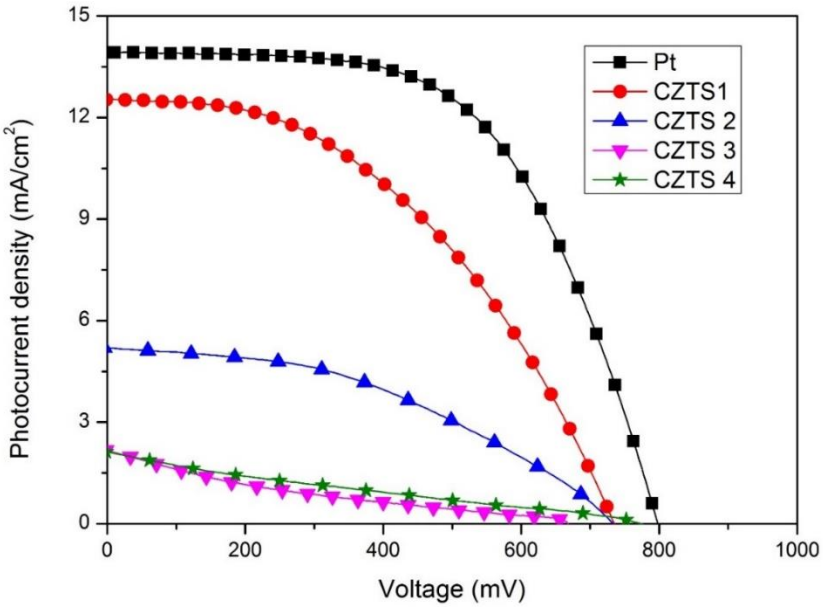

Figure 70. J-V plot of dye-sensitised solar cells fabricated with different counter electrodes (CZTS and Pt)

Table 13. Photovoltaic performance parameters of the devices based on different counter electrodes under 1000W/m^2 illumination

Device	J_{sc} [mA/cm^2]	V_{oc} [mV]	FF [%]	Efficiency [%]
Pt	13.95	797	58	6.43
CZTS 1	12.54	733	43	3.91
CZTS 2	7.21	690	27	1.34
CZTS 3	2.15	668	18	0.26
CZTS 4	2.11	736	24	0.37

3.4.5. Impedance analysis

Interfacial resistance of the device can be further examined through electrochemical impedance spectra. The resultant Nyquist plot is further simulated with the equivalent circuit as presented in the Figure 71. The simulated

charge transfer resistance value (Rct- CE) of CZTS1 electrode is 48.7 ohms, this is four times larger than that of Pt electrode (11.7ohms). The high charge transfer resistance at CZTS 1 electrode might be responsible for the small fill factor of this device as mentioned earlier [158]. The charge transfer resistance of all the CZTS 1 film can be further reduced by varying the composition, substrate temperature, or probing thickness of the electrode. EIS parameters of the other CZTS electrodes are given in Table 14.

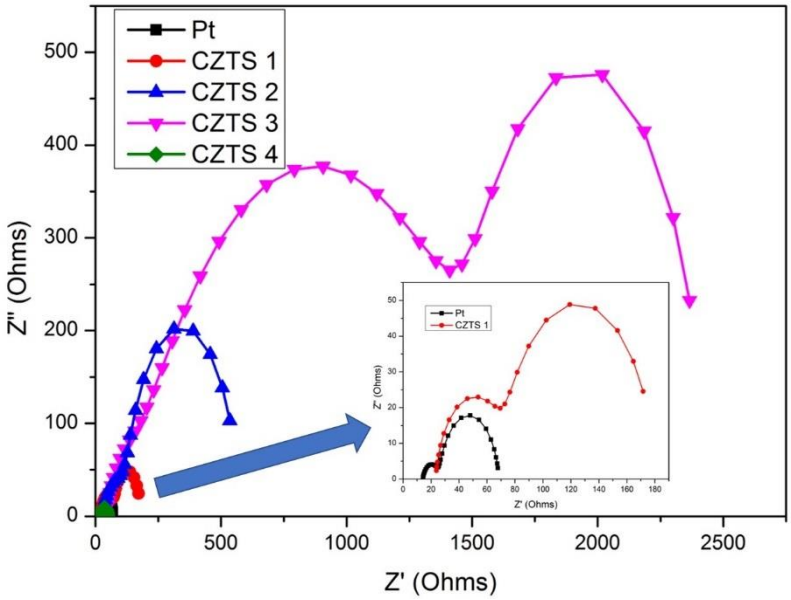

Figure 71. Nyquist plots of dye-sensitised solar cells with different counter electrodes (CZTS and Pt). The measurements were carried out under 1 sun AM1.5 illumination.

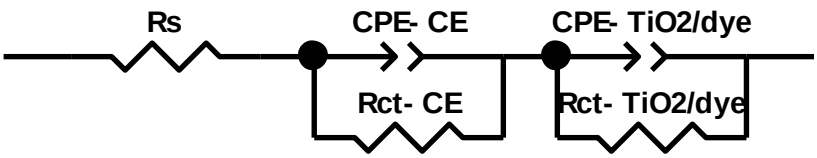

Figure 72. Equivalent circuit used for fitting the experimental data

Table 14. Comparison of the charge transport parameters of the devices under dark condition

Device	R_{ct} (CE) (ohms)	R_s (ohms)
Pt	11.7	14.07
CZTS 1	48.75	23.33
CZTS 2	97.53	41.91
CZTS 3	99.73	26.9
CZTS 4	-	25.37

3.4.6. Summary

Aero-sol controlled CZTS film was fabricated by a low cost JNS coating technique. Under identical experimental conditions, the CZTS films showed reasonable electrocatalytic performance in tri-iodide reduction reactions. Even though the photovoltaic performance of the CZTS electrodes-based devices is lower than the Pt based device, their low cost and easy fabrication encourage the implementation of these electrodes as Pt-free counter electrodes in dye solar cells for large scale applications.

3.5. Conclusions

Even though in recent times dye sensitised solar cell technology is considered as a quite assessed typical configuration, still different strategies are currently under research for the improvement of the power conversion efficiency and increasing the long-term stability of the devices. Among all the studies, improvement on the main components of the DSSCs remains the top most focus. Improving the metal oxide properties, different cost-effective simple synthesis methods, modification

of dyes, finding new redox electrolytes (liquid or solid), and low-cost counter electrodes still seem a very wide action research field. In this chapter, I have studied different methods to synthesis alternative materials for the improvement of DSSC performance. The summary of the results is,

1. The combination of high surface area, packing density and dye loading capacity significantly have an impact on the performance of mesoporous TiO_2 photoanode in DSSC.
2. A new sensitiser, heteroleptic Ruthenium(II) polypyridyl complex having an extended π-conjugation has achieved 25% higher efficiency than the commercial N719 in DSSCs.
3. A low-cost Pt free counter electrode for DSSC has shown promising photovoltaic performance

All the methods and materials used in this chapter are simple and cost effective. It is important to bring down the cost of DSSCs for their further exploitation in real-world applications like building integrated photovoltaics. Though these results are encouraging, commercial materials are used for DSSC fabrication in the upcoming chapters in order to achieve transparency and have standard comparison.

Chapter 4: Multifunctional semi-transparent DSSCs for building applications

In this chapter, the spectral behaviour of the DSSCs with different transparencies are studied. The colour rendering index (CRI) and correlated colour temperature (CCT) of the semi- transparent DSSCs are calculated for adaptive glazing application in buildings. The calculated values are compared with air filled double pane glazing and evacuated (vacuum) glazing. From the CCT and CRI analysis, three better DSSC glazing devices are found and used for further analysis. The solar factor for the devices is calculated for different light incident angles for a whole year at a particular location. The correlation between clearness index and DSSC transmittance is also studied. Moreover, glare analysis is performed for all the devices on a sunny day, intermittent day and overcast day, and is also compared with double glazing. Finally, the transmittance of the devices is measured after 2 years to understand the effects of device stability on DSSC glazing applications.

This chapter is based on the following published articles

1. A. Ghosh, **P. Selvaraj**, S. Sundaram, T.K. Mallick, *Sol. Energy* **2018**, *163*, 537
2. **P. Selvaraj** , A. Ghosh, T.K. Mallick, S. Sundaram, *Renewable Energy* **2019**, 141, 516-525

4.1. Introduction

As mentioned earlier, buildings consume 34% of world energy demand [219] for heating, ventilation, cooling and lighting load demand [220]. Mitigation of this energy demand is possible by introducing new zero energy building or retrofits using energy efficient materials. Buildings are composed of different envelopes

such as doors, roofs, walls and windows. Due to the transparent nature of a window, it has a large impact on the energy demand as well as the thermal and visual comfort of a building [221,222]. Presently available single or double glazed windows allow a considerable amount of solar heat for hot climates and excessive heat loss for cold climates, also daylight which creates glare [223,224]. Closing the windows for a fully air-conditioned building accounts for 20-30% more energy consumption from the use of artificial lighting [225].

On the other hand, smart or advanced type glazings have the potential to reduce building energy demand. Switchable and static transparent type of advanced glazings are currently available [226]. Static transparent PV glazings are promising for window applications due to their multifunctional property such as ability to control solar gain, daylight glare and generate clean electricity [82,227]. PV glazings are also known as BIPV glazing because it replaces buildings traditional windows and becomes an integral part of the building. BIPV can also replace other building envelopes such as walls and roof. However, the windows of a building are of prime importance as it is the only building envelope which maintains a relation between external environment and internal room [226]. Thus, advanced BIPV windows are required to allow soothing daylight and also to control the solar heat by using a single system. Moreover, for retrofit application, replacement of windows is easier than any other part of the building [228,229].

In this work, different transparent DSSCs are used to evaluate luminous transmittance, CCT and CRI for the incoming daylight through DSSC glazing. CCT, CRI and daylight glare index (DGI) of DSSC glazing were compared with air filled double pane glazing and evacuated (vacuum) glazing.

4.2. Experimental

Six small-scale (active area- 0.28 cm^2) semi-transparent dye-sensitised solar cells (DSSCs) were fabricated by varying TiO_2 electrode thickness. The experimental steps are given in chapter 2.

4.3. Luminous transmittance of semi-transparent DSSCs

4.3.1. luminous transmission calculation

The transmission data of the devices was measured by a UV–Vis–NIR spectrophotometer. Luminous transmittance values τ_v are given by [230]

$$\tau_v = \frac{\sum_{380nm}^{780nm} D_{65}(\lambda)\, V(\lambda)\, \tau(\lambda)\, \Delta\lambda}{\sum_{380nm}^{780nm} D_{65}(\lambda)\, V(\lambda)\, \Delta\lambda} \quad (1)$$

where τ(λ) is the spectral transmittance of DSSC glazing, D65(λ) is the spectral power distribution of CIE standard illuminant D65, V(λ) is the photopic luminous efficiency function of the human eye and Δλ = 10 nm. The standard photopic luminosity function V(λ) is also called as standard eye sensitivity and is used to define a conversion between the radiated energy (in Watts) and the luminous flux (in Lumen). Figure 73 shows the photopic eye sensitivity to light wavelength. The maximum sensitivity is in the green spectral range at 555 nm, where V (λ) has a value of unity, i.e. V (555 nm) = 1.

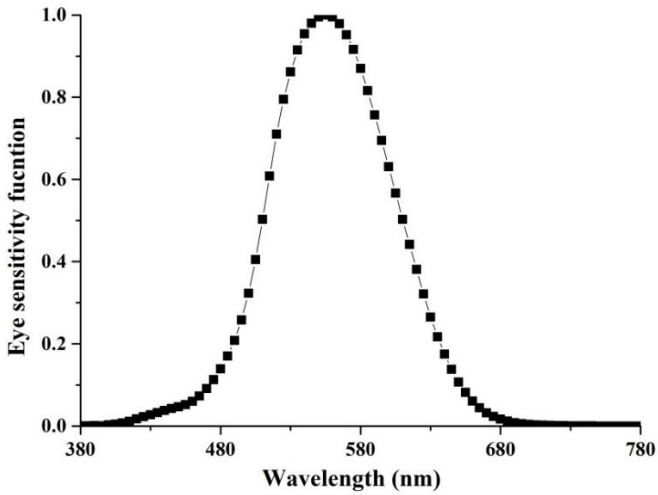

Figure 73. Standardization curve of eye sensitivity to wavelength of light [231]

4.3.2. Working electrode thickness- device transparency relationship

The transparency of DSSCs is heavily depending on the thickness of TiO_2 nanostructured materials. Figure 74 shows the transmission spectra of the fabricated DSSCs with various TiO_2 thicknesses in the range of wavelength from 380 to 780 nm.

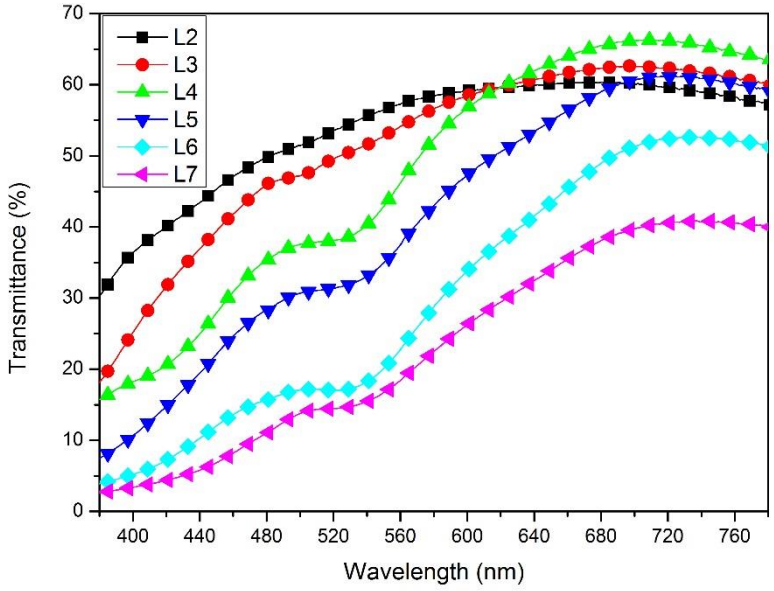

Figure 74. Spectral transmittance of the semi-transparent DSSCs.

The thinnest electrode with 3.5 µm thickness (L2) device has an average of 53% transparency in the visible range (390-700 nm). However, as the

thickness of the electrode increases, the transmittance of the solar cell gradually decreases, and the average transparency is 50%, 44%, 37%, 25% and 19% respectively for L3, L4, L5, L6, and L7 devices which is evident from the Figure 75. The average transparency of 53% was recorded for the device made with 3.5 µm thick TiO_2 electrode (L2) and the device with 14 µm thick TiO_2 electrode has 19% transparency. More dye molecules attached to the thick TiO_2 films absorb more light, leading to low transmittance, also thick films physically block/absorb the light [232].

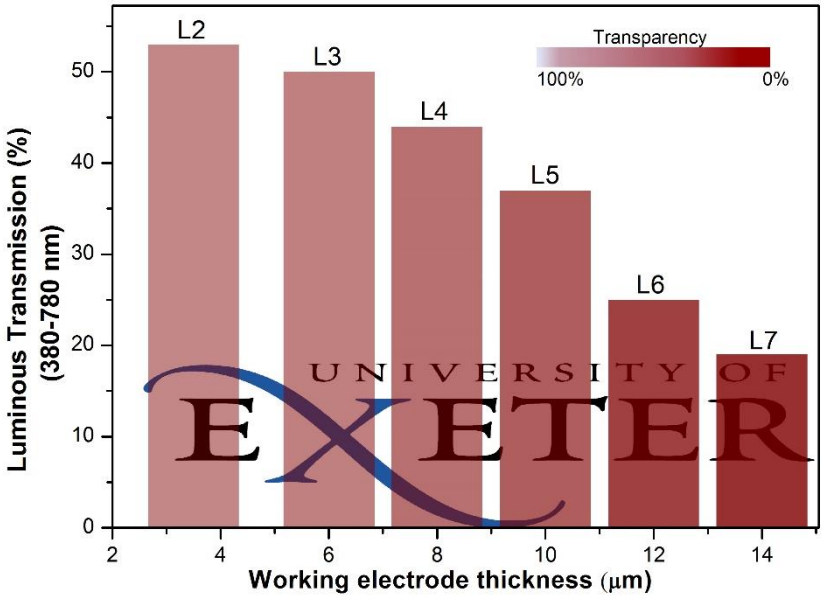

Figure 75. Effect of working electrode thickness on device transparency

4.4. Evaluation of CRI and CCT

To evaluate colour properties of the DSSC glazing, method recommended by CIE 13.3-1995 was followed. Colour is perception and not possible to measure with any equipment [233]. At first CCT was calculated. Colour matching functions corresponding to sensitivity of human eye and spectral power distribution of the wavelength dependent transmitted light were used to identify the CCT. For colour rendering index evaluation, 1931 CIE chromaticity coordinates of test colour

samples were evaluated followed by determination of 1964 CIE UCS chromaticity coordinates ($W_{t,i}$*;$U_{t,i}$*;$V_{t,i}$*). Resultant colour shift was investigated to find out special colour rendering index (R_i) which offered general colour rendering index (CRI). All calculations were processed using MATLAB 8.5.

4.4.1. CCT evaluation

The tristimulus values X, Y, Z indicate the three-colour perception of human eye response. They also indicate how much red, blue and green are in the colour. This XYZ colour system was established in 1931 and referred as 1931 2^0 CIE standard observer [231,234]. Tristimulus values X, Y and Z of transmitted light through DSSC glazing can be calculated from the measured SPD transmittance, D65 spectral power distribution and the colour matching functions as shown in Figure 76 [234].

$$X = \sum_{380nm}^{780nm} D_{65}(\lambda)\ \tau(\lambda)\ \overline{x}(\lambda)\ \Delta\lambda \tag{2}$$

$$Y = \sum_{380nm}^{780nm} D_{65}(\lambda)\ \tau(\lambda)\ \overline{y}(\lambda)\ \Delta\lambda \tag{3}$$

$$Z = \sum_{380nm}^{780nm} D_{65}(\lambda)\ \tau(\lambda)\ \overline{z}(\lambda)\ \Delta\lambda \tag{4}$$

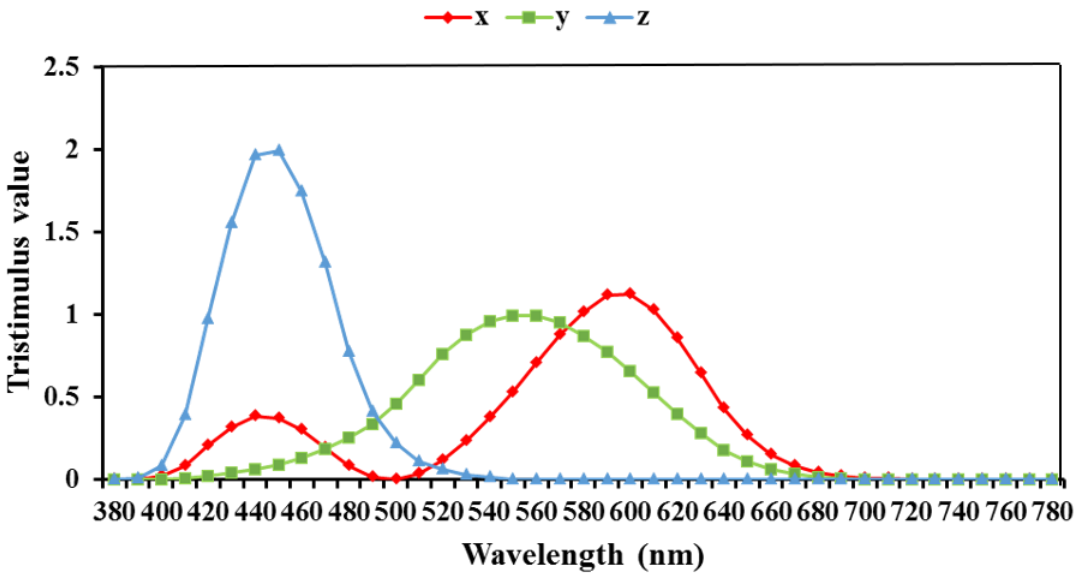

Figure 76. The spectral response of the colour matching functions

$$\bar{x}(\lambda), \bar{y}(\lambda), \bar{z}(\lambda)$$

Chromacity coordinates (x,y) can be calculated by the below equation

$$x = \frac{X}{X+Y+Z} \text{ and } y = \frac{Y}{X+Y+Z}$$

CCT was calculated from McCamy's equation [235]

$$CCT = 449n^3 + 3525n^2 + 6823.3n + 5520.33 \quad (5)$$

where $n = \frac{(x - 0.3320)}{(0.1858 - y)}$ and x,y chromacity coordinate

4.4.2. CRI calculation

Colour rendering is defined as "the effect of an illuminant on the colour appearance of objects by conscious or subconscious comparison with their colour appearance under a reference illuminant". CRI is a numerical measure of how true the colours look when viewed with the light source.

Here, for CRI evaluation tristimulus values of the light transmitted by the glazing and reflected by each of eight test colours (i=1 to 8) are given by where test colour is defined by their spectral reflectance $\beta_i(\lambda)$.

$$X_{t,i} = \sum_{380nm}^{780nm} D_{65}(\lambda)\ \tau(\lambda)\beta_i(\lambda)\,\bar{x}(\lambda)\ \Delta\lambda \tag{6}$$

$$Y_{t,i} = \sum_{380nm}^{780nm} D_{65}(\lambda)\ \tau(\lambda)\beta_i(\lambda)\,\bar{y}(\lambda)\ \Delta\lambda \tag{7}$$

$$Z_{t,i} = \sum_{380nm}^{780nm} D_{65}(\lambda)\ \tau(\lambda)\beta_i(\lambda)\,\bar{z}(\lambda)\ \Delta\lambda \tag{8}$$

Trichromatic coordinates u_t and v_t for the transmitted light were determined from

$$u_t = \frac{4X}{X+15Y+3Z} \text{ and } v_t = \frac{6X}{X+15Y+3Z} \tag{9}$$

Each test colour for the light transmitted and then reflected by the test colour i is thus given by

$$u_{t,i} = \frac{4X_{t,i}}{X_{t,i}+15Y_{t,i}+3Z_{t,i}} \text{ and } v_{t,i} = \frac{6X_{t,i}}{X_{t,i}+15Y_{t,i}+3Z_{t,i}} \tag{10}$$

Trichromatic coordinate correction after distortion by chromatic adaptation is provided by

$$u'_{t,i} = \frac{10.872 + 0.8802\frac{c_{t,i}}{c_t} - 8.2544\frac{d_{t,i}}{d_t}}{15.518 + 3.2267\frac{c_{t,i}}{c_t} - 2.0636\frac{d_{t,i}}{d_t}}\ , \tag{11}$$

$$v'_{t,i} = \frac{5.520}{15.518 + 3.2267\frac{c_{t,i}}{c_t} - 2.0636\frac{d_{t,i}}{d_t}} \tag{12}$$

Where c_t and d_t for transmitted light and $c_{t,i}$ and $d_{t,i}$ for each light transmitted and then reflected by test colour are calculated from

$$c_t = \frac{4 - u_t - 10v_t}{v_t},$$

$$d_t = \frac{1.708v_t + 0.404 - 1.481u_t}{v_t} \tag{13}$$

$$c_{t,i} = \frac{4 - u_{t,i} - 10v_{t,i}}{v_{t,i}},\ d_{t,i} = \frac{1.708v_{t,i} + 0.404 - 1.481u_{t,i}}{v_{t,i}} \tag{14}$$

Colour space system $W^*_{t,i}$, $U^*_{t,i}$, $V^*_{t,i}$ are given by

$$W^*_{t,i} = 25\left(\frac{100Y_{t,i}}{Y_t}\right)^{1/3} - 17 \tag{15}$$

$$U^*_{t,i} = 13W^*_{t,i}\left(u'_{t,i} - 0.1978\right) \tag{16}$$

$$V^*_{t,i} = 13W^*_{t,i}\left(V'_{t,i} - 0.3122\right) \tag{17}$$

The total distortion (colour difference between the colour coordinates determined for the same test colour samples illuminated by test and the reference illuminants) ΔE_i is determined from

$$\Delta E_i = \sqrt{(U^*_{t,i} - U^*_{r,i})^2 + (V^*_{t,i} - V^*_{r,i})^2 + (W^*_{t,i} - W^*_{r,i})^2} \tag{18}$$

The special colour rendering index R_i for each colour sample is given by

$$R_i = 100 - 4.6\,\Delta E_i \tag{19}$$

The general colour rendering index (CRI) is thus given by

$$CRI = \frac{1}{8}\sum_{i=1}^{8} R_i \tag{20}$$

4.4.3. CCT and CRI for DSSC glazing

Figure 77 shows the variation of CCT and CRI with device transparency. CCT was calculated using equation 5 and CRI was calculated from equation 20. The CRI includes spectrally dependent characteristics with CRI values of 95 or higher considered acceptable. A CRI close to 100 indicates an excellent visual quality. Light colour is an influential factor on indoor comfort. Colour temperature is conventionally expressed in kelvins, using the symbol K, a unit of measure for absolute temperature. Colour temperatures over 5000 K are called "cool colours" (bluish), while lower colour temperatures (2700–3000 K) are called "warm colours" (yellowish). "Warm" in this context is an analogy to radiated heat flux of traditional incandescent lighting rather than temperature [236]. A strong linear correlation was found between CCT and CRI for DSSC glazing. It can be concluded that higher achievable CRI also offers higher CCT. For indoor light condition, a CCT from 3000 K -5300 K and CRI of more than 80 are generally required [113]. To realize a high CRI, a DSSC should have an enough broad spectral coverage, but it leads to a high CCT, which is not suitable for indoor comfort. L2 (3.5 µm thick electrode) and L3 (6 µm thick electrode) devices offer better CRI and CCT compared to other layers.

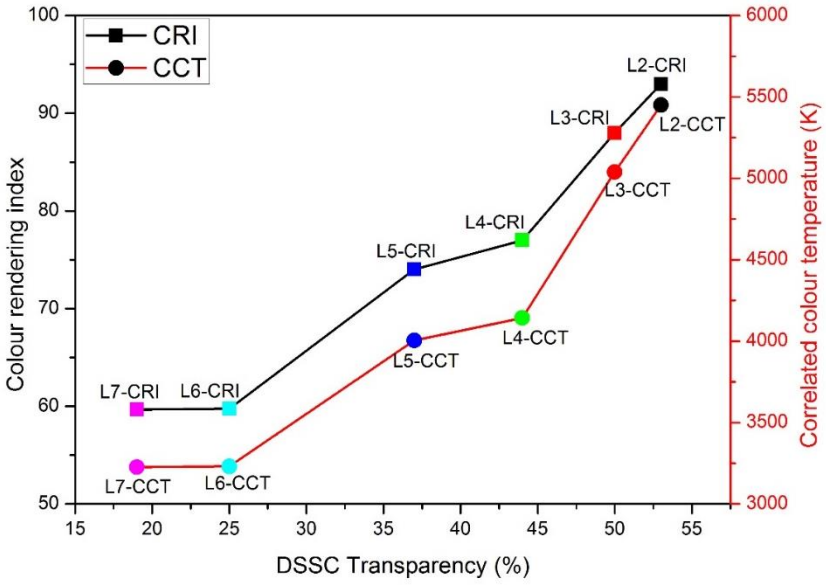

Figure 77. Variation of CCT and CRI with device transparency

4.4.4. CCT & CRI comparison of DSSC with vacuum and double glazing

Figure 78 shows the normal hemispherical transmission of 53% transparent DSSC, double and vacuum glazing. Vacuum glazing consists vacuum between two glass panes and potential to reduce heat loss in northern climatic conditions [224,237]. Double-glazing is a widely available glazing technology for building window applications [238,239]. Thus, these two glazing systems were considered in this work to compare the behaviour of adaptive DSSC glazing.

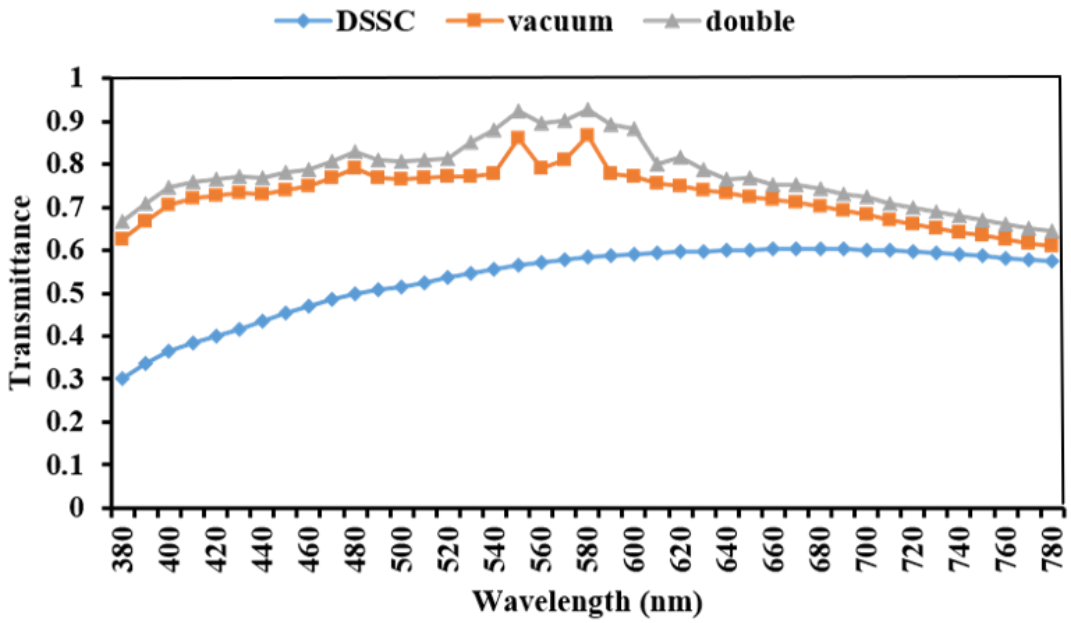

Figure 78. Comparison of the normal-hemispherical spectral transmittance of different glazings

Presence of low emission coating in the double and vacuum glazing influenced to decrease transmission after 600 nm whereas DSSC showed increasing of transmission after 600 nm. Figure 79 indicates the CCT and CRI for 53% transparent DSSC, 72% transparent vacuum glazing and 78% transparent double-glazing. DSSC glazing has 45 % less transmission compared to double glazing and 35% less than vacuum glazing, however, CRI only compromises 2.7% less compared to both glazing. It indicates that CRI depends more on the wavelength dependent spectral values than one single transmittance value.

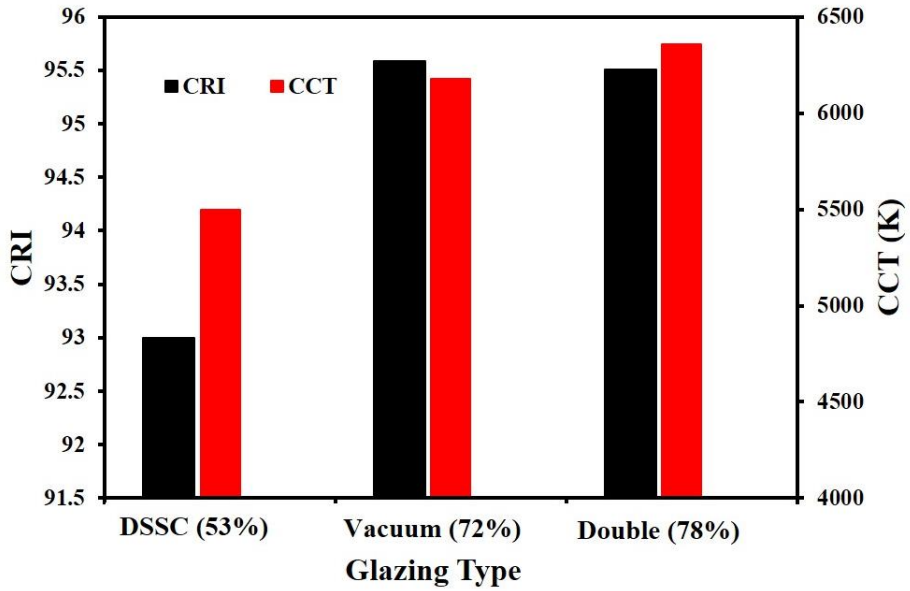

Figure 79. Comparison of CCT and CRI of DSSC (53%), Vacuum (72%) and double (78%) glazing types. Percentage of transparency is given brackets.

After comparing the results, it is found that the transparent DSSCs offer only 2.6% lower CRI and CCT values than the vacuum and double-glazing. Figure 80 compares the electrical efficiency and CRI of the devices with their transparencies (The electrical efficiency analysis is done in the next chapter). The devices with higher transparency have better CRI and CCT values. Since L5 device has the highest efficiency among all with 37% transparency and devices L2 and L3 are aesthetically suitable, I consider these three devices named as L2, L3 and L5 with 53%, 50% and 37% transparency respectively for further analysis in this work.

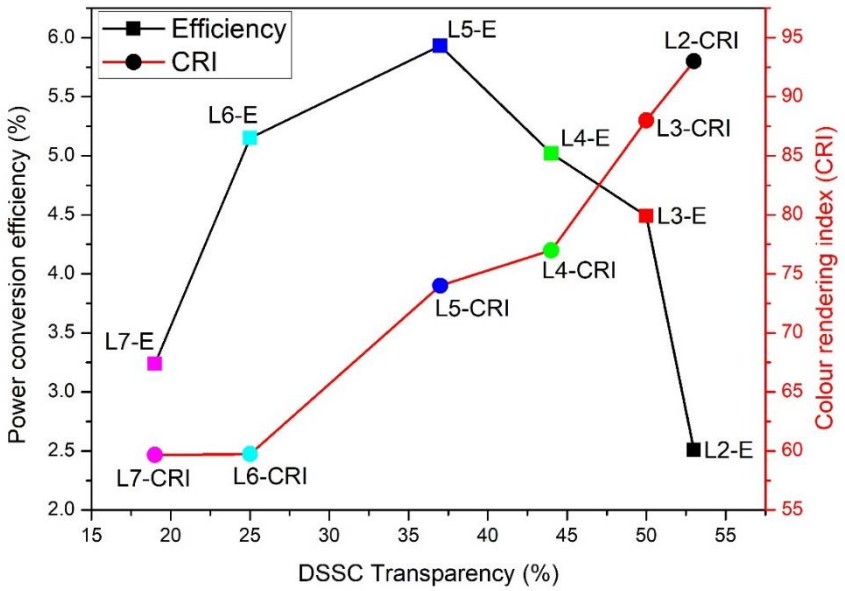

Figure 80. Comparison of electrical efficiency and CRI for DSSCs with different transparencies

4.5. Spectral behaviour of the aged DSSCs

As DSSCs have long term stability issues, the optical properties of the devices were measured after two years. Figure 81 compares the transmittance of both fresh and old devices. The transparency of the devices is decreased by 20-30% after 2 years compared to the initial measurement. This could be due to the interfacial reaction in the device. Since the electrolyte has corrosive characteristics, corrosion of the electrode in the electrolyte solution frequently occurs resulting in poor transparency of the cell. Though the electrodes are corroded, the devices still transmit the light. For glazing perspective, the durability based on transmission is comparable with other smart glazing [240].

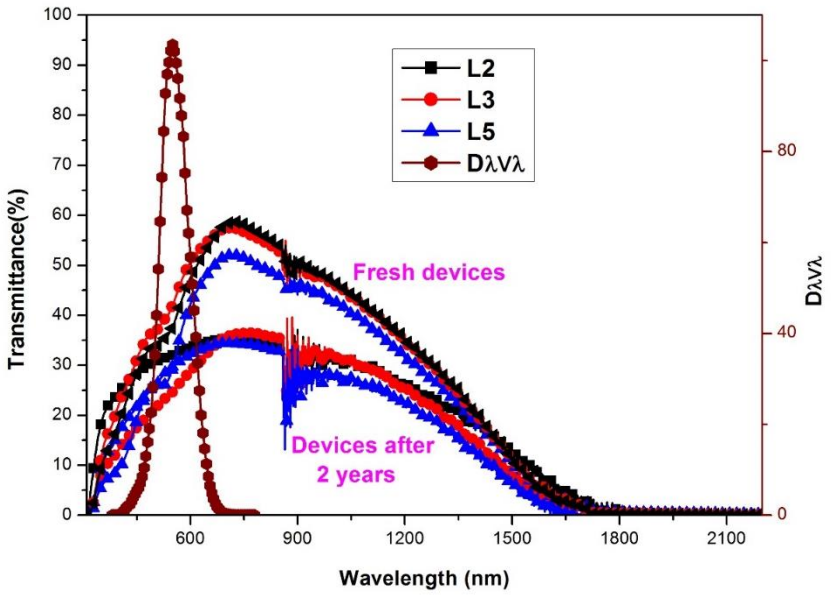

Figure 81. Comparison of transmittance of the different transparent DSSCs (Fresh and after 2 years)

4.6. Angular transmission

For any particular location glazing transmission varies with season and time of day. Thus, glazing transmission angular behaviour is more crucial than single glazing transmittance value for building energy simulation and design

Angular dependent glazing transmission is given by[241][242]

$$\tau_s(\theta)=\frac{1}{2}\left[\frac{1-\left\{\frac{\sin(\theta-n)}{\sin(\theta+n)}\right\}^2}{1+(2n_g-1)\left\{\frac{\sin(\theta-n)}{\sin(\theta+n)}\right\}}+\frac{1-\left\{\frac{\tan(\theta-n)}{\tan(\theta+n)}\right\}^2}{1+(2n_g-1)\left[\frac{\tan(\theta-n)}{\tan(\theta+n)}\right]^2}\right]\times\exp\left(\frac{-k_g N_g t_g}{\cos\theta}\right) \quad (21)$$

Where refractive index (n) and extinction coefficient (k)

$$k=-\frac{\lambda}{4\pi d}\ln t \quad (22)$$

$$n = \frac{\left(1+\sqrt{r}\right)}{\left(1-\sqrt{r}\right)} \tag{23}$$

$$r = \frac{\beta - \sqrt{\beta^2 - 4\left(2-\rho\right)\rho}}{2\left(2-\rho\right)} \tag{24}$$

$$t = \frac{\left(\rho - r\right)}{r\tau_s} \tag{25}$$

Spectral transmittance and reflectance at normal incidence are the most commonly measured optical properties of glazing. For vertical plane DSSC glazing, transmission varies with light incident angle. Here, using equation 21, incident angle dependent glazing's angular transmission was calculated from measured normal incident transmission. Figure 82 shows the angular dependency of the L2, L3 and L5 DSSC glazing devices. At the University of Exeter in Penryn, the incident angle varies from 13 degrees to 82 degrees throughout the year. For the month of January, glazing transmission is high compared to month of July.

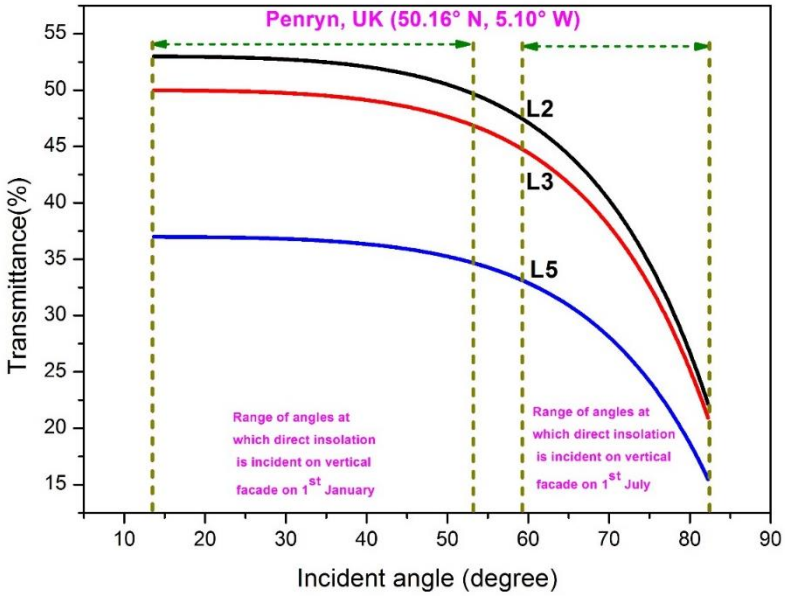

Figure 82. Variation of DSSC transmission with solar incident angle

4.7. Solar factor

The solar factor or solar heat gain coefficient of a glazing indicates the fraction of the entering incident solar radiation into a room after passing through that glazing material [243]. It also measures the transmitted solar energy through a glazing. This is the sum of the solar transmittance (τ_s) and entering infrared radiation (q_i) to a building interior [244]. Angular dependent solar transmission from equation 21 is replaced in equation 26.

$$g = \tau_s + q_i = \tau_s + \alpha \frac{h_i}{h_i + h_e} \\ = \tau_s + (1 - \tau_s - \rho_s) \frac{h_i}{h_i + h_e} \quad (26)$$

Angular solar factor (g(θ)) was evaluated using equation 27

$$g(\theta) = g(0)\tau_s(\theta) \quad (27)$$

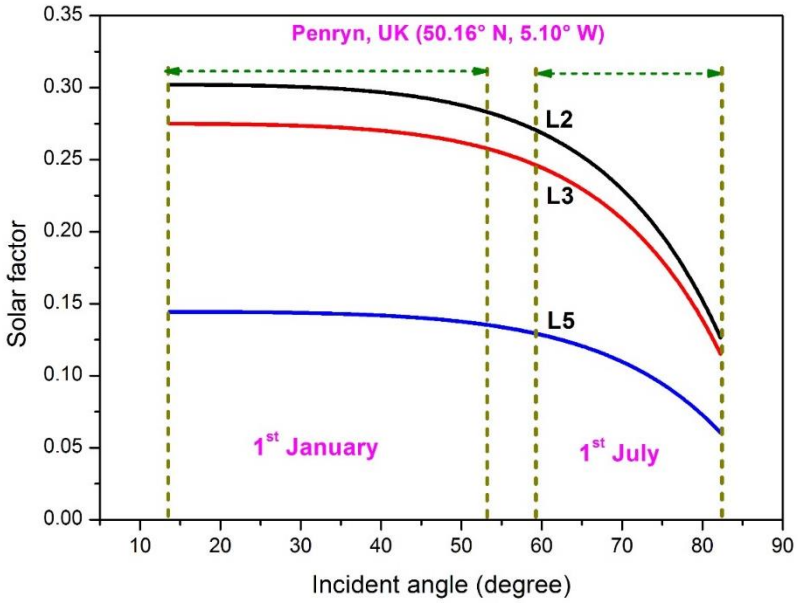

Figure 83. Variation solar factor with solar incident angle

As both conductive glasses are sealed in DSSC, little air gap is present between the two glass panes. So, the whole device was considered as a single glazing (4.4 mm thickness). Using equation 27, angular solar factor was calculated and shown in Figure 83. External heat transfer coefficient (h_e) of 25 W/m^{2}K, internal heat transfer coefficient (h_i) of 7.7 W/m^{2}K, and wind speed of 4 m/s were considered to evaluate the solar factor for the normal incident angle. However, due to the angular transmission, this solar heat gain is not achievable in DSSC glazing [245].

4.8. Glazing transmission and clearness index

Glazing transmittance also has a strong correlation with clearness index, and knowing this value helps in building energy calculation. To evaluate clearness index, the only measured parameter is global horizontal solar radiation. As DSSC is considered to be in wide future as one of the future PV glazing materials, its angular transmission behaviour variation with clearness index evaluation is essential.

The relationship between clearness index and glazing transmittance is given by equation 28 [241]

$$\tau = \tau_0 \left\{ d\left[k_T r_b \left(1-d\right) + \left(1-\cos\theta\right)\left(1-k_T\left(1-d\right)\right)\right] + r_b\left(1-d\right) + \rho_g \frac{\left(1-\cos\beta\right)}{2} \right\} \times \left\{ \frac{\tau_{dir}}{\tau_0} r_b \left(1-d\right)\left(1+k_T d\right) + \frac{\tau_{diff}}{\tau_0}\frac{d}{2}\left(1+\cos\theta\right)\left(1-k_T\left(1-d\right)\right) + \frac{\tau_g}{\tau_0}\frac{\rho_g\left(1-\cos\theta\right)}{2} \right\} \quad (28)$$

From equation 21 $\tau = \tau_{dir}$ when $\theta = \theta_{dir}$

$\tau = \tau_{dif}$ when $\theta = \theta_{dif} = 59.68 - 0.1388\beta + 0.001497\beta^2$ [246]

$\tau = \tau_g$ when $\theta = \theta_g = 90 - 0.5788\beta + 0.002693\beta^2$ [246]

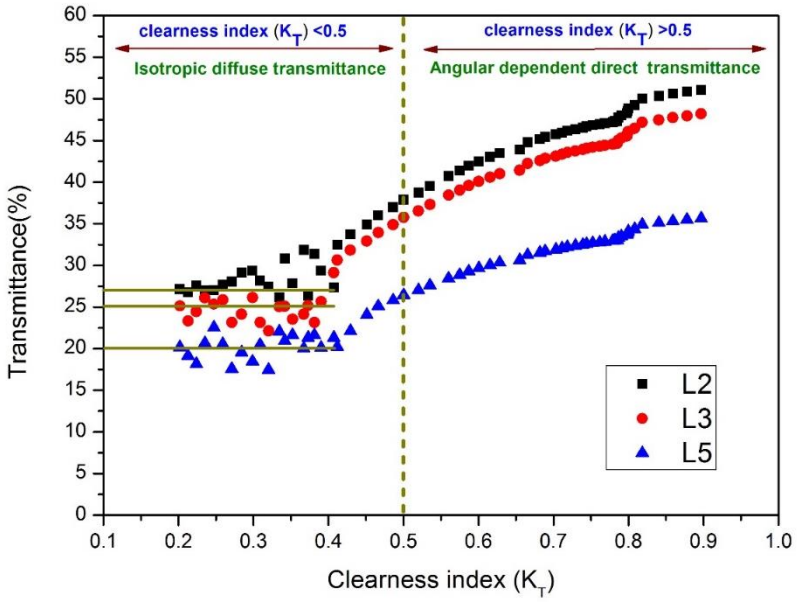

Figure 84. Variation of DSSC transmission with clearness index

The correlation between clearness index and glazing transmittance was evaluated for DSSC glazing and shown in Figure 84. Isotropic diffuse transmittance is dominant for clearness index below 0.5, whereas angular dependent direct transmission is dominant after 0.5. For vertical plane DSSC glazing, transmittance varies with season, day and time. However, for south

facing vertical plane DSSC glazing, single value glazing transmittance of 20% for L5, 25% for L3 and 27% for L2 can be chosen throughout the year while clearness index is less than 0.5. This study offers a yearly usable single glazing transmittance for DSSC glazing, which is advantageous for the building designers in northern latitude areas. For others, azimuthal orientation single achievable glazing transmission below the threshold clearness index is listed in Table 15.

Table 15. Yearly usable single transmittance value of DSSCs for different transparency, different azimuthal and monthly clearness index

Inclination	**Azimuthal orientation**	**Mean monthly clearness index**	**Transmittance**		
			L2 DSSC	**L3 DSSC**	**L5 DSSC**
Vertical plane DSSC	North	0.7	27%	25%	20%
	South	0.5	27%	25%	20%
	East, West, North West, North East	0.6	27%	25%	20%

4.9. Daylight glare analysis

To identify the daylight glare control potential of these DSSC glazings, theoretical analysis using measured outdoor vertical illuminance was employed. Glare index calculation is provided for a DSSC glazing for a typical sunny day, intermittent day and overcast day in Penryn, UK (50.16° N, 5.10° W). The criteria for sunny, intermittent and overcast days are 1. Sunny day- 0-5% opaque cloud coverage,

2. Intermittent day- 26-50% opaque cloud coverage, and 3. Overcast day- 88-100% opaque cloud coverage

The glazing is considered to be on a vertical south façade. The dimensions of the room and glazing position and measuring points are shown in Figure 85. These dimensions resemble the DSSC as a large glazed façade, while the internal surface of the unfurnished room has white paint (0.8 reflectance) as mentioned previously [247]. The glare subjective rating is [248] given by equation 29 where E_V is the vertical illuminance facing the window (worst case) measured at the centre of the room. This SR index allows discomfort glare estimation experienced by subjects when working at a visual daylight task (VDT) placed against a window of high or not uniform luminance. The reason for selecting this index is the engagement of only one photo sensor which can save time and cost. The criterion scale of discomfort glare subjective rating is given in Table 16. This method also allows the non-intrusive measuring equipment necessary for scale model daylighting assessments [249,250].

$$SR = 0.1909E_v^{0.31} \tag{29}$$

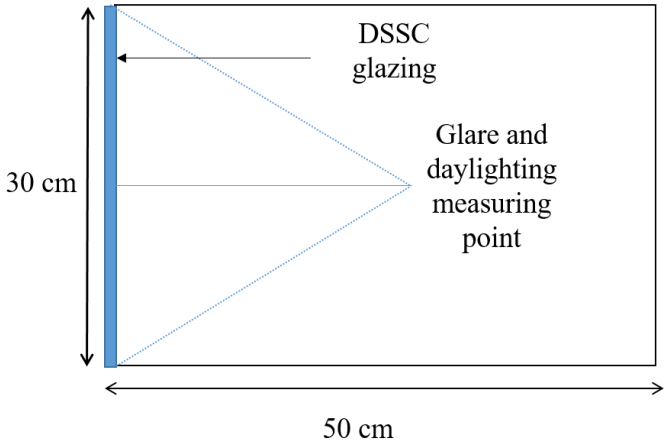

Figure 85. Schematic cross section of a room with DSSC glazing place on vertical south facade.

Table 16. Criterion scale of discomfort glare subjective rating (SR)

Comfort level indicator	Glare subjective rating (SR)
Just intolerable	2.5
Just disturbing	1.5
Just noticeable/ accepting	0.5

Glare analysis was performed using equation 28. Wavelength dependent spectrum data for double glazing was collected from Ghosh et.al. [224]. Illuminance data was recorded for south facing vertical plane on the roof of the ESI building in Penryn, UK (50.16° N, 5.10° W) using the illuminance sensor from MESA. Figure 86, Figure 87 and Figure 88 show the daylight control potential using three different transparent DSSCs and a double glazing for a typical clear sunny day, intermittent cloudy day and overcast day respectively. Around mid-day, all types of glazings allowed an excessive amount of light which creates disturbing glare on a clear sunny day. Despite this, all the glazings allow excessive light which creates disturbing glare, 21% reduction in glare subjective rating is observed for the 37% transparent DSSC glazing compared to double glazing on a clear sunny day. Glare reduction is less in all the DSSC glazings for intermittent cloudy and overcast days as well. The glare subjective rating for a typical sunny, intermittent cloudy and overcast day for different glazing types are compared in Table 17.

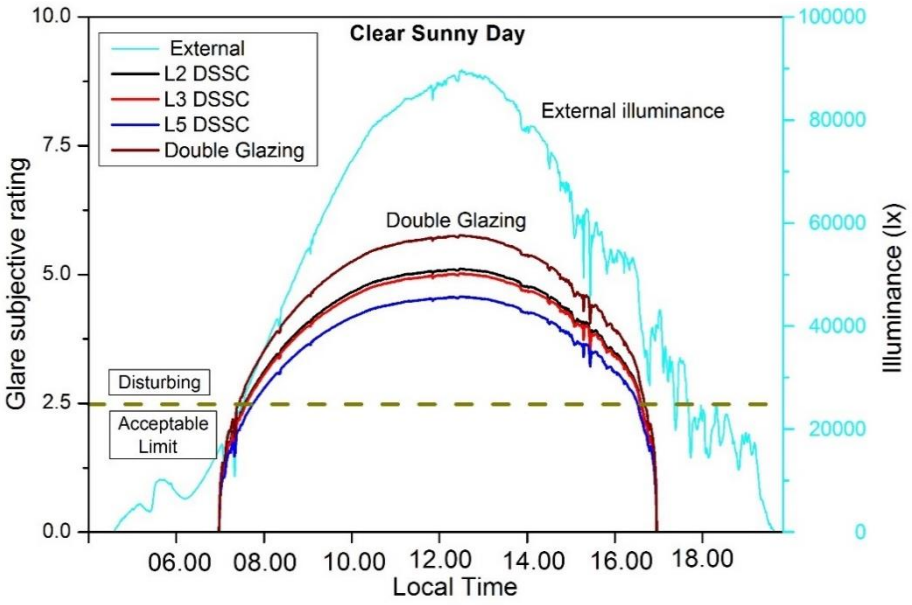

Figure 86. Daylight glare index of transparent DSSC and double glazing for a typical clear sunny day at Penryn, University of Exeter

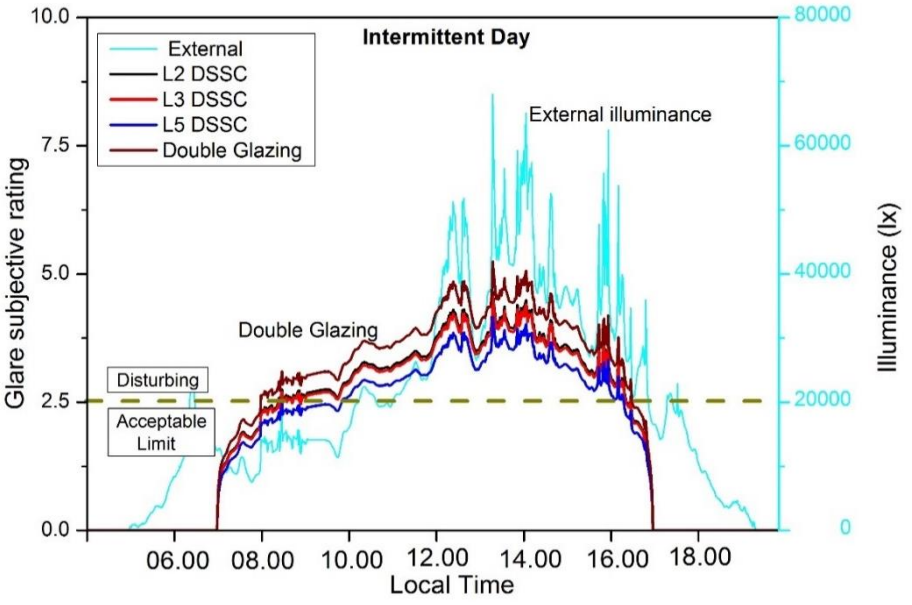

Figure 87. Daylight glare index of transparent DSSC and double glazing for an intermittent day at Penryn, University of Exeter

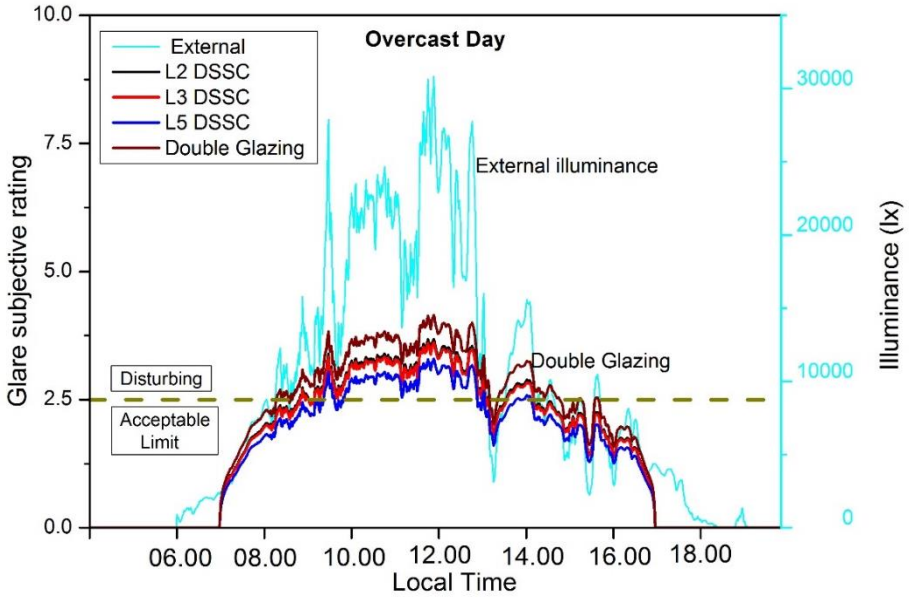

Figure 88. Daylight glare index of transparent DSSC and double glazing for a typical cloudy day at Penryn, University of Exeter

Table 17. Comparison of glare subjective ratings for a typical sunny, intermittent cloudy and overcast day for different glazing types

Weather	Glare subjective rating (SR) @ mid-day			
	Double Glazing	**L2 DSSC**	**L3 DSSC**	**L5 DSSC**
Clear sunny day	5.70	5.10	4.95	4.50
Intermittent cloudy day	4.30	3.75	3.70	3.40
Overcast day	3.80	3.40	3.35	3.10

4.10. Conclusions

The colour rendering index (CRI) and correlated colour temperature (CCT) of transmitted daylight through a DSSC glazing is an essential parameter for

building interior space comfort. In this chapter, different transparent DSSCs were fabricated using different TiO_2 electrode thickness. CCT and CRI for all the DSSC glazings were calculated. It was found that 53% and 50% transparent DSSCs offered achievable CRI and CCT. The results of 53% transparent DSSC were compared with vacuum and double-glazing. Vacuum and double-glazing, which have higher transparency than DSSC, offered only 2.7% higher CRI and CCT values near to overcast sky. Even though 53% transparent DSSC offered best CRI and CCT, 37% transparent device offered the best efficiency. So, the devices higher than 50% transparency (L2, L3) and electrically the most efficient device (L5) were chosen for further analysis. The angular transmission of DSSC glazing for three different transparencies (L2, L3, L5) were investigated and finally the solar factor was calculated. It was found that, for Penryn location (50.16° N, 5.10° W) solar factor was higher in January than July. Using clearness index and glazing transmission correlation, one single yearly usable glazing transmission for different azimuthal direction was evaluated. Finally, daylight glare analysis of DSSC glazing was carried out and compared with double glazing. For a clear sunny day, 21% more glare can be reduced than double glazing using 37% transparent DSSC glazing. Since the effect of device temperature does not have a significant impact on the performance much, long term stable DSSC glazing system could replace the double-glazing in the future.

Chapter 5: Performance of semi- transparent dye-sensitised solar cells under concentrated light

After analysing the results in the previous chapter, it has been found that semi- transparent dye-sensitised solar cells (DSSCs) can be coupled within a building's architecture to provide daylighting and electrical power simultaneously. However, the performance loss in large area DSSCs has been a long-term issue. In this chapter, the relationship between the transparency and performance of DSSCs is studied by changing the TiO_2 electrode thickness. A Low concentrator with 3× optical concentration was designed and employed to study the effect of light concentration on DSSCs. Moreover, a systematic study of the temperature dependency on the performance of bare DSSCs and those coupled with LCPV system has been carried out. In addition to that, both bare and concentrator coupled DSSCs have been tested under different light intensities.

This chapter is based on the following published articles

1. **P. Selvaraj**, H. Baig, T.K. Mallick, J. Siviter, A. Montecucco, W. Li, M. Paul, T. Sweet, M. Gao, A.R. Knox, S. Sundaram, *Sol. Energy Mater. Sol. Cells* **2018**, *175*, 29.
2. **P. Selvaraj**, H. Baig, T.K. Mallick, S. Sundaram, *Mater. Lett.* **2018**, *222*, 78.

5. 1. Introduction

Even though DSSCs have achieved PCEs over 14% [251,252] with a small active area, the power output decreases with an increase in the cell active area of the photoanode [253]. This is due to some unfavourable issues such as non-homogeneous and non-uniform titania layers because of large area deposition, dye sensitisation and electrolyte filling issues and electrical interconnection of

individual cells [125]. However, the performance loss during scale up can be addressed by coupling optical concentrators with small DSSC. Concentrating Photovoltaic (CPV) systems make use of optical components which concentrate the incoming sunlight and focus it on solar cells. The concentrated light reaching the solar cell increases the energy production several times [129,254,255]. As mentioned earlier, based on the light illumination intensity it focuses on the solar cell, the concentrators may be classified as low concentration systems, medium concentration systems and high concentrator systems. Low concentration systems are usually simple in their design, manufacture and operation. These systems have a concentration factor of less than 10× [65]. Due to its versatility in applications and geometries, a type of low concentrator - the compound parabolic concentrator (CPC) is used in low and medium temperature ranges [256]. Since DSSC performance is very sensitive to its operating temperature, A low concentrator with 3× optical concentration is used in this work.

5. 2. Experimental Methods

5.2.1. DSSC Fabrication

Fabrication methods of the working electrodes and the corresponding devices are given in the chapter 2.

5.2. 2. Low Concentrator fabrication

Figure 89. shows the fabrication of the concentrator with a geometrical concentration factor of C=4×. The concentrator was printed into two halves (Figure 89. (a)), reflective film (94%) was adhered on the CPC surface (Figure 89. (b)), and the two halves were assembled together as shown in (Figure 89. (c)). The concentrator was placed on top of the solar cell for testing. (Figure 89. (d))

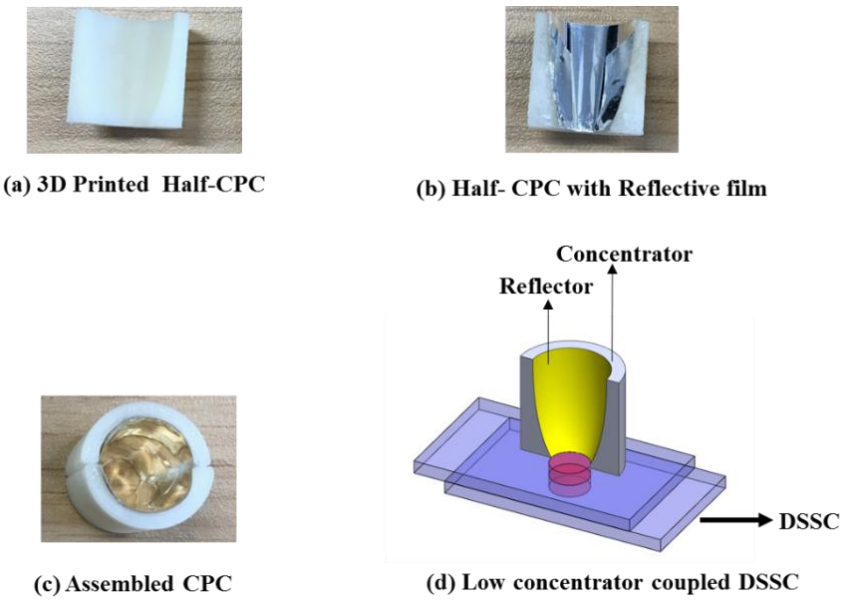

Figure 89. Fabricated low concentrator. (a) one half of the printed concentrator, (b) adhered reflective film, (c) assembled concentrator used for this work and, (d) low concentrator coupled DSSC

5.2.3. Device characterization

In an indoor controlled environment, the CPV unit was tested to evaluate the impact of radiation intensity. Under the same condition, the DSSCs were characterised as mentioned in the chapter 2. The temperature of the devices was recorded using an OMEGA RDXL 12SD temperature recorder. Finally, the concentrator unit was placed on the DSSC to perform DSSC-LCPV measurements.

5.3. Photovoltaic performance of the devices

5.3.1. PV performance of the bare DSSCs

As discussed in the previous chapter, when the thickness of the electrode increases, the transmittance of the solar cell gradually decreases. Meanwhile, when the TiO_2 layer thickness was increased from 3.5µm to 10 µm an obvious increase of J_{sc} from 7.36 mA/cm^2 to 12.75 mA/cm^2 was occurred in the

corresponding devices, resulting in a corresponding improvement of efficiency from 2.51% to 5.93%. The current density-voltage (J-V) curves of the devices are shown in Figure 90.

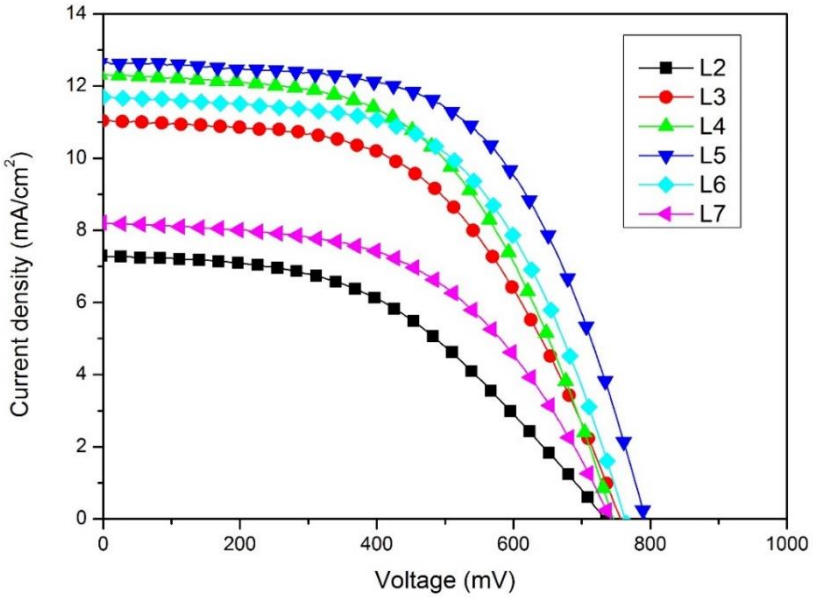

Figure 90. Photocurrent density-voltage (J-V) curves of the bare DSSCs based on different TiO_2 thicknesses.

Generally, more dye molecules attached to the thick TiO_2 films absorb more light, leading to low transmittance, also thick films physically block/absorb the light [232]. Conversely, the photovoltaic performance decreased after 10 µm thick TiO_2 with further increase in titania layer thickness (12µm, 14 µm) [257–259]. In common, increasing the thickness of TiO_2 layer can enhance the light harvesting and improve the device performance in DSSC, but which does not agree with J-V test results for devices L6 and L7. For that reason, too thick TiO_2 layers increase the length of the electron pathways, and thus decrease FF and V_{oc} and, in extreme cases, even I_{sc}.[260] .The photovoltaic parameters of the devices with different TiO_2 thickness are given in Table 18.

Table 18. Photovoltaic parameters of the bare cells based on different TiO_2

thicknesses under an illumination of 1000 W/m^2 (AM 1.5 G).

Device	TiO_2 thickness (μm)	J_{sc} [mA/cm^2]	V_{oc} [mV]	FF [%]	P_{max} [mW/cm^2]	η [%]
L2	3.5	7.36	733	46.6	2.48	2.51
L3	6.0	11.14	756	54.0	4.46	4.49
L4	8.0	12.42	746	56.2	4.99	5.02
L5	10.0	12.75	793	58.7	5.87	5.93
L6	12.0	11.81	763	59.0	5.10	5.15
L7	14.0	8.28	742	56.6	3.22	3.24

5.3.2. Performance loss in scaled-up DSSCs

In order to use DSSCs as building integrated photovoltaic element, the devices need to be prepared as transparent as possible especially for window applications. Due to this, scaling up of DSSC has become an important process even though it has associated with different issues. Here, 1.1 cm^2 active area DSSC device with 10 μm titania thickness and 37% transparency was fabricated under the same conditions to study the performance of a 4× scale-up device (Figure 91).

(a) Fabricated Bare DSSC (b) Scaled up DSSC

Figure 91. Fabricated L5 devices. (a) Small active area bare DSSC and (b) Scaled-up device.

Figure 92. (a, b) shows the current density -voltage and power density -voltage behaviour respectively for device with an active area of 0.28 cm^2 and 1.1 cm^2 (~4 times larger area than 0.28 cm^2). The output power P of a solar cell is given by current times voltage (P=I.V). At a given IV point, P can be visualised by drawing a square, its area is equal to the output power at that point. Figure 92 (b) provides the power output of the both DSSC devices per unit cross-sectional area whereas, current density figures shows the amount of electric current flowing per unit cross-sectional area of both the devices. The short circuit current of 1.1 cm^2 active area device is higher than the small area device (Table 19). However, the current density and power density of the scaled up DSSC is much lower than the small area devices. Due to the high sheet resistance, which causes Ohmic loss and further leads to a significantly reduced fill-factor and efficiency of the scaled-up devices[261].

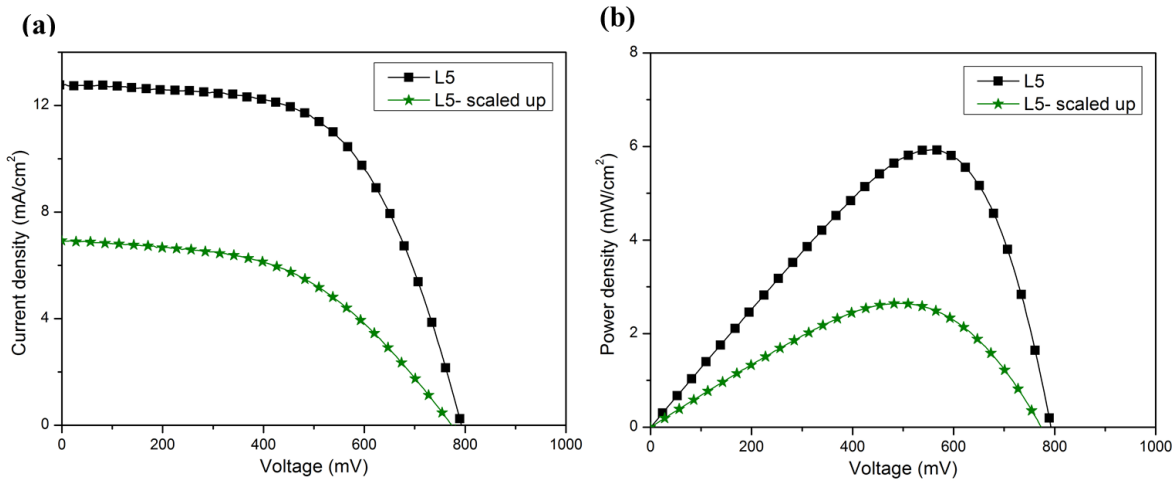

Figure 92. Comparison of (a) current density-voltage curves, and (b) power density-voltage of the small area bare cells, coupled with LCPV and scaled up device.

Table 19. Photocurrent density - voltage (J-V) parameters of the bare cells and scaled up device under an illumination of 1000 W/m^2 (AM 1.5 G).

Device	I_{sc} [mA]	J_{sc} [mA/cm^2]	V_{oc} [mV]	FF [%]	P_{max} [mW/ cm^2]	η [%]
L5- 0.28cm^2	3.60	12.75	793	58.7	5.87	5.93
L5- 1.1 cm^2	7.76	6.93	773	49.3	2.96	2.64

5.3.3. PV performance of the low concentrator coupled DSSCs

The LCPV system was placed on DSSCs to understand the photovoltaic performance of DSSCs under concentrated light. Figure 93 and Table 20 show the photocurrent density-voltage characteristics and the photovoltaic parameters of the DSSCs coupled with the low concentrator system. It is clear from the Table 20 that J_{sc} of the devices coupled with the concentrator increased with the TiO_2 electrode thickness then starts decreasing after 10 µm which is due to long electron diffusion length. Device L5C has the highest J_{sc} of 23.16 mA/cm^2, which is 82% higher than the corresponding bare device. Increase in the short circuit current is due to the concentrated light. Like silicon solar cells, open circuit voltage of DSSC increases logarithmically with light intensity according to the equation below,

$$V'_{oc} = V_{oc} + \frac{nkT}{q} \ln X \qquad (30)$$

where X is the concentration of sunlight [262].

Although fill factor decreased for all the devices compared with the bare cells, which could be due to more electron recombination, but the overall photovoltaic performance increased for all the devices coupled with the low concentrator.

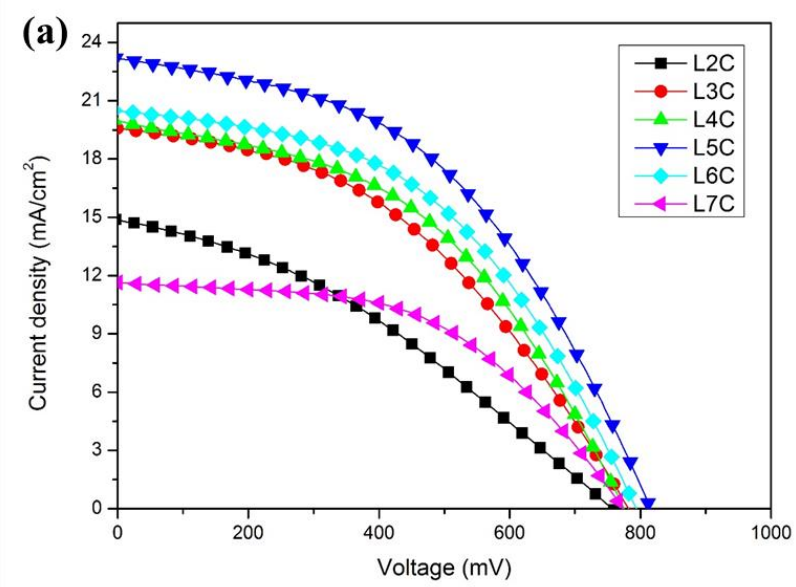

Figure 93. Photocurrent density-voltage (J-V) curves for the low concentrator coupled devices based on different TiO_2 thicknesses.

Table 20. Photovoltaic parameters of the cells based on different TiO_2 thicknesses with low concentrator under an illumination of 1000 W/m^2 (AM 1.5 G).

Device	**J_{sc} [mA/cm^2]**	**V_{oc} [mV]**	**FF [%]**	**P_{max} [mW/cm^2]**	**η [%]**
L2C	14.86	757	34.4	3.89	3.90
L3C	19.55	782	42.7	6.55	6.60
L4C	19.96	775	45.6	7.08	7.12
L5C	23.16	816	46.2	8.74	8.82
L6C	20.48	794	47.3	7.68	7.77
L7C	11.63	774	53.5	4.63	4.69

The photovoltaic performances of bare and concentrator coupled DSSCs with respect to TiO_2 film thickness are compared in Figure 94.(a-d). It is clear that

the concentrator coupled devices perform better than their bare counterparts. From the comparison, device L5 with 10 µm TiO_2 thickness is found to be the best of all devices with 5.9% and 8.8% PCE for bare and concentrator coupled.

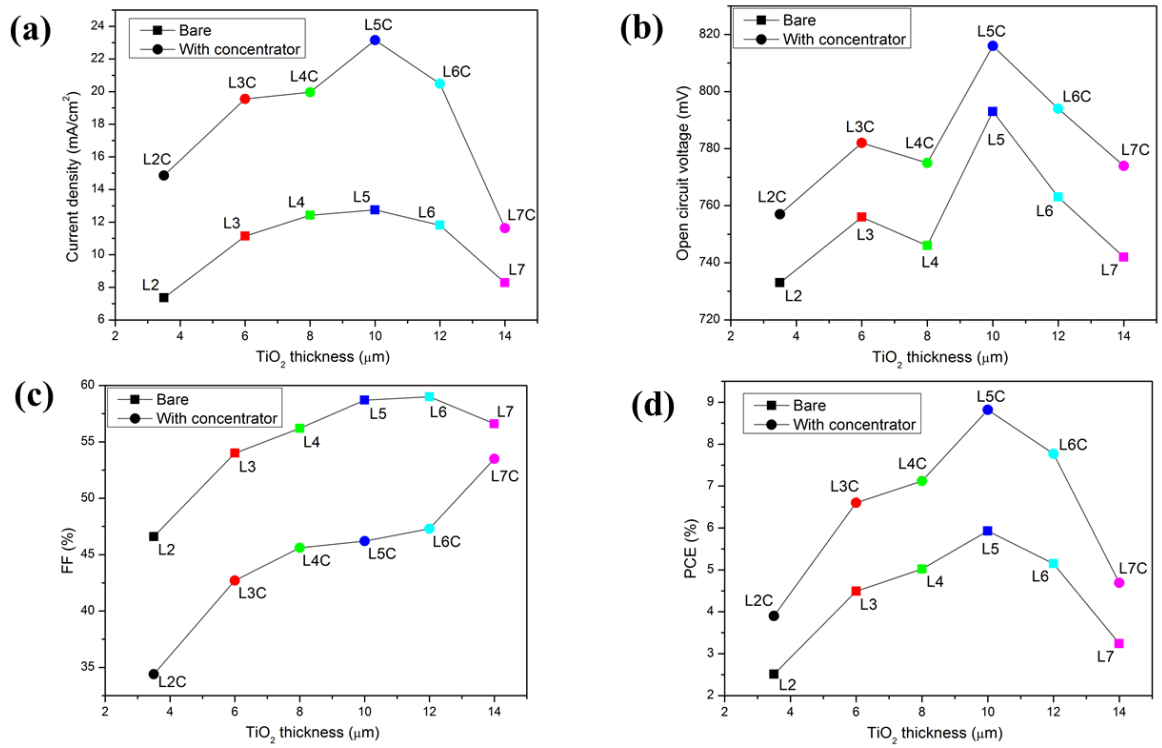

Figure 94. Comparison of performance parameters with different working electrode thickness for bare and low concentrator coupled devices.

5.3.4. L5 scaled up Device vs L5 low concentrator Coupled Device

Figure 95 and Table 21 compare the detailed current- voltage behaviour for device L5 with an active area of 0.28cm^2 bare device (L5), 0.28cm^2 device coupled with LCPV system and scaled up 1.1 cm^2 device. The digital images of the fabricated devices are presented in Figure 96. From the comparison between the L5 scaled-up device and low concentrator coupled one, the concentrator coupled device has slightly lesser current value due to the losses in reflective film. The short circuit current of 1.1cm^2 active area device is higher than the other devices. On the other hand, the current density of the concentrator coupled

device is much higher than the scaled-up device which increases the overall performance. From the above comparison L5 has been found as the best performing device. Therefore, device L5 has been taken for further analysis.

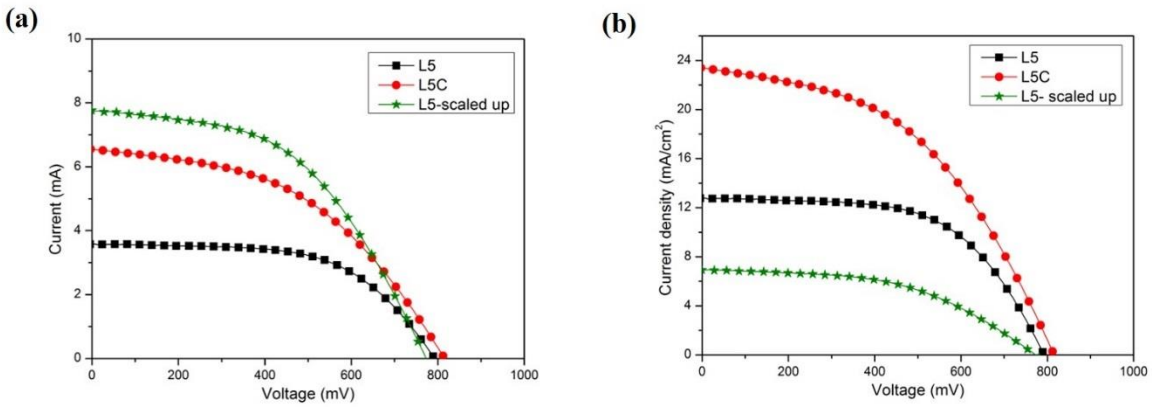

Figure 95. Comparison of (a) I-V, and (b) J-V curves of the small area bare cells, coupled with LCPV and scaled up device under 1 sun illumination.

Table 21. Comparison of the photovoltaic parameters of the small active area bare cells, small cells coupled with LCPV and scaled up device under an illumination of 1000 W/m^2 (AM 1.5 G).

Device	**I_{sc} [mA]**	**J_{sc} [mA/cm^2]**	**V_{oc} [mV]**	**FF [%]**	**P_{max} [mW/ cm^2]**	**η [%]**
L5- 0.28cm^2	3.60	12.75	792.7	58.7	5.87	5.93
L5C- 0.28cm^2	6.54	23.16	816.2	46.2	8.74	8.82
L5 1.1 cm^2	7.76	6.93	773.4	49.3	2.64	2.64

(a) Fabricated Bare DSSC (b) DSSC with Concentrator (c) Scaled up DSSC

Figure 96. Digital images of the fabricated devices

5.3.5. Performance of low concentrator coupled silicon solar cell

To find the concentrator intensity output, a 0.28 cm^2 silicon solar cell was coupled with the same low concentrator and its performance compared with the bare silicon solar cell (Figure 97, Figure 98 and Table 22). There is a significant increase in all the photovoltaic parameters. On the contrary to DSSC performance, an increase of 7.7% fill factor is observed for the low concentrator coupled silicon solar cell. By comparing the current densities, it was found that the LCPV system coupled silicon solar cell showed an optical concentration of 3.05x.

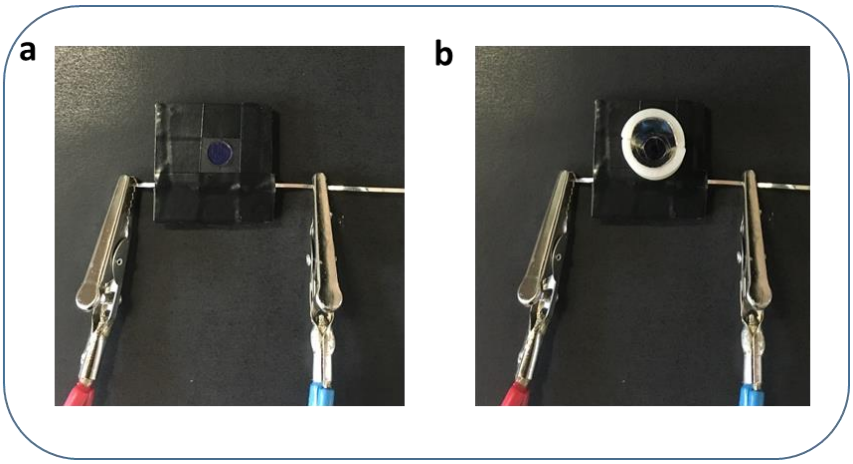

Figure 97. Devices used for Silicon solar cell measurements (a). Bare 0.28cm^2 Si solar cell (b). Si solar cell coupled with low concentrator.

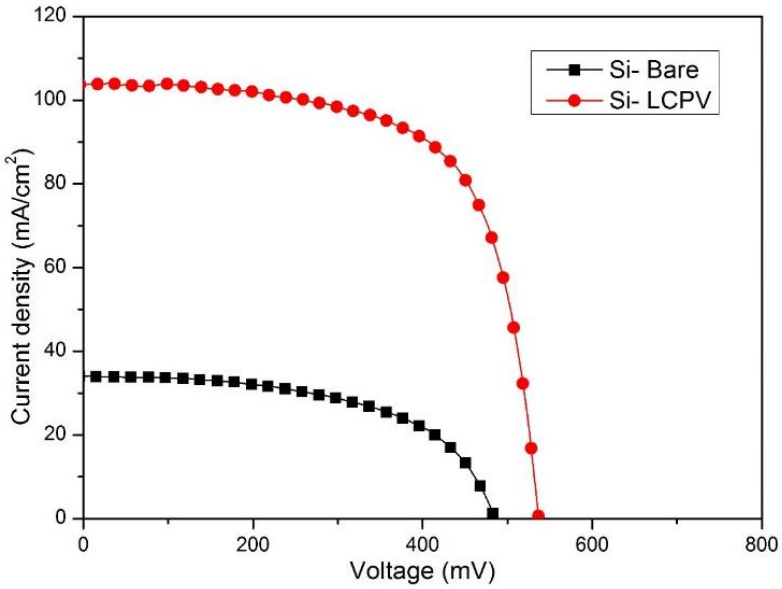

Figure 98. Comparison of J-V characteristics of Bare 0.28cm^2 Si solar cell and Si solar cell coupled with low concentrator.

Table 22. Photovoltaic parameters of Bare 0.28cm^2 Si solar cell and Si solar cell coupled with low concentrator under 1 sun illumination.

Device	J_{sc} [mA/cm^2]	V_{oc} [mV]	FF [%]	P_{max} [mW/ cm^2]	PCE [%]
Si-Bare	33.97	485.3	58.7	9.67	9.1
Si-LCPV	103.75	536.7	66.4	36.92	36.98

5.3.6. Impact of operating temperature on PV performance

DSSC performance is very sensitive to its operating temperature as the concentrated sunlight generates high temperature due to high light intensity [263]. To understand the stability and behaviour of transparent DSSCs at different operating temperatures, the best performing device (L5) was tested with and without LCPV under 1 sun illumination for 20 minutes. The photovoltaic parameters of the devices are given in Table 23.

Table 23. Impact of operating temperature on the photocurrent density - voltage (J-V) parameters of the bare cell (L5) under an illumination of 1000 W/m^2 (AM 1.5 G).

Temperature [°C]	**J_{sc} [mA/cm^2]**	**V_{oc} [mV]**	**FF [%]**	**P_{max} [mW/ cm^2]**	**η [%]**
28	12.75	792.7	58.7	5.87	5.93
32	12.89	795.7	58.7	5.96	6.02
36	13.01	785.3	59.2	5.99	6.05
40	13.06	777.3	59.4	5.96	6.02
42	13.09	770.9	59.5	5.94	6.00
44	13.11	767.5	59.6	5.93	5.99
46	13.12	766.5	59.7	5.92	5.98
48	13.12	765.2	59.5	5.92	5.97
50	13.09	763.4	59.6	5.91	5.97
52	13.08	762.9	59.7	5.91	5.97

Table 24. Impact of operating temperature on the photocurrent density - voltage (J-V) parameters of the device coupled with LCPV (L5C) under an illumination of 1000 W/m^2 (AM 1.5 G).

Temperature [°C]	**J_{sc} [mA/cm^2]**	**V_{oc} [mV]**	**FF [%]**	**P_{max} [mW/ cm^2]**	**η [%]**
28	23.16	816.2	46.2	8.74	8.82
32	25.16	821.3	46.0	9.41	9.51
36	25.35	814.7	48.5	10.01	10.11
40	25.55	808.1	49.2	9.99	10.09

42	23.95	799.7	48.9	9.45	9.54
44	23.91	796.7	49.9	9.40	9.50
46	23.86	793.0	50.4	9.27	9.36
48	21.70	785.3	50.7	8.65	8.66
50	21.66	782.8	51.0	8.58	8.64
52	21.60	779.5	51.4	8.57	8.63

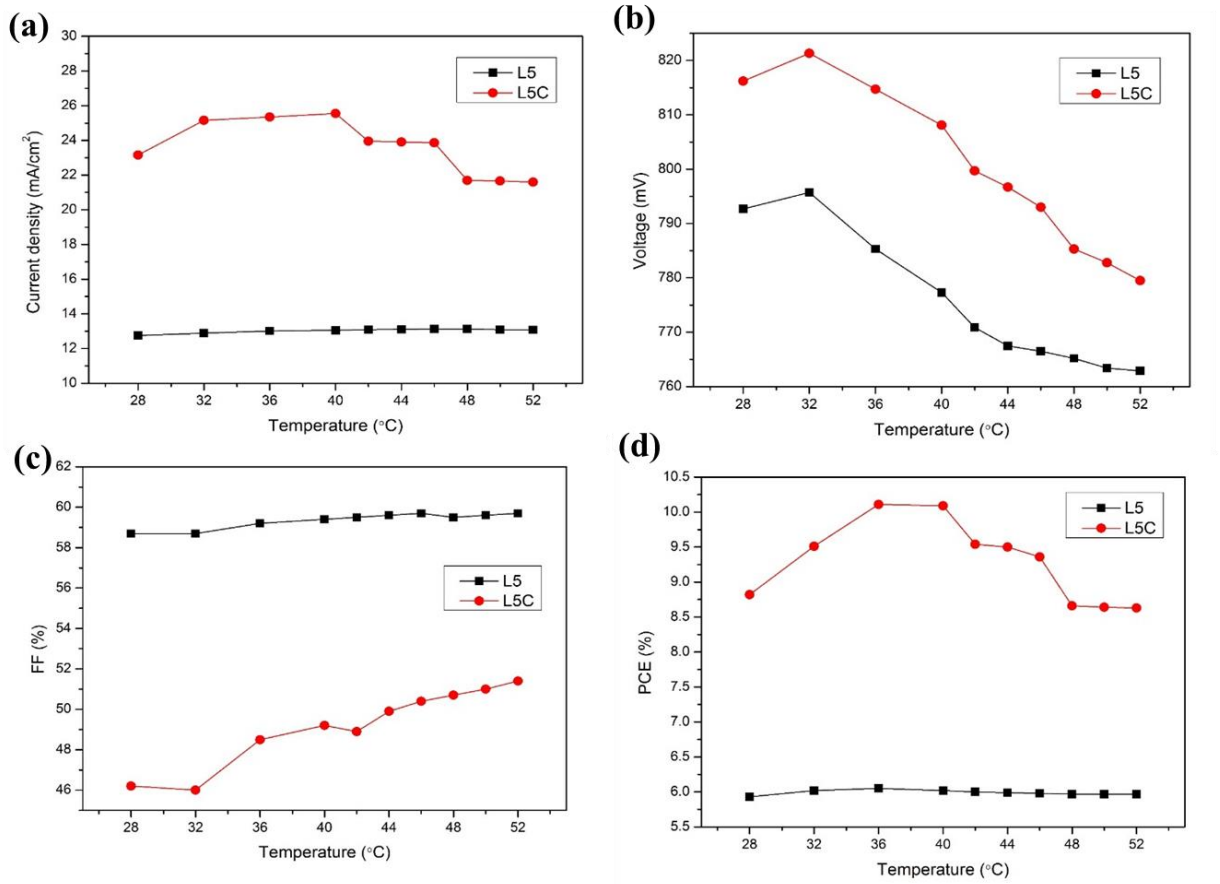

Figure 99. Temperature dependence of the DSSC parameters of bare cell (L5) and coupled with LCPV (L5C) measured under an illumination of 1000 W/m^2 (AM 1.5 G). (a) Temperature (°C) vs Current density (mA/cm^2), (b) Temperature (°C) vs Open circuit voltage (mV), (c) Temperature (°C) vs Fill factor, (d) Temperature (°C) vs power conversion efficiency.

It can be seen from Figure 99. (a) that current density (J_{sc}) for the bare device increases gradually up to 42°C and then starts decreasing. For the device

coupled with LCPV, J_{sc} increases till 40°C and then falls, whereas, V_{oc} increases at the start then steadily decreases with temperature for both devices (Figure 99. (b)). On the other hand, power density reaches its maximum value at 36°C then starts decreasing from 5.99 mW/cm^2 to 5.91 mW/cm^2 for bare devices and from 10.01 mW/cm^2 to 8.57 mW/cm^2 for low concentrator coupled devices. The maximum power conversion efficiency is recorded at 36°C (Figure 99. (d)) for both the devices. It was found that the devices reached a steady state temperature of 52°C after 20 minutes. Both devices show positive and negative temperature co-efficient as the power conversion efficiency of both the devices increasing till 36°C then start decreasing. Due to high light intensity, the LCPV coupled devices obtained higher current density than the bare devices. Thus, the overall performance of the solar cells increases even at high temperatures. This oscillatory behaviour of the opto-electronic properties may be attributed due to the different velocities of the redox processes occurring at the TiO_2/dye, dye/electrolyte and the electrolyte/counter electrode interfaces of the DSSCs [264,265].

5.4. Charge transfer mechanics in semi-transparent DSSCs under low concentration

As DSSC systems have many interfaces such as TiO_2/dye, dye/electrolyte and electrolyte/counter electrode, incoming light intensity could influence the electronic properties of the devices. When a solar concentrator is coupled, the intensity of incoming light becomes higher. Figure 100 illustrates the different charge transport processes of the DSSC systems used in this work. In bare small area DSSC the electron generation is less due to the less intensity of light. When a concentrator is coupled, more electrons are generated which can be seen from figure b. Even though the scaled-up device generates and transports more

electrons, the active area is four times larger than the small device. The electron transport of the concentrator coupled device is similar to the scaled-up device with 4x lesser active area.

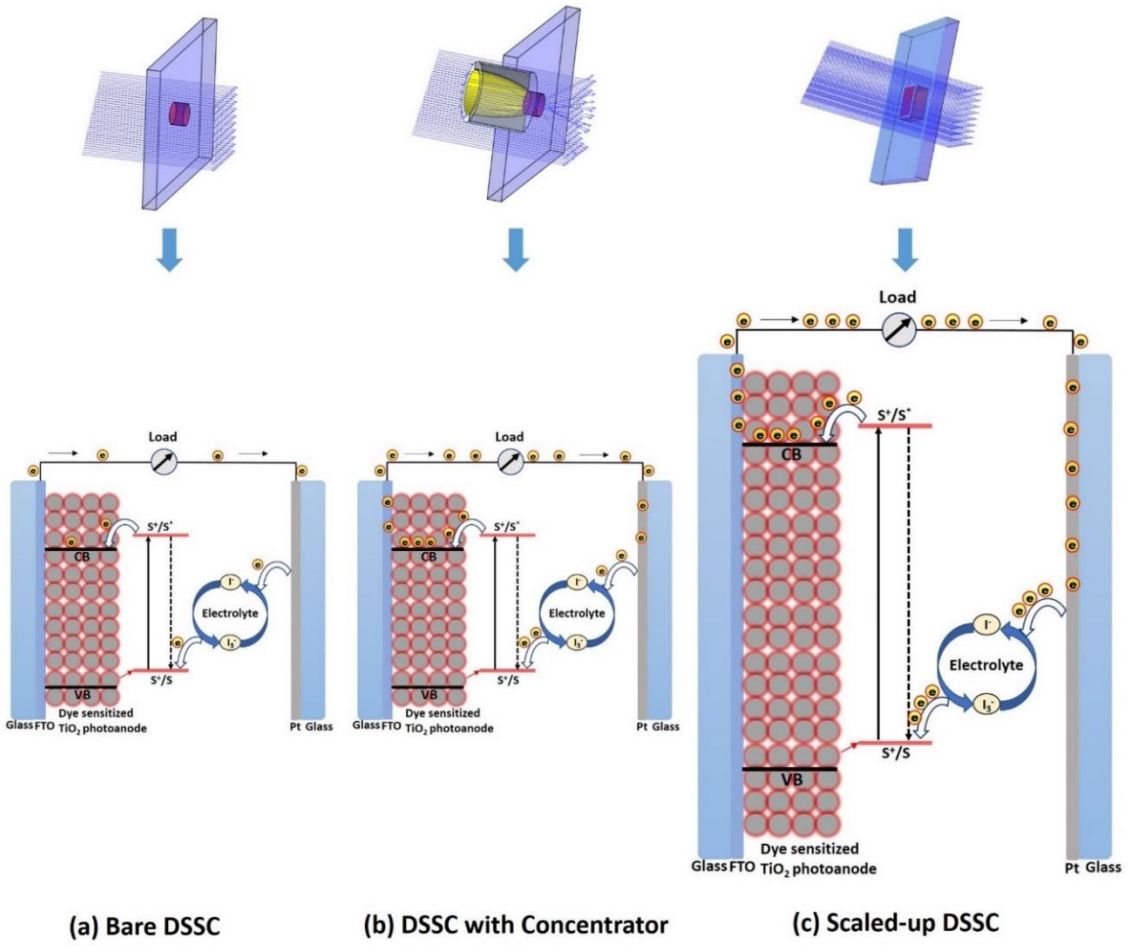

Figure 100. Schematic illustration of the charge transfer process in (a) 37% transparent bare DSSC with small active area (b) 37% transparent DSSC coupled with low concentrator and (c) 37% transparent scaled-up DSSC.

To understand the electronic and ionic process, electrochemical impedance spectroscopy was performed for DSSCs. EIS is a steady state method which uses a tiny AC voltage to create a very small perturbation on the system. It measures the current response to the application of voltage as a function of the frequency [266]. A lot of research has been done on the EIS

analysis of the DSSC [189,267,268]. However, effect of concentrated light on the charge transport properties of transparent DSSCs has not been focused much. This section focuses on the EIS analysis of the transparent DSSCs and their concentrator coupled devices. EIS measurements were carried out with an Autolab PGSTAT 10 and Z view software was used for data fitting as mentioned in Chapter 2.

5.4.1. Bare DSSCs under dark

Figure 101 shows the impedance spectra of the measured bare devices under dark and with applied bias (V_{oc}). The first semi-circle represents the charge transport at the platinum counter electrode/ electrolyte interface and the second semicircle associated with the mid frequency region, corresponds to the charge transfer and recombination at the TiO_2/dye/electrolyte interface. Generally, a larger diameter corresponds to the larger interfacial resistance and higher interfacial charge recombination. [190]

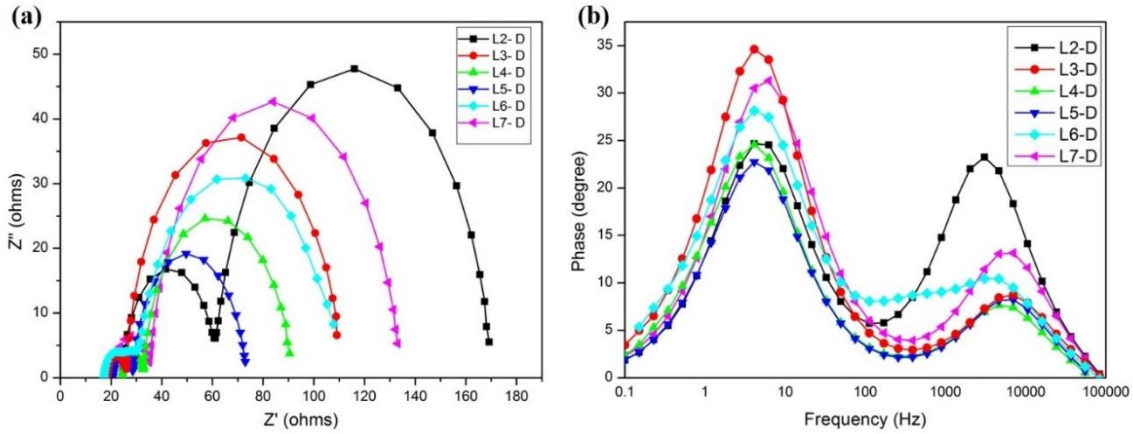

Figure 101. (a) Nyquist and (b) Bode plots of the bare transparent DSSCs under dark condition in open circuit voltage. Experimental data are shown in the symbols, and the equivalent circuit fits are shown in the lines.

Comparison of the semicircles indicates that the semicircle diameter decreases in the order: L2>L3>L4>L5, implying the reduction of charge transfer resistance at the TiO_2/dye/electrolyte interface with an increase in the TiO_2 electrode thickness. Since L5 device has the optimum thickness for electron diffusion towards the FTO, electron recombination is minimized. This results in higher photocurrent for the device L5. However, with further increase in the TiO_2 layer thickness, interfacial charge transfer resistance increases, [269] hence L7, L6> L5. Device L6 has slightly higher charge transport resistance than L7 at the TiO_2/dye/electrolyte, which could be due to the different velocities of the redox processes.

5.4.2. Bare devices under 1 sun light intensity

The diameter of the semicircle decreases when light is illuminated on the solar cells as shown in Figure 102, which suggests the reduction of resistance in the interface. For all the devices, overall charge transfer resistance decreases significantly and the resistance at the TiO_2/dye/electrolyte interface also decreases during the light illumination, which could be due to high electron generation. Interfacial resistance decreases with an increase in titania layer thickness, which influences in high photocurrent.

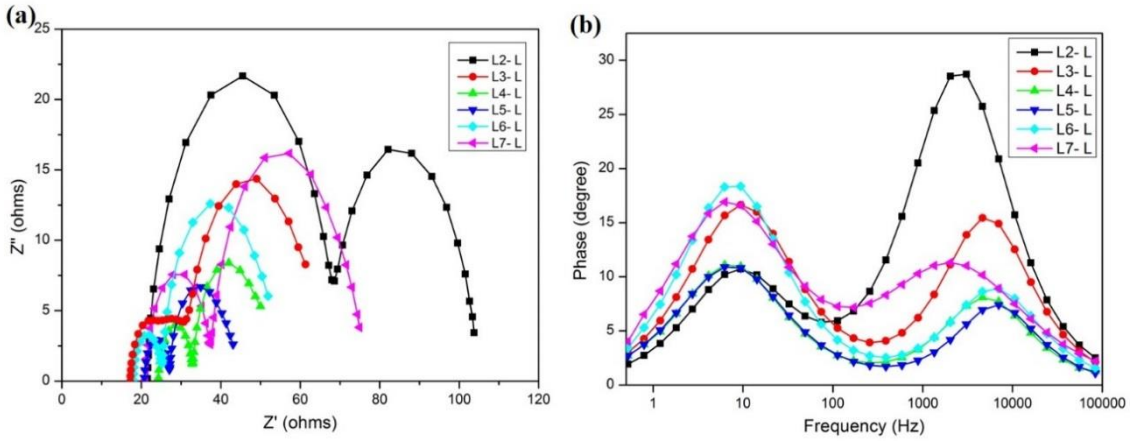

Figure 102. (a) Nyquist and (b) Bode plots of the bare transparent DSSCs under 1 sun illumination in open circuit voltage

The best performing device L5 has an overall charge transfer resistance of 51.83 Ω in dark and 22.50Ω in light measuring conditions. Due to low interface resistances, the PV performance of L5 devices is better than other transparent devices.

5.4.3. Concentrator coupled DSSCs

When the low concentrator is coupled, the charge transfer resistance at TiO_2/dye/electrolyte interface decreases further, which is due to 3× concentrated light. Even though generated photo current is doubled, decrease in charge transfer resistance at the interfaces is not much for low concentrator coupled devices. This could be because of more electron generation causes more electron recombination.

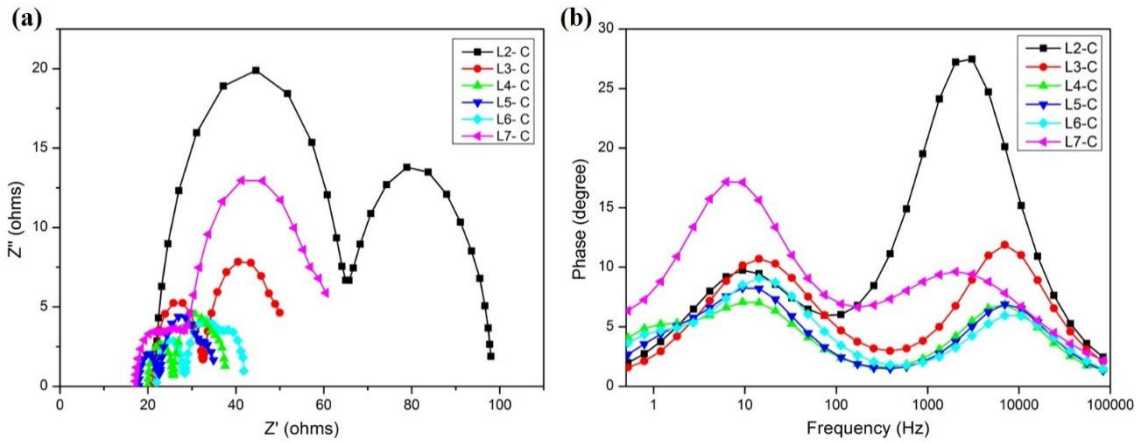

Figure 103. (a) Nyquist and (b) Bode plots of the low concentrator coupled transparent DSSCs under 1 sun illumination in open circuit voltage

In contrast to the bare devices, the charge transport resistance for the thickest electrode device (L7) is higher than L3 device, this occurs due to the high dye loading in the thickest electrode which causes more electron generation due to concentrated light, but the long electron pathway makes it difficult for the electrons to reach the FTO before recombining with the redox electrolyte. This may result in a smaller photocurrent which agrees with the photovoltaic data. Nyquist plots and EIS parameters of the devices are given in Figure 103 and Table 25.

Table 25. Comparison of charge transport parameters of the transparent DSSCs under dark, 1 sun light and low concentrated light.

Device	Charge transport properties										
	Bare DSSC- Dark			Bare DSSC- 1 sun				Low concentrator coupled DSSC			
	R_s (Ω)	R_{ct} (Total) (Ω)	R_{ct} (TiO_2/dye/electrolyte) (Ω)	R_s (Ω)	R_{ct} (Total) (Ω)	R_{ct} (TiO_2/dye/electrolyte) (Ω)	η [%]	R_s (Ω)	R_{ct} (Total) (Ω)	R_{ct} (TiO_2/dye/electrolyte) (Ω)	η [%]
L2	24.89	144.09	108.03	21.78	82.12	35.57	2.51	21.68	76.44	32.77	3.90
L3	24.25	108.87	98.15	21.03	53.79	37.51	4.49	21.25	28.78	17.51	6.60
L4	22.13	68.36	57.95	24.25	25.70	17.22	5.02	22.25	19.56	13.49	7.12
L5	21.09	51.83	44.23	20.67	22.50	16.02	5.93	20.11	17.58	11.83	8.82
L6	19.17	87.18	83.22	17.96	34.09	26.82	5.15	17.92	17.02	12.49	7.77
L7	17.45	90.98	81.70	17.29	44.08	30.09	3.24	17.25	43.48	32.10	4.69

5.4.4. Scaled-up device- Comparison with concentrator coupled device

Nyquist and Bode plots (Figure 104) show that the contact resistance (R_S) of the scaled-up device is higher than the small active area devices. On the other hand, the overall charge transfer resistance is significantly lower for the large area device, which could be due to more electron generation. More dye molecules in the active area helps the scaled- up device to generate more electrons which is evident from its photocurrent value. Charge transfer resistance at

TiO_2/dye/electrolyte interface decreases from 16.02Ω to 11.83Ω for small area device when it is coupled with a low concentrator. For the scaled-up device this resistance is much lower which is 6.92Ω. Even though the interfacial resistance is minimum, yet the overall efficiency is 2.64% for the scaled-up device as seen in the previous section.

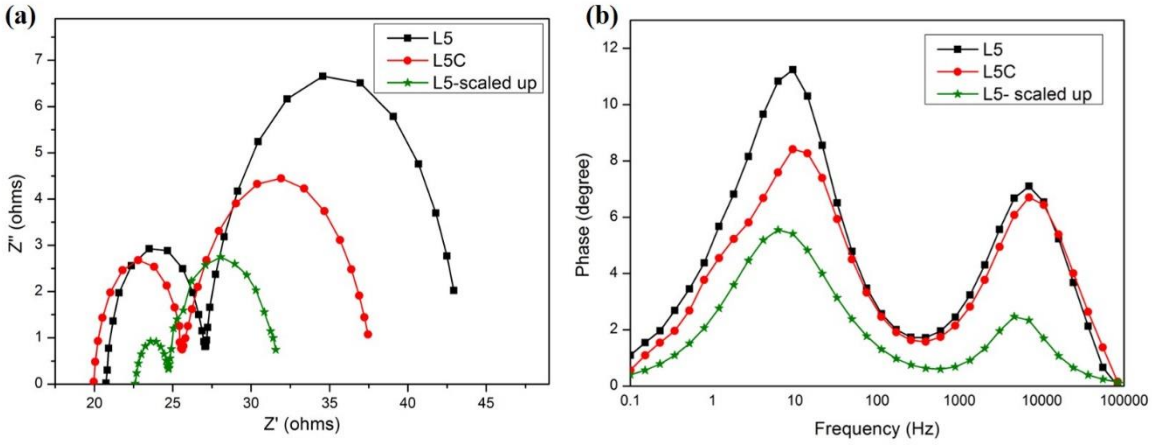

Figure 104. Comparison of (a) Nyquist and (b) Bode plots of the different L5 transparent DSSCs

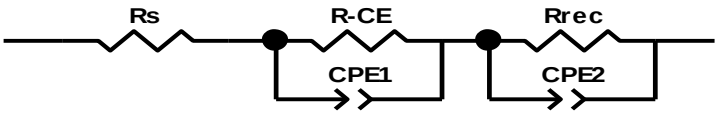

Figure 105. Equivalent circuit used in Z view for fitting all the EIS data.

Where,

R_s is the sheet resistance of the TiO_2 electrode

R-CE is the resistance at the electrolyte/counter electrode interface

Rrec is the resistance at the TiO_2/dye, dye/electrolyte interface

CPE1 and CPE 2 are constant phase elements

5.5. Performance of low concentrated transparent DSSCs under different light intensities

It has been already proved that, the incoming light intensity affects the photovoltaic performance of DSSCs significantly. As DSSCs photovoltaic performance is better than silicon solar cells under low light intensities, it is important to understand the effects of incoming light intensity in order to maintain the optimum operating conditions for the concentrator coupled DSSCs in practical application environments [270]. In this experiment, I systematically investigated the conditions for satisfactory photovoltaic performance of DSSCs in various light-intensity environments. A transparent DSSC with a conversion efficiency of 5.41 (under 1 sun light condition) was fabricated for this study. Light intensity was controlled by EKO MP-160i I–V Tracer software. The devices were tested from 1000 W/m^2 to 400 W/m^2 light intensities.

5.5.1. Bare DSSCs

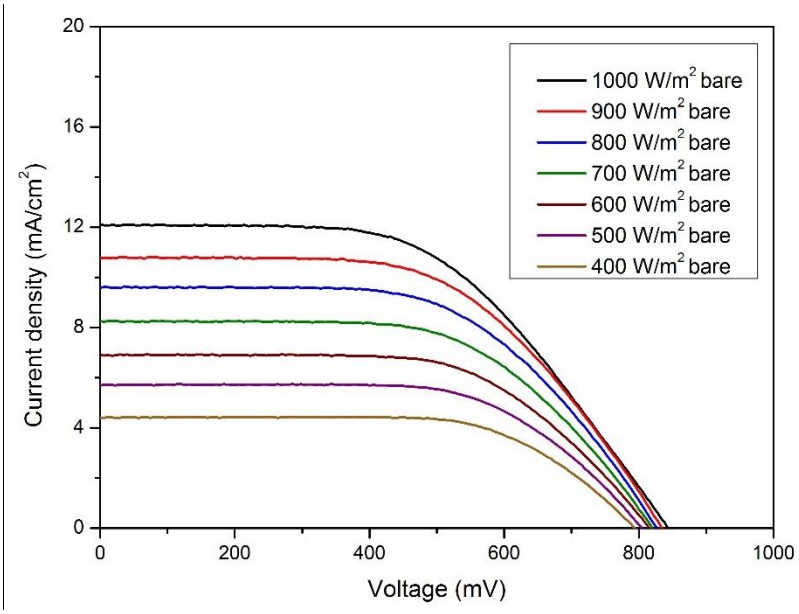

Figure 106. Photocurrent density-voltage (J-V) curves of the bare devices under different light intensities

Figure 106. depicts the current density- voltage characteristics of the bare devices. It is observed from the Table 26. that, current density of the device decreases when the light intensity decreases. Not much difference is observed in open circuit voltage since V_{OC} is given by the difference of the Fermi level of electrons in the titanium dioxide and the redox potential of the liquid electrolyte. So, light intensity doesn't have much role to play in deciding open circuit voltage of the devices. Interestingly, the fill factor goes up to 69% from 55.3% when intensity is decreased from 1000 W/m^2 to 400 W/m^2. This happens because, under low light intensity the devices have enough time to complete the redox reactions in the device interface. This the overall power conversion efficiency is improved from 5.41 % to 6.30% for the applied lowest intensity. All the photovoltaic parameters for the bare devices are given in Table 26.

Table 26. Comparison of photocurrent density - voltage (J-V) parameters of the bare cells under different light intensities.

Light intensity (W/m^2)	**J_{sc} [mA/cm^2]**	**V_{oc} [mV]**	**FF [%]**	**η [%]**
1000	12.10	843	55.3	5.41
900	10.78	839	58.4	5.70
800	9.60	832	59.6	5.89
700	8.25	824	61.4	5.99
600	6.91	816	63.5	6.06
500	5.70	802	65.8	6.24
400	4.40	796	69.0	6.30

5.5.2. Low concentrator coupled DSSCs

Following the measurement of the bare cells, the same concentrator was coupled, and the devices were tested. As shown in Figure 107, J-V characteristics are similar to the bare devices. An increase conversion efficiency is observed, a little drop in V_{oc} and the current density is decreased by 52% for the lowest light intensity to 8.58 mA/cm^2 from 18.05 mA/cm^2 for 1 sun illumination.

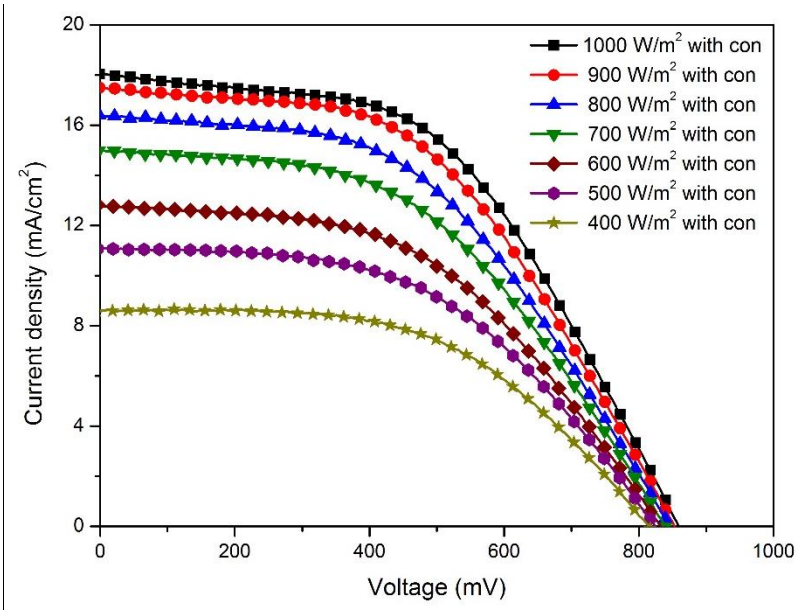

Figure 107. Photocurrent density-voltage (J-V) curves of the concentrator coupled devices under different light intensities

An increase in fill factor is seen but compare to the bare devices the number is small. This could be due to more electron recombination as the concentrator improves the intensity up to 3x. But the overall photovoltaic conversion efficiency is increased from 7.81 % for 1000 W/m^2 to 11.47 for 400 W/m^2 which is 47% improvement. All the photovoltaic parameters for the concentrator coupled devices are given in Table 27.

Table 27. Photocurrent density - voltage (J-V) parameters of the low concentrator coupled devices under different light intensities

Light intensity (W/m^2)	**J_{sc} [mA/cm^2]**	**V_{oc} [mV]**	**FF [%]**	**η [%]**
1000	18.05	859	52.2	7.81
900	17.50	854	51.2	8.38
800	16.40	849	50.3	8.88
700	14.99	841	50.2	9.57
600	12.80	834	51.0	9.97
500	11.08	820	52.4	11.00
400	8.58	814	56.0	11.47

The photovoltaic performances of the bare and concentrator coupled DSSCs under different illumination intensities are compared in Figure 108. It is clear that the DSSCs perform better under low light conditions even when the optical element is coupled. This makes them an excellent candidate for building applications. This system could also be used for indoor applications as well [271].

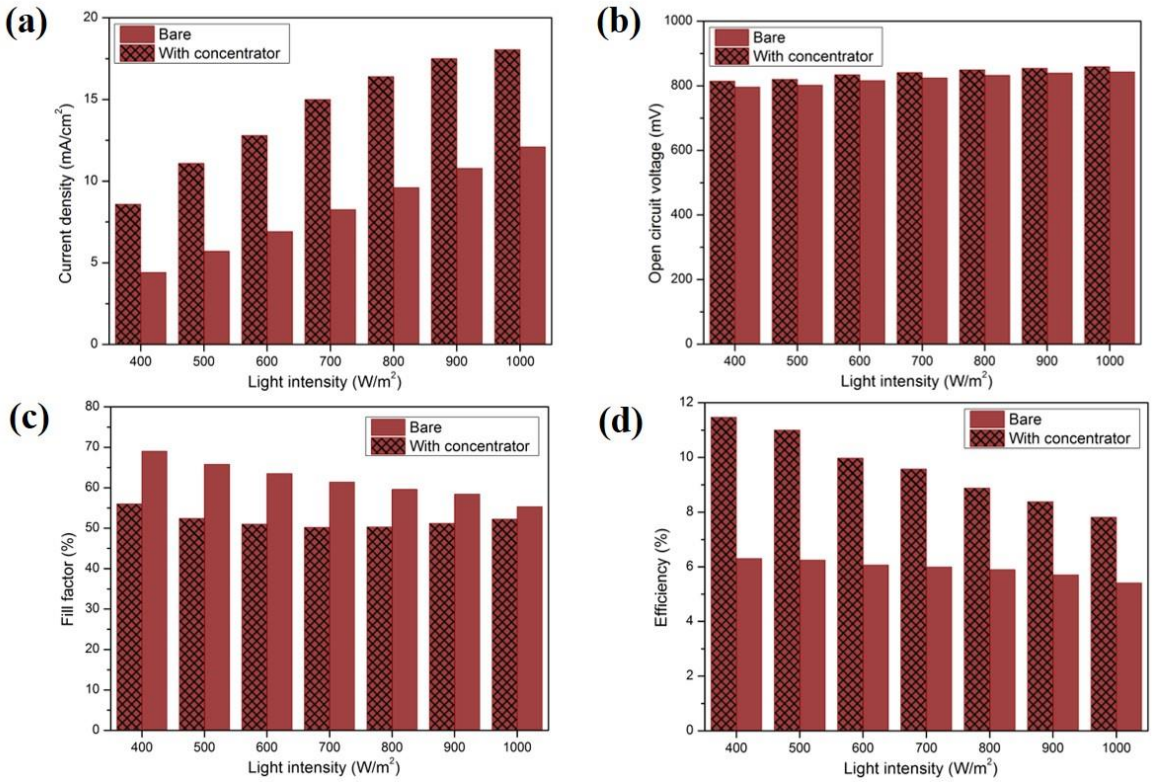

Figure 108. Figure Comparison of performance parameters of the bare and low concentrator coupled devices under different light intensities

As liquid electrolyte based DSSCs have concerns of solvent leakage and corrosion problems in the long-term process, coupling concentrators with solid state DSSCs is an option. Moreover, high efficient sensitiser such as porphyrin could be used to achieve high photovoltaic performance devices. Nevertheless, the energy payback time of DSSCs is much lower compared with silicon solar cells [137], and in addition, the low concentrators can be fabricated with low cost materials which makes this system even more economically feasible.

5.6. Conclusions

A low concentrator with 3× optical and 4× geometrical concentration was designed and employed on the devices, and the relationship between the transparency and performance of the devices has been understood. It has been found that the photovoltaic performance of the devices increases with the

thickness of the mesoporous TiO_2 electrode. Due to long electron diffusion length of high thickness devices, their pv performance decreases. In an indoor environment, the performance of transparent DSSCs coupled with low concentrator photovoltaic system was studied. The results show that the overall performance of the LCPV system coupled devices is more than 50% higher than the bare DSSCs. To estimate the impact of operating temperature of the devices due to the addition of 3× concentrating light, the devices were measured under different temperatures for both bare and concentrator coupled cells. The results obtained demonstrate that the LCPV system coupled device stability is similar to the bare devices. EIS results show that high light intensity reduces the interfacial resistances and improves the performance of DSSCs. Finally, both types of devices were tested under different light intensities from 1000 W/m^2 to 400 W/m^2. It has been found that the devices work well in low light conditions. All the above findings will offer useful insights into solve the scaling up problem of DSSCs using solar concentrators for efficient and environmentally friendly solar cells. Therefore, this system can be economically compatible with common Si solar cell-based systems, which could lead in to the application of building integrated concentrated photovoltaics to get electricity and day lighting simultaneously.

Chapter 6: Conclusions and future perspectives

Each chapter of this thesis has contained its own detailed discussion. This chapter summarises the main findings and discusses the unifying themes and wider implications as well as future perspectives.

6.1. Conclusions

The objective of this thesis was to further investigate the wider applications of dye-sensitised solar cells. A literature review was performed to understand the working mechanisms and the current research trends in DSSCs. Several novel research opportunities were identified from the literature review and three different disciplines (new materials, glazing properties and solar concentrators) were covered.

Firstly, the operating process of the DSSC is greatly dependent on the individual component properties and the interplay between them, requiring systematic analysis to gain insight into the inherent complexity of the system. To achieve a more fundamental understanding of the device mechanisms of dye-sensitised solar cells, three simple and low-cost new materials for cost effective DSSCs were introduced. The photovoltaic performance of the synthesized mesoporous TiO_2 devices is significantly higher than the commercial P25 titania electrode devices. The highest power conversion efficiency of 6.08% with a photo current density of 12.63 mA/cm^2 was achieved because of enhanced light harvesting, which is due to the high surface area. Additionally, the new m-HRD-1 sensitiser-based device achieved 20% more short circuit current due to the more effective anchoring of the dye molecules. Moreover, m-HRD-1 was stable up to 270°C, compared to N719's 270°C. Furthermore, The CZTS counter electrode DSSC showed a promising power conversion efficiency of 3.91%. Even

though this is lower than the standard Pt electrode device, the cost effectiveness of this electrode makes it a potential candidate for large scale DSSC applications. As evident from the results summarized here, it is necessary to understand the specific factors and parameters which can affect the photovoltaic performance to achieve highly efficient and low cost DSSCs.

From the literature review, it was identified that DSSCs could be used as BIPV material. In order to investigate DSSC glazing's colour and glazing properties under different environmental factors, semi-transparent DSSCs were fabricated and analysed. It was found that, the transparent DSSCs offer only 2.7% lower CRI and CCT values than the vacuum and double-glazing. In south west UK (Penryn, UK - 50.16° N, 5.10° W) the solar factor was higher in January than in July. Moreover, on a clear sunny day, 21% more glare can be reduced than double glazing using 37% transparent and 6% power conversion efficient DSSC glazing.

From the results, it was found that semi-transparent DSSC is a potential glazing system for new or retrofit windows. Building engineers and architects will be able to benefit from these results to design a new low energy or retrofit building with DSSC glazing.

From the chapter 4 results and literature review, it was understood that it is important to have large area DSSC panels for building integrated applications. However, the performance loss in DSSC scale up is one of the challenges that the scientific community is facing. A low solar concentrator was introduced for DSSC in this chapter.The photovoltaic performance of the bare semi-transparent devices was studied and the relationship between the transparency and PV performance was understood.

The photovoltaic performance of the devices increases with the thickness of the photoanode until a certain point, then for high thickness devices it starts decreasing, which is due to long electron diffusion length. The overall performance of the concentrator coupled devices was more than 50% higher than the bare DSSCs. Interestingly, an increase of 67% in power conversion efficiency was observed at 36 °C for the concentrator-coupled device under 1 sun illumination. Moreover, under different device operating temperatures, the low concentrator system coupled device stability was similar to the bare one. From the impedance studies, it was found that high light intensity reduces the interfacial resistances and improves the performance of semi-transparent DSSCs

All the above findings will provide useful insights into solving the scaling up problem of DSSCs using solar concentrators. Since the effect of device temperature does not have a significant impact on the performance, a long term stable DSSC glazing system could replace the double-glazing in the future. However, further work is needed to unlock the full potential of DSSCs, some suggestions which have been understood from the literature are given in the next section.

6.2. Future perspectives

Since this work has shown how solar concentrators could be used to improve the photovoltaic performance of the DSSCs, it is hoped that this work will trigger further work on applying concentrators for other emerging solid state solar cells such as perovskite and organic solar cells.

- Medium and high concentrators with 10- 100× optical concentration could be used for further improvement in photovoltaic performance.

- More outdoor studies need to be carried out by coupling the solar concentrators on third generation solar cells.
- These concentrators could be coupled with flexible DSSCs for indoor applications, as DSSCs work well in low light conditions.
- Device stability is obviously an important consideration for photovoltaic technologies as the longer the photovoltaic system operates, the lower is the total cost. Therefore, more outdoor device stability studies need to be carried out in order to apply this technology for building integrated applications.

Implementing this kind of new solar technology could be the way forward to achieve the goal of the Paris climate change agreement of reducing the GHG emission to keep the global warming well below 2°C. Moreover, adopting this technology could reduce the building energy consumption and provide energy access to the 20% population of the world that still live without electricity.

Bibiliography

[1] K. Sopian, B. Ali, N. Asim, Strategies for renewable energy applications in the organization of Islamic conference (OIC) countries, Renew. Sustain. Energy Rev. 15 (2011) 4706–4725. doi:10.1016/j.rser.2011.07.081.

[2] bp, Energy demand by sector, (n.d.). https://www.bp.com/en/global/corporate/energy-economics/energy-outlook/demand-by-sector.html (accessed October 28, 2018).

[3] S. Riffat, R. Powell, D. Aydin, Future cities and environmental sustainability, Futur. Cities Environ. 2 (2016) 1. doi:10.1186/s40984-016-0014-2.

[4] D. Li, J. He, L. Li, A review of renewable energy applications in buildings in the hot-summer and warm-winter region of China, Renew. Sustain. Energy Rev. 57 (2016) 327–336. doi:10.1016/j.rser.2015.12.124.

[5] S.J. Hayter, A. Kandt, F.– Alicen Kandt, Renewable Energy Applications for Existing Buildings - Preprint, 48th AiCARR Int. Conf. (2011) 1–15. http://www.osti.gov/bridge:%5Cnhttp://www.ntis.gov/help/ordermethods.aspx.

[6] T. Jin, J. Kim, What is better for mitigating carbon emissions – Renewable energy or nuclear energy? A panel data analysis, Renew. Sustain. Energy Rev. 91 (2018) 464–471. doi:10.1016/j.rser.2018.04.022.

[7] RENEWABLE ENERGY, (n.d.). https://www.studentenergy.org/topics/renewable-energy (accessed October 28, 2018).

[8] A.D. Woldeyohannes, D.E. Woldemichael, A.T. Baheta, Sustainable renewable energy resources utilization in rural areas, Renew. Sustain.

Energy Rev. 66 (2016) 1–9. doi:10.1016/j.rser.2016.07.013.

[9] Green Energy Tribune, Solar energy empowers villagers and saves wildlife in Nepal, (n.d.). https://greenenergytribune.com/solar-energy-empowers-villagers-and-saves-wildlife-in-nepal/ (accessed October 28, 2018).

[10] Global Education, Sustainable energy sources, (n.d.). https://www.globaleducation.edu.au/teaching-activity/sustainable-energy-sources-up.html (accessed October 28, 2018).

[11] J. Tsao, N. Lewis, G. Crabtree, Solar FAQs, US Dep. Energy. (2006) 1–24. http://www.sandia.gov/~jytsao/Solar FAQs.pdf.

[12] P.P. Labouchère, A Material Approach to Dye-Sensitized Solar Cells : Atomic Layer Deposition and Inverse Opal Host-Guest Architectures PAR, 2014.

[13] ASTM INTERNATIONAL, Standard Tables for Reference Solar Spectral Irradiances: Direct Normal and Hemispherical on 37° Tilted Surface, (n.d.). https://www.astm.org/Standards/G173.htm (accessed October 28, 2018).

[14] W. Shockley, H.J. Queisser, Detailed balance limit of efficiency of p-n junction solar cells, J. Appl. Phys. 32 (1961) 510–519. doi:10.1063/1.1736034.

[15] Photovoltaic energy, Shockley- Queisser Limit, (n.d.). https://photovoltaicsite.wordpress.com/2016/01/06/shockley-queisser-limit/ (accessed October 28, 2018).

[16] N. Pootrakulchote, Investigation on Functionalized Ruthenium-Based Sensitizers to Enhance Performance and Robustness of Dye-Sensitized Solar Cells, 2012.

[17] J. KRÜGER, Interface engineering in solid-state dye-sensitized solar cells(1) Kr﷿ger, J. Interface engineering in solid-state dye-sensitized solar cells. 2003, 2793., 2003.

[18] Thoughtco., Photoelectric Effect and Einstein's 1921 Nobel Prize, (n.d.). https://www.thoughtco.com/the-photoelectric-effect-2699352 (accessed October 28, 2018).

[19] L.-P. Heiniger, New Approaches for Improved Photon Management in Dye-Sensitized Solar Cells Leo-Philipp HEINIGER, 2014.

[20] T. Ibn-Mohammed, S.C.L. Koh, I.M. Reaney, A. Acquaye, G. Schileo, K.B. Mustapha, R. Greenough, Perovskite solar cells: An integrated hybrid lifecycle assessment and review in comparison with other photovoltaic technologies, Renew. Sustain. Energy Rev. 80 (2017) 1321–1344. doi:10.1016/j.rser.2017.05.095.

[21] A. Goetzberger, J. Luther, G. Willeke, Solar cells: Past, present, future, Sol. Energy Mater. Sol. Cells. 74 (2002) 1–11. doi:10.1016/S0927-0248(02)00042-9.

[22] M.A. Green, Y. Hishikawa, E.D. Dunlop, D.H. Levi, J. Hohl-Ebinger, A.W.Y. Ho-Baillie, Solar cell efficiency tables (version 52), Prog. Photovoltaics Res. Appl. 26 (2018) 427–436. doi:10.1002/pip.3040.

[23] D.A. Gore, D.A. Drew, Modifying the doping in a *pn* junction to achieve specified current-voltage characteristics, Inverse Probl. Eng. 5 (1997) 55–68. doi:10.1080/174159797088027652.

[24] J. Nelson, The Physics of solar cells, Phys. Sol. Cells. (2003).

[25] A. Dualeh, Analysis of Key Electronic , Optical and Structural Parameters

in Mesoscopic Solid-State Solar Cells PAR, 2014.

[26] A. Sproul, UNSW_Understanding_the_p-n_Junction.pdf, (n.d.).

[27] B.M. Kayes, Radial pn Junction , Wire Array Solar Cells Thesis by, 2009.

[28] J. Hanania, K. Stenhouse, Yyelland. Brodie, J. Donev, Photovoltaic effect - Energy Education, Energy Educ. (2017) 1. http://energyeducation.ca/encyclopedia/Photovoltaic_effect (accessed October 28, 2018).

[29] A. Chandra, G. Anderson, S. Melkote, W. Gao, H. Haitjema, K. Wegener, Role of surfaces and interfaces in solar cell manufacturing, CIRP Ann. - Manuf. Technol. 63 (2014) 797–819. doi:10.1016/j.cirp.2014.05.008.

[30] S. Moon, K. Kim, Y. Kim, J. Heo, J. Lee, Highly efficient single-junction GaAs thin-film solar cell on flexible substrate, Sci. Rep. 6 (2016) 1–6. doi:10.1038/srep30107.

[31] W.A. Badawy, A review on solar cells from Si-single crystals to porous materials and Quantum dots, J. Adv. Res. 6 (2015) 123–132. doi:10.1016/j.jare.2013.10.001.

[32] A. Mohammad Bagher, Types of Solar Cells and Application, Am. J. Opt. Photonics. 3 (2015) 94. doi:10.11648/j.ajop.20150305.17.

[33] S. Sharma, K.K. Jain, A. Sharma, Solar Cells: In Research and Applications—A Review, Mater. Sci. Appl. 06 (2015) 1145–1155. doi:10.4236/msa.2015.612113.

[34] J. Ramanujam, U.P. Singh, Copper indium gallium selenide based solar cells - A review, Energy Environ. Sci. 10 (2017) 1306–1319. doi:10.1039/c7ee00826k.

[35] A.A.B. Baloch, S.P. Aly, M.I. Hossain, F. El-Mellouhi, N. Tabet, F.H. Alharbi, Full space device optimization for solar cells, Sci. Rep. 7 (2017) 1–14. doi:10.1038/s41598-017-12158-0.

[36] A. Polman, M. Knight, E.C. Garnett, B. Ehrler, W.C. Sinke, Photovoltaic materials: Present efficiencies and future challenges, Science (80-.). 352 (2016). doi:10.1126/science.aad4424.

[37] S. Philipps, F. Ise, W. Warmuth, Photovoltaics Report - Fraunhofer, ISE, (2017). www.ise.fraunhofer.de.

[38] M.C. Beard, J.M. Luther, A.J. Nozik, The promise and challenge of nanostructured solar cells, Nat. Nanotechnol. 9 (2014) 951–954. doi:10.1038/nnano.2014.292.

[39] M.A. Green, The path to 25% silicon solar cell efficiency: History of silicon cell evolution, Prog. Photovoltaics Res. Appl. 17 (2009) 183–189. doi:10.1002/pip.892.

[40] J. Yan, B.R. Saunders, Third-generation solar cells: A review and comparison of polymer:fullerene, hybrid polymer and perovskite solar cells, RSC Adv. 4 (2014) 43286–43314. doi:10.1039/c4ra07064j.

[41] U. Sulaeman, A. Zuhairi Abdullah, The way forward for the modification of dye-sensitized solar cell towards better power conversion efficiency, Renew. Sustain. Energy Rev. 74 (2017) 438–452. doi:10.1016/j.rser.2017.02.063.

[42] E. Płaczek-Popko, Top PV market solar cells 2016, Opto-Electronics Rev. 25 (2017) 55–64. doi:10.1016/j.opelre.2017.03.002.

[43] A.A.F. Husain, W.Z.W. Hasan, S. Shafie, M.N. Hamidon, S.S. Pandey, A

review of transparent solar photovoltaic technologies, Renew. Sustain. Energy Rev. 94 (2018) 779–791. doi:10.1016/j.rser.2018.06.031.

[44] N. Marinova, S. Valero, J.L. Delgado, Organic and perovskite solar cells: Working principles, materials and interfaces, J. Colloid Interface Sci. 488 (2017) 373–389. doi:10.1016/j.jcis.2016.11.021.

[45] C.M. Proctor, M. Kuik, T.Q. Nguyen, Charge carrier recombination in organic solar cells, Prog. Polym. Sci. 38 (2013) 1941–1960. doi:10.1016/j.progpolymsci.2013.08.008.

[46] S. Aldridch, Organic Photovoltaics (OPV) Tutorial _ Sigma-Aldrich, (n.d.). http://www.sigmaaldrich.com/materials-science/organic-electronics/opv-tutorial.html (accessed February 24, 2016).

[47] organic solar cells working principle - Google Search, (n.d.). http://www.meh.uni-freiburg.de/research/currentresearch/fieldB/hybridzelle (accessed April 5, 2016).

[48] M.C. Scharber, N.S. Sariciftci, Efficiency of bulk-heterojunction organic solar cells, Prog. Polym. Sci. 38 (2013) 1929–1940. doi:10.1016/j.progpolymsci.2013.05.001.

[49] B. O'Regan, M. Grätzel, A low-cost, high-efficiency solar cell based on dye-sensitized colloidal TiO2 films, Nature. 353 (1991) 737–740. doi:10.1038/353737a0.

[50] H.C. Weerasinghe, F. Huang, Y.B. Cheng, Fabrication of flexible dye sensitized solar cells on plastic substrates, Nano Energy. 2 (2013) 174–189. doi:10.1016/j.nanoen.2012.10.004.

[51] M. Shakeel Ahmad, A.K. Pandey, N. Abd Rahim, Advancements in the development of TiO2photoanodes and its fabrication methods for dye sensitized solar cell (DSSC) applications. A review, Renew. Sustain. Energy Rev. 77 (2017) 89–108. doi:10.1016/j.rser.2017.03.129.

[52] B.E. Hardin, H.J. Snaith, M.D. McGehee, The renaissance of dye-sensitized solar cells, Nat. Photonics. 6 (2012) 162–169. doi:10.1038/nphoton.2012.22.

[53] S. Sarker, A.J.S. Ahammad, H.W. Seo, D.M. Kim, Electrochemical impedance spectra of dye-sensitized solar cells: Fundamentals and spreadsheet calculation, Int. J. Photoenergy. 2014 (2014). doi:10.1155/2014/851705.

[54] A. Furube, R. Katoh, K. Hara, Electron injection dynamics in dye-sensitized semiconductor nanocrystalline films, Surf. Sci. Rep. 69 (2014) 389–441. doi:10.1016/j.surfrep.2014.09.003.

[55] S. Yun, P.D. Lund, A. Hinsch, Stability assessment of alternative platinum free counter electrodes for dye-sensitized solar cells, Energy Environ. Sci. 8 (2015) 3495–3514. doi:10.1039/c5ee02446c.

[56] S. Ito, N.-L.C. Ha, G. Rothenberger, P. Liska, P. Comte, S.M. Zakeeruddin, P. P?chy, M.K. Nazeeruddin, M. Gr?tzel, High-efficiency (7.2%) flexible dye-sensitized solar cells with Ti-metal substrate for nanocrystalline-TiO2 photoanode, Chem. Commun. (2006) 4004. doi:10.1039/b608279c.

[57] T. Yamaguchi, N. Tobe, D. Matsumoto, T. Nagai, H. Arakawa, Highly efficient plastic-substrate dye-sensitized solar cells with validated conversion efficiency of 7.6%, Sol. Energy Mater. Sol. Cells. 94 (2010)

812–816. doi:10.1016/j.solmat.2009.12.029.

[58] J.H. Park, Y. Jun, H.-G. Yun, S.-Y. Lee, M.G. Kang, Fabrication of an Efficient Dye-Sensitized Solar Cell with Stainless Steel Substrate, J. Electrochem. Soc. 155 (2008) F145–F149. doi:10.1149/1.2909548.

[59] X. Huang, P. Shen, B. Zhao, X. Feng, S. Jiang, H. Chen, H. Li, S. Tan, Stainless steel mesh-based flexible quasi-solid dye-sensitized solar cells, Sol. Energy Mater. Sol. Cells. 94 (2010) 1005–1010. doi:10.1016/j.solmat.2010.02.005.

[60] J.R. Jennings, Y. Liu, Q. Wang, Efficiency limitations in dye-sensitized solar cells caused by inefficient sensitizer regeneration, J. Phys. Chem. C. 115 (2011) 15109–15120. doi:10.1021/jp2053053.

[61] M. Ye, X. Wen, M. Wang, J. Iocozzia, N. Zhang, C. Lin, Z. Lin, Recent advances in dye-sensitized solar cells: From photoanodes, sensitizers and electrolytes to counter electrodes, Mater. Today. 18 (2015) 155–162. doi:10.1016/j.mattod.2014.09.001.

[62] S. Barkaszi, J. Dunlop, Discussion of strategies for mounting photovoltaic arrays on rooftops, Sol. Eng. (2001) 333–338. doi:10.1080/714038564.

[63] B. Norton, P.C. Eames, T.K. Mallick, M.J. Huang, S.J. McCormack, J.D. Mondol, Y.G. Yohanis, Enhancing the performance of building integrated photovoltaics, Sol. Energy. 85 (2011) 1629–1664. doi:10.1016/j.solener.2009.10.004.

[64] 4green.gr, The global BIPV and BAPV markets will reach 2.25GW by 2017, (n.d.). https://www.4green.gr/news/data/diafora/94250.asp (accessed December 9, 2018).

[65] H. Baig, Enhancing Performance of Building Integrated Concentrating Photovoltaic systems, University of Exeter, 2015. http://hdl.handle.net/10871/17301.

[66] A.K. Shukla, K. Sudhakar, P. Baredar, Recent advancement in BIPV product technologies: A review, Energy Build. 140 (2017) 188–195. doi:10.1016/j.enbuild.2017.02.015.

[67] Romag, Building integrated photovoltaics/ a handbook, (n.d.). https://www.romag.co.uk/solar/building-integrated-pv/ (accessed October 28, 2018).

[68] Hermans techniglaz, Hermans Techniglaz-PowerGlaz BIPV for town hall in Midden-Delfland, (n.d.). http://hermanstechniglaz.nl/powerglaz-stadskantoor-midden-delfland/ (accessed October 28, 2018).

[69] Newatlas, Platio integrates solar panels in pedestrian walkways and street furniture, (n.d.). https://newatlas.com/platio-photovoltaic-solar-panel-paving/50549/#p473676.

[70] Florian, Solar Canopies & Awning Systems Photo Gallery, (n.d.). https://www.floriansolarproducts.com/photo.html (accessed October 28, 2018).

[71] Anu Solar power, Solar Roof Tile Installation, (n.d.). http://anusolar.com/index.php/portfolio/kerala/#prettyPhoto (accessed October 28, 2018).

[72] Solar Construction, Transparent Solar Panels, (n.d.). http://www.solar-constructions.com/wordpress/transparent-solar-panels/ (accessed October 28, 2018).

[73] T. tai Chow, C. Li, Z. Lin, Innovative solar windows for cooling-demand climate, Sol. Energy Mater. Sol. Cells. 94 (2010) 212–220. doi:10.1016/j.solmat.2009.09.004.

[74] P.W. Wong, Y. Shimoda, M. Nonaka, M. Inoue, M. Mizuno, Semi-transparent PV: Thermal performance, power generation, daylight modelling and energy saving potential in a residential application, Renew. Energy. 33 (2008) 1024–1036. doi:10.1016/j.renene.2007.06.016.

[75] B.P. Jelle, Building integrated photovoltaics: A concise description of the current state of the art and possible research pathways, Energies. 9 (2016) 1–30. doi:10.3390/en9010021.

[76] M. Casini, Active dynamic windows for buildings: A review, Renew. Energy. 119 (2018) 923–934. doi:10.1016/j.renene.2017.12.049.

[77] N. Skandalos, D. Karamanis, PV glazing technologies, Renew. Sustain. Energy Rev. 49 (2015) 306–322. doi:10.1016/j.rser.2015.04.145.

[78] M. Saifullah, J. Gwak, J.H. Yun, Comprehensive review on material requirements, present status, and future prospects for building-integrated semitransparent photovoltaics (BISTPV), J. Mater. Chem. A. 4 (2016) 8512–8540. doi:10.1039/c6ta01016d.

[79] A.K. Shukla, K. Sudhakar, P. Baredar, A comprehensive review on design of building integrated photovoltaic system, Energy Build. 128 (2016) 99–110. doi:10.1016/j.enbuild.2016.06.077.

[80] E. Biyik, M. Araz, A. Hepbasli, M. Shahrestani, R. Yao, L. Shao, E. Essah, A.C. Oliveira, T. del Caño, E. Rico, J.L. Lechón, L. Andrade, A. Mendes, Y.B. Atlı, A key review of building integrated photovoltaic (BIPV) systems,

Eng. Sci. Technol. an Int. J. 20 (2017) 833–858. doi:10.1016/j.jestch.2017.01.009.

[81] B.P. Jelle, C. Breivik, H. Drolsum Røkenes, Building integrated photovoltaic products: A state-of-the-art review and future research opportunities, Sol. Energy Mater. Sol. Cells. 100 (2012) 69–96. doi:10.1016/j.solmat.2011.12.016.

[82] A. Ghosh, S. Sundaram, T.K. Mallick, Colour properties and glazing factors evaluation of multicrystalline based semi-transparent Photovoltaic-vacuum glazing for BIPV application, Renew. Energy. 131 (2019) 730–736. doi:10.1016/j.renene.2018.07.088.

[83] Y. Sun, K. Shanks, H. Baig, W. Zhang, X. Hao, Y. Li, B. He, R. Wilson, H. Liu, S. Sundaram, J. Zhang, L. Xie, T. Mallick, Y. Wu, Integrated CdTe PV glazing into windows: energy and daylight performance for different architecture designs, Appl. Energy. (2018). doi:10.1016/j.apenergy.2018.09.133.

[84] M. Wang, J. Peng, N. Li, H. Yang, C. Wang, X. Li, T. Lu, Comparison of energy performance between PV double skin facades and PV insulating glass units, Appl. Energy. 194 (2017) 148–160. doi:10.1016/j.apenergy.2017.03.019.

[85] T.D. Lee, A.U. Ebong, A review of thin film solar cell technologies and challenges, Renew. Sustain. Energy Rev. 70 (2017) 1286–1297. doi:10.1016/j.rser.2016.12.028.

[86] M. Saifullah, J. Gwak, J.H. Yun, Comprehensive review on material requirements, present status, and future prospects for building-integrated

semitransparent photovoltaics (BISTPV), J. Mater. Chem. A. 4 (2016) 8512–8540. doi:10.1039/c6ta01016d.

[87] N. Skandalos, D. Karamanis, PV glazing technologies, Renew. Sustain. Energy Rev. 49 (2015) 306–322. doi:10.1016/j.rser.2015.04.145.

[88] E. Cuce, Toward multi-functional PV glazing technologies in low/zero carbon buildings: Heat insulation solar glass - Latest developments and future prospects, Renew. Sustain. Energy Rev. 60 (2016) 1286–1301. doi:10.1016/j.rser.2016.03.009.

[89] J. Gong, K. Sumathy, Q. Qiao, Z. Zhou, Review on dye-sensitized solar cells (DSSCs): Advanced techniques and research trends, Renew. Sustain. Energy Rev. 68 (2017) 234–246. doi:10.1016/j.rser.2016.09.097.

[90] J. Gong, J. Liang, K. Sumathy, Review on dye-sensitized solar cells (DSSCs): Fundamental concepts and novel materials, Renew. Sustain. Energy Rev. 16 (2012) 5848–5860. doi:10.1016/j.rser.2012.04.044.

[91] M. Grätzel, Dye-sensitized solar cells, J. Photochem. Photobiol. C Photochem. Rev. 4 (2003) 145–153. doi:10.1016/S1389-5567(03)00026-1.

[92] H.M. Upadhyaya, S. Senthilarasu, M.H. Hsu, D.K. Kumar, Recent progress and the status of dye-sensitised solar cell (DSSC) technology with state-of-the-art conversion efficiencies, Sol. Energy Mater. Sol. Cells. 119 (2013) 291–295. doi:10.1016/j.solmat.2013.08.031.

[93] S. Sharma, Bulkesh Siwach, S.K. Ghoshal, D. Mohan, Dye sensitized solar cells: From genesis to recent drifts, Renew. Sustain. Energy Rev. 70 (2017) 529–537. doi:10.1016/j.rser.2016.11.136.

[94] N.T.R.N. Kumara, A. Lim, C.M. Lim, M.I. Petra, P. Ekanayake, Recent progress and utilization of natural pigments in dye sensitized solar cells: A review, Renew. Sustain. Energy Rev. 78 (2017) 301–317. doi:10.1016/j.rser.2017.04.075.

[95] G. Richhariya, A. Kumar, P. Tekasakul, B. Gupta, Natural dyes for dye sensitized solar cell: A review, Renew. Sustain. Energy Rev. 69 (2017) 705–718. doi:10.1016/j.rser.2016.11.198.

[96] S. Shalini, R. Balasundara Prabhu, S. Prasanna, T.K. Mallick, S. Senthilarasu, Review on natural dye sensitized solar cells: Operation, materials and methods, Renew. Sustain. Energy Rev. 51 (2015) 1306–1325. doi:10.1016/j.rser.2015.07.052.

[97] M. Berginc, U. Opara Kra??ovec, M. Jankovec, M. Topi??, The effect of temperature on the performance of dye-sensitized solar cells based on a propyl-methyl-imidazolium iodide electrolyte, Sol. Energy Mater. Sol. Cells. 91 (2007) 821–828. doi:10.1016/j.solmat.2007.02.001.

[98] A. Parisi, R. Pernice, A. And??, A.C. Cino, V. Franzitta, A.C. Busacca, Electro-optical characterization of ruthenium-based dye sensitized solar cells: A study of light soaking, ageing and temperature effects, Optik (Stuttg). 135 (2017) 227–237. doi:10.1016/j.ijleo.2017.01.100.

[99] A. Kay, M. Grätzel, Low cost photovoltaic modules based on dye sensitized nanocrystalline titanium dioxide and carbon powder, Sol. Energy Mater. Sol. Cells. 44 (1996) 99–117. doi:10.1016/0927-0248(96)00063-3.

[100] R. Sastrawan, J. Beier, U. Belledin, S. Hemming, A. Hinsch, R. Kern, C. Vetter, F.M. Petrat, A. Prodi-Schwab, P. Lechner, W. Hoffmann, A glass

frit-sealed dye solar cell module with integrated series connections, Sol. Energy Mater. Sol. Cells. 90 (2006) 1680–1691. doi:10.1016/j.solmat.2005.09.003.

[101] M.G. Kang, N.G. Park, Y.J. Park, K.S. Ryu, S.H. Chang, Manufacturing method for transparent electric windows using dye-sensitized TiO2 solar cells, Sol. Energy Mater. Sol. Cells. 75 (2003) 475–479. doi:10.1016/S0927-0248(02)00202-7.

[102] Y. Takeda, N. Kato, K. Higuchi, A. Takeichi, T. Motohiro, S. Fukumoto, T. Sano, T. Toyoda, Monolithically series-interconnected transparent modules of dye-sensitized solar cells, Sol. Energy Mater. Sol. Cells. 93 (2009) 808–811. doi:10.1016/j.solmat.2008.09.054.

[103] W.J. Lee, E. Ramasamy, D.Y. Lee, J.S. Song, Performance variation of carbon counter electrode based dye-sensitized solar cell, Sol. Energy Mater. Sol. Cells. 92 (2008) 814–818. doi:10.1016/j.solmat.2007.12.012.

[104] EPFL, Photovoltaic glazing, the world's first on campus, (n.d.). https://actu.epfl.ch/news/un-vitrage-photovoltaique-premiere-mondiale-sur-le/ (accessed October 28, 2018).

[105] J.G. Kang, J.H. Kim, J.T. Kim, Performance evaluation of DSC windows for buildings, Int. J. Photoenergy. 2013 (2013). doi:10.1155/2013/472086.

[106] M. Morini, R. Corrao, Energy Optimization of BIPV Glass Blocks: A Multi-software Study, Energy Procedia. 111 (2017) 982–992. doi:10.1016/j.egypro.2017.03.261.

[107] A. Ghosh, P. Selvaraj, S. Sundaram, T.K. Mallick, The colour rendering index and correlated colour temperature of dye-sensitized solar cell for

adaptive glazing application, Sol. Energy. 163 (2018) 537–544. doi:10.1016/j.solener.2018.02.021.

[108] H.M. Lee, J.H. Yoon, Power performance analysis of a transparent DSSC BIPV window based on 2 year measurement data in a full-scale mock-up, Appl. Energy. 225 (2018) 1013–1021. doi:10.1016/j.apenergy.2018.04.086.

[109] C. Cornaro, L. Renzi, M. Pierro, A. Di Carlo, A. Guglielmotti, Thermal and electrical characterization of a semi-transparent dye-sensitized photovoltaic module under real operating conditions, Energies. 11 (2018). doi:10.3390/en11010155.

[110] A. Ghosh, B. Norton, Interior colour rendering of daylight transmitted through a suspended particle device switchable glazing, Sol. Energy Mater. Sol. Cells. 163 (2017) 218–223. doi:10.1016/j.solmat.2017.01.041.

[111] R.G. Davis, D.N. Grinthner, Correlated color temperature, illuminance level, and the Kruithof curve, J. Illum. Eng. Soc. 19 (1990) 27–38.

[112] M.R. Luo, The quality of light sources, Color. Technol. 127 (2011) 75–87.

[113] B.W. D'Andrade, S.R. Forrest, White organic light-emitting devices for solid-state lighting, Adv. Mater. 16 (2004) 1585–1595.

[114] A.R. Webb, Considerations for lighting in the built environment: Non-visual effects of light, Energy Build. 38 (2006) 721–727. doi:10.1016/j.enbuild.2006.03.004.

[115] W.J.M. Van Bommel, J.G. van der Beld, Lighting for work: a review of visual and biological effects, Light. Res. Technol. 36 (2004) 255–269.

[116] M.K. Gunde, U.O. Krašovec, W.J. Platzer, Color rendering properties of

interior lighting influenced by a switchable window, J. Opt. Soc. Am. A. 22 (2005) 416. doi:10.1364/JOSAA.22.000416.

[117] C. Chain, D. Dumortier, M. Fontoynont, Consideration of daylight's colour, Energy Build. 33 (2001) 193–198. doi:10.1016/S0378-7788(00)00081-5.

[118] X. Gong, S. Wang, D. Moses, G.C. Bazan, A.J. Heeger, Multilayer polymer light-emitting diodes: White-light emission with high efficiency, Adv. Mater. 17 (2005) 2053–2058.

[119] X. Niu, L. Ma, B. Yao, J. Ding, G. Tu, Z. Xie, L. Wang, White polymeric light-emitting diodes with high color rendering index, Appl. Phys. Lett. 89 (2006) 213508.

[120] J. Hernández-Andrés, R.L. Lee, J. Romero, Calculating correlated color temperatures across the entire gamut of daylight and skylight chromaticities., Appl. Opt. 38 (1999) 5703–9. doi:10.1364/AO.38.005703.

[121] J. Mardaljevic, How to Maintain Neutral Daylight Illumination with SageGlass ® Electrochromic Glazing (whitepaper), (2014) 18.

[122] B.P. Jelle, A. Hynd, A. Gustavsen, D. Arasteh, H. Goudey, R. Hart, Fenestration of today and tomorrow: A state-of-the-art review and future research opportunities, Sol. Energy Mater. Sol. Cells. 96 (2012) 1–28. doi:10.1016/j.solmat.2011.08.010.

[123] E. Ramasamy, W.J. Lee, D.Y. Lee, J.S. Song, Portable, parallel grid dye-sensitized solar cell module prepared by screen printing, J. Power Sources. 165 (2007) 446–449. doi:10.1016/j.jpowsour.2006.11.057.

[124] A. Hinsch, H. Brandt, W. Veurman, S. Hemming, M. Nittel, U. Würfel, P. Putyra, C. Lang-Koetz, M. Stabe, S. Beucker, K. Fichter, Dye solar modules

for facade applications: Recent results from project ColorSol, Sol. Energy Mater. Sol. Cells. 93 (2009) 820–824. doi:10.1016/j.solmat.2008.09.049.

[125] E. Stathatos, Dye Sensitized Solar Cells: A New Prospective to the Solar to Electrical Energy Conversion. Issues to be Solved for Efficient Energy Harvesting., Eng. Sci. Technol. Rev. 5 (2012) 9–13.

[126] Grren Rhino Energy, Concentrating Photovoltaics _ Solar Power, (n.d.). http://www.greenrhinoenergy.com/solar/technologies/pv_concentration.php (accessed December 12, 2018).

[127] D. Chemisana, Building integrated concentrating photovoltaics: A review, Renew. Sustain. Energy Rev. 15 (2011) 603–611. doi:10.1016/j.rser.2010.07.017.

[128] H. Baig, K.C. Heasman, T.K. Mallick, Non-uniform illumination in concentrating solar cells, Renew. Sustain. Energy Rev. 16 (2012) 5890–5909. doi:10.1016/j.rser.2012.06.020.

[129] H. Baig, N. Sellami, T.K. Mallick, Performance modeling and testing of a Building Integrated Concentrating Photovoltaic (BICPV) system, Sol. Energy Mater. Sol. Cells. 134 (2015) 29–44. doi:10.1016/j.solmat.2014.11.019.

[130] K. Shanks, S. Senthilarasu, T.K. Mallick, Optics for concentrating photovoltaics : Trends , limits and opportunities for materials and design, Renew. Sustain. Energy Rev. 60 (2016) 394–407. doi:10.1016/j.rser.2016.01.089.

[131] H.G. Agrell, J. Lindgren, A. Hagfeldt, Degradation mechanisms in a dye-sensitized solar cell studied by UV-VIS and IR spectroscopy, Sol. Energy.

75 (2003) 169–180. doi:10.1016/S0038-092X(03)00248-2.

[132] Build Solar, Solar Squared | United Kingdom | BUILDSOLAR, (2017). https://www.buildsolar.co.uk/ (accessed October 28, 2018).

[133] Gigaom, Gigaom _ The World's Largest Solar CPV Farm, Courtesy of Amonix, (n.d.). https://gigaom.com/2010/08/09/the-worlds-largest-solar-cpv-farm-courtesy-of-amonix/ (accessed October 28, 2018).

[134] S.D. Ã, K. Wang, J. Weng, Y. Sui, Y. Huang, S. Xiao, S. Chen, L. Hu, F. Kong, X. Pan, C. Shi, L. Guo, Design of DSC panel with efficiency more than 6 % $, 85 (2005) 447–455. doi:10.1016/j.solmat.2004.10.001.

[135] S. Casaluci, M. Gemmi, V. Pellegrini, A. Di Carlo, F. Bonaccorso, Nanoscale, (2016). doi:10.1039/C5NR07971C.

[136] S. Dai, J. Weng, Y. Sui, C. Shi, Y. Huang, S. Chen, X. Pan, X. Fang, L. Hu, F. Kong, K. Wang, Dye-sensitized solar cells , from cell to module $, 84 (2004) 125–133. doi:10.1016/j.solmat.2004.03.002.

[137] K.J. Moon, S.W. Lee, Y.H. Lee, J.H. Kim, J.Y. Ahn, S.J. Lee, D.W. Lee, S.H. Kim, Effect of TiO2 nanoparticle-accumulated bilayer photoelectrode and condenser lens-assisted solar concentrator on light harvesting in dye-sensitized solar cells., Nanoscale Res. Lett. 8 (2013) 283. doi:10.1186/1556-276X-8-283.

[138] S. Choi, E. Cho, S. Lee, Y. Kim, D. Lee, Development of a high-efficiency laminated dye-sensitized solar cell with a condenser lens., Opt. Express. 19 Suppl 4 (2011) A818-23. doi:10.1364/OE.19.00A818.

[139] G.D. Barber, P.G. Hoertz, S.H.A. Lee, N.M. Abrams, J. Mikulca, T.E. Mallouk, P. Liska, S.M. Zakeeruddin, M. Grätzel, A. Ho-Baillie, M.A. Green,

Utilization of direct and diffuse sunlight in a dye-sensitized solar cell - Silicon photovoltaic hybrid concentrator system, J. Phys. Chem. Lett. 2 (2011) 581–585. doi:10.1021/jz200112m.

[140] A. Sacco, M. Gerosa, S. Bianco, L. Mercatelli, R. Fontana, L. Pezzati, M. Quaglio, C.F. Pirri, A.O.M. Tucci, Dye-sensitized solar cell for a solar concentrator system, Sol. Energy. 125 (2016) 307–313. doi:10.1016/j.solener.2015.11.026.

[141] V. More, V. Shivade, P. Bhargava, Effect of Cleaning Process of Substrate on the Efficiency of the DSSC, Trans. Indian Ceram. Soc. 5456 (2016) 1–4. doi:10.1080/0371750X.2016.1149100.

[142] NSG TEC™ for Solar Applications, (n.d.). https://www.pilkington.com/en/global/products/product-categories/solar-energy/nsg-tec-for-solar-applications#productrange (accessed October 19, 2018).

[143] TCO22-15 - Electrode Materials - Solaronix, (n.d.). http://shop.solaronix.com/electrode-materials/tco22-15.html (accessed October 19, 2018).

[144] Titania & Platinum Pastes - Materials, (n.d.). http://www.greatcellsolar.com/shop/dsc-materials/pastes.html (accessed October 19, 2018).

[145] S.R. Gajjela, K. Ananthanarayanan, C. Yap, M. Gr, Synthesis of mesoporous titanium dioxide by soft template based approach : characterization and application in dye-sensitized solar cells †, (2010) 838–845. doi:10.1039/b921360k.

[146] M. Hoc, Development of TiO 2 pastes modified with Pechini sol – gel method for high efficiency dye-sensitized solar cell, (2008) 156–162. doi:10.1007/s10971-008-1763-7.

[147] S. Ito, T.N. Murakami, P. Comte, P. Liska, C. Grätzel, M.K. Nazeeruddin, M. Grätzel, Fabrication of thin film dye sensitized solar cells with solar to electric power conversion efficiency over 10%, Thin Solid Films. 516 (2008) 4613–4619. doi:10.1016/j.tsf.2007.05.090.

[148] C.P. Lee, R.Y.Y. Lin, L.Y. Lin, C.T. Li, T.C. Chu, S.S. Sun, J.T. Lin, K.C. Ho, Recent progress in organic sensitizers for dye-sensitized solar cells, RSC Adv. 5 (2015) 23810–23825. doi:10.1039/c4ra16493h.

[149] Ruthenizer 535-bisTBA - Sensitizing Dyes - Solaronix, (n.d.). http://shop.solaronix.com/sensitizing-dyes/ruthenizer-535-bistba.html (accessed October 19, 2018).

[150] W.S. Wadsworth, W.D. Emmons, The Utility of Phosphonate Carbanions in Olefin Synthesis, J. Am. Chem. Soc. 83 (1961) 1733–1738. doi:10.1021/ja01468a042.

[151] N.A.S. Miyaura, Stereoselective Synthesis of Arylated (E)-Alkenes..., J. C. S. Chem. Comm. (1979) 866–867. doi:10.1039/C39790000866.

[152] L. Giribabu, T. Bessho, M. Srinivasu, C. Vijaykumar, Y. Soujanya, V.G. Reddy, P.Y. Reddy, J.H. Yum, M. Grätzel, M.K. Nazeeruddin, A new familiy of heteroleptic ruthenium(ii) polypyridyl complexes for sensitization of nanocrystalline TiO2films, Dalt. Trans. 40 (2011) 4497–4504. doi:10.1039/c0dt01417f.

[153] Z.S. Wang, T. Yamaguchi, H. Sugihara, H. Arakawa, Significant efficiency

improvement of the black dye-sensitized solar cell through protonation of TiO2films, Langmuir. 21 (2005) 4272–4276. doi:10.1021/la050134w.

[154] Meltonix 1170-25 - Sealing Materials - Solaronix, (n.d.). http://shop.solaronix.com/sealing-materials/meltonix-1170-25.html (accessed October 19, 2018).

[155] S. Senthilarasu, T.A.N. Peiris, J. García-Cañadas, K.G.U. Wijayantha, Preparation of nanocrystalline TiO 2 electrodes for flexible dye-sensitized solar cells: Influence of mechanical compression, J. Phys. Chem. C. 116 (2012) 19053–19061. doi:10.1021/jp301638p.

[156] Platisol T - Platinum Pastes - Solaronix, (n.d.). http://shop.solaronix.com/platinum-catalysts/platisol-t.html (accessed October 19, 2018).

[157] D.D. Kirubakaran, S. Pitchaimuthu, C.R. Dhas, P. Selvaraj, S.Z. Karazhanov, S. Sundaram, Jet-nebulizer-spray coated copper zinc tin sulphide film for low cost platinum-free electrocatalyst in solar cells, Mater. Lett. 220 (2018) 122–125. doi:10.1016/j.matlet.2018.02.122.

[158] P. Sudhagar, S. Nagarajan, Y.G. Lee, D. Song, T. Son, W. Cho, M. Heo, K. Lee, J. Won, Y.S. Kang, Synergistic catalytic effect of a composite (CoS/PEDOT:PSS) counter electrode on triiodide reduction in dye-sensitized solar cells, ACS Appl. Mater. Interfaces. 3 (2011) 1838–1843. doi:10.1021/am2003735.

[159] O.A. Journal, Synthesis and Photo Electrochemical Characterization of an Extended π-Conjugated Heteroleptic Ruthenium (II) Complex, 1 (2017) 1–7. doi:10.15406/oajp.2017.01.00007.

[160] D. Fuchs, H. Sigmund, Analysis of the current-voltage characteristic of solar cells, Solid. State. Electron. 29 (1986) 791–795. doi:10.1016/0038-1101(86)90181-4.

[161] J. Zhang, S.T. Lee, B. Sun, Effect of series and shunt resistance on organic-inorganic hybrid solar cells performance, Electrochim. Acta. 146 (2014) 845–849. doi:10.1016/j.electacta.2014.08.065.

[162] PV education, Solar Cell Efficiency | PVEducation, (n.d.). http://www.pveducation.org/pvcdrom/solar-cell-efficiency (accessed October 19, 2018).

[163] Introduction to Solar Radiation, Dalt. Trans. 39 (2010) 10286. http://www.newport.com/Introduction-to-Solar-Radiation/411919/1033/content.aspx (accessed October 19, 2018).

[164] L. Micheli, Enhancing Electrical and Heat Transfer Performance of High-Concentrating Photovoltaic Receivers, 2015. http://hdl.handle.net/10871/18484.

[165] Q. Wang, J.E. Moser, M. Grätzel, Electrochemical impedance spectroscopic analysis of dye-sensitized solar cells, J. Phys. Chem. B. 109 (2005) 14945–53. doi:10.1021/jp052768h.

[166] J. Wu, Z. Lan, J. Lin, M. Huang, Y. Huang, L. Fan, G. Luo, Y. Lin, Y. Xie, Y. Wei, Counter electrodes in dye-sensitized solar cells, Chem. Soc. Rev. 46 (2017) 5975–6023. doi:10.1039/c6cs00752j.

[167] M.L.M.S.A. Abdel-mottaleb, A facile low temperature synthesis of TiO 2 nanorods for high efficiency dye sensitized solar cells, (2013) 111–122. doi:10.1007/s00339-012-7368-6.

[168] D. Rangel, J. Navarro, S. Vargas, M. González, V.M. Castaño, R. Rodríguez, A novel dual mechanism in dye-sensitized solar cells, (2017) 1164–1170. doi:10.1002/er.

[169] R. Sahnoun, A. Govindasamy, A. Miyamoto, Efficiency enhancement of dye-sensitized TiO 2 solar cell based on ruthenium(II) terpyridyl complex photosensitizer, Int. J. Energy Res. 39 (2015) 977–992. doi:10.1002/er.4288.

[170] B. Dawoud, E. Amer, D. Gross, Experimental investigation of an adsorptive thermal energy storage, Int. J. Energy Res. 31 (2007) 135–147. doi:10.1002/er.

[171] S. Shalini, R. Balasundaraprabhu, T.S. Kumar, N. Prabavathy, S. Senthilarasu, Status and outlook of sensitizers / dyes used in dye sensitized solar cells (DSSC): a review, (2016) 1303–1320. doi:10.1002/er.

[172] H. Diker, C. Varlikli, E. Stathatos, N-doped titania powders prepared by different nitrogen sources and their application in quasi-solid state dye-sensitized solar cells, Int. J. Energy Res. 38 (2014) 908–917. doi:10.1002/er.3091.

[173] P. Selvaraj, H. Baig, T.K. Mallick, S. Sundaram, Charge transfer mechanics in transparent dye-sensitised solar cells under low concentration, Mater. Lett. (2018). doi:10.1016/j.matlet.2018.03.137.

[174] W. Cheng, J.R. Deka, Y. Chiang, A. Rogeau, S. Lu, One-Step , Surfactant-Free Hydrothermal Method for Syntheses of Mesoporous TiO 2 Nanoparticle Aggregates and Their Applications in High E ffi ciency Dye-

Sensitized Solar Cells, (2012). doi:10.1021/cm3017616.

[175] J.J. Silva, J.A. Varela, E. Joanni, R. Parra, P.R. Bueno, Synthesis and characterization of mesoporous TiO 2 nanostructured films prepared by a modified sol – gel method for application in dye solar cells, 37 (2011) 1017–1024. doi:10.1016/j.ceramint.2010.11.014.

[176] C. Yu, X. Li, Z. Liu, X. Yang, Y. Huang, J. Lin, J. Zhang, C. Tang, Synthesis of hierarchically porous TiO 2 nanomaterials using alginate as soft templates, Mater. Res. Bull. 83 (2016) 609–614. doi:10.1016/j.materresbull.2016.07.014.

[177] E. Ramasamy, C. Jo, A. Anthonysamy, I. Jeong, J.K. Kim, J. Lee, Soft-Template Simple Synthesis of Ordered Mesoporous Titanium Nitride-Carbon Nanocomposite for High Performance Dye-Sensitized Solar Cell Counter Electrodes, (2012). doi:10.1021/cm203672g.

[178] M.M. Byranvand, A.N. Kharat, L. Fatholahi, Z.M. Beiranvand, A Review on Synthesis of Nano-TiO 2 via Different Methods, 3 (2013) 1–9.

[179] F. Cao, S. Xin, Y. Guo, L. Wan, nano-current-collectors as high-rate anode materials in lithium-ion, (2014) 2014–2020. doi:10.1039/c0cp01119c.

[180] M. Tio, Energy & Environmental Science, (2010). doi:10.1039/c003630g.

[181] M. Ye, C. Chen, M. Lv, D. Zheng, W. Guo, C. Lin, spheres for e ffi cient dye-sensitized solar cells †, (2013) 6577–6583. doi:10.1039/c3nr01604h.

[182] P.P. Das, A. Roy, P. Sujatha, eosin Y dye molecules for DSSC application †, Phys. Chem. Chem. Phys. 18 (2015) 1429–1438. doi:10.1039/C5CP04716A.

[183] P. Pratim, A. Roy, M. Tathavadekar, P.S. Devi, Applied Catalysis B :

Environmental Photovoltaic and photocatalytic performance of electrospun Zn 2 SnO 4 hollow fibers, "Applied Catal. B, Environ. 203 (2017) 692–703. doi:10.1016/j.apcatb.2016.10.035.

[184] A. Roy, P.P. Das, M. Tathavadekar, S. Das, P.S. Devi, Performance of colloidal CdS sensitized solar cells with ZnO nanorods / nanoparticles, (2017) 210–221. doi:10.3762/bjnano.8.23.

[185] X. Wang, Y. Xiao, C. Xie, arrays for enhanced light harvesting by a light, CrystEngComm. 17 (2015) 1151–1158. doi:10.1039/C4CE02129K.

[186] Z. Arifin, S. Soeparman, D. Widhiyanuriyawan, S. Suyitno, Performance Enhancement of Dye-Sensitized Solar Cells Using a Natural Sensitizer, 2017 (2017).

[187] N. Tasi, Z. Brankovi, Ž. Milan, T. Novakovi, M. Podlogar, G. Brankovi, Electrochimica Acta Mesoporous fi lms prepared from synthesized TiO 2 nanoparticles and their application in dye-sensitized solar cells (DSSCs), 210 (2016) 606–614. doi:10.1016/j.electacta.2016.05.179.

[188] Q. Wang, J. Moser, M. Gra, Electrochemical Impedance Spectroscopic Analysis of Dye-Sensitized Solar Cells, (2005) 14945–14953. doi:10.1021/jp052768h.

[189] C. Longo, A.F. Nogueira, M. De Paoli, Solid-State and Flexible Dye-Sensitized TiO 2 Solar Cells : a Study by Electrochemical Impedance Spectroscopy, (2002) 5925–5930.

[190] W.-Q. Wu, B.-X. Lei, H.-S. Rao, Y.-F. Xu, Y.-F. Wang, C.-Y. Su, D.-B. Kuang, Hydrothermal fabrication of hierarchically anatase TiO2 nanowire arrays on FTO glass for dye-sensitized solar cells., Sci. Rep. 3 (2013) 1352.

doi:10.1038/srep01352.

[191] Z. Yao, M. Zhang, H. Wu, L. Yang, R. Li, P. Wang, Donor/Acceptor Indenoperylene Dye for Highly Efficient Organic Dye-Sensitized Solar Cells, J. Am. Chem. Soc. 137 (2015) 3799–3802. doi:10.1021/jacs.5b01537.

[192] B. O'Regan, M. Gratzel, A Low-Cost, High-Efficiency Solar-Cell Based on Dye-Sensitized Colloidal TiO_2 Films, Nature. 353 (1991) 737–740. doi:10.1038/353737a0.

[193] M.K. Nazeeruddin, P. Péchy, T. Renouard, S.M. Zakeeruddin, R. Humphry-Baker, P. Cointe, P. Liska, L. Cevey, E. Costa, V. Shklover, L. Spiccia, G.B. Deacon, C.A. Bignozzi, M. Grätzel, Engineering of efficient panchromatic sensitizers for nanocrystalline TiO2-based solar cells, J. Am. Chem. Soc. 123 (2001) 1613–1624. doi:10.1021/ja003299u.

[194] M. Grätzel, Recent Advances in Sensitized Mesoscopic Solar Cells, Acc. Chem. Res. 42 (2009) 1788–1798. doi:10.1021/ar900141y.

[195] D.P. Hagberg, J.J.-H. Yum, H. Lee, F. De Angelis, T. Marinado, K.M. Karlsson, R. Humphry-Baker, L. Sun, A. Hagfeldt, M. Grätzel, K. Nazeeruddin, F. De Angelis, T. Marinado, K.M. Karlsson, R. Humphry-Baker, L. Sun, A. Hagfeldt, M. Grätzel, M.K.K. Nazeeruddin, Molecular engineering of organic sensitizers for dye-sensitized solar cell applications, J. Am. Chem. Soc. 130 (2008) 6259–6266. doi:10.1021/ja800066y.

[196] N. Robertson, Optimizing dyes for dye-sensitized solar cells, Angew. Chemie - Int. Ed. 45 (2006) 2338–2345. doi:10.1002/anie.200503083.

[197] M.K. Nazeeruddin, A. Kay, I. Rodicio, R. Humphry-Baker, E. Müller, P.

Liska, N. Vlachopoulos, M. Grätzel, Conversion of Light to Electricity by cis-X2Bis (2,2′-bipyridyl-4,4′-dicarboxylate) ruthenium (II) Charge-Transfer Sensitizers (X = Cl−, Br−, I−, CN−, and SCN−) on Nanocrystalline TiO2Electrodes, J. Am. Chem. Soc. 115 (1993) 6382–6390. doi:10.1021/ja00067a063.

[198] P. Wang, S.M. Zakeeruddin, J.E. Moser, M.K. Nazeeruddin, T. Sekiguchi, M. Grätzel, A stable quasi-solid-state dye-sensitized solar cell with an amphiphilic ruthenium sensitizer and polymer gel electrolyte, Nat. Mater. 2 (2003) 402–407. doi:10.1038/nmat904.

[199] P. Wang, S.M. Zakeeruddin, J.E. Moser, R. Humphry-Baker, P. Comte, V. Aranyos, A. Hagfeldt, M.K. Nazeeruddin, M. Grätzel, Stable new sensitizer with improved light harvesting for nanocrystalline dye-sensitized solar cells, Adv. Mater. 16 (2004) 1806–1811. doi:10.1002/adma.200400039.

[200] P. Wang, C. Klein, R. Humphry-Baker, S.M. Zakeeruddin, M. Gr??tzel, A high molar extinction coefficient sensitizer for stable dye-sensitized solar cells, J. Am. Chem. Soc. 127 (2005) 808–809. doi:10.1021/ja0436190.

[201] L. Giribabu, V.K. Singh, C. Vijay Kumar, Y. Soujanya, V. Gopal Reddy, P. Yella Reddy, Organic-ruthenium(II) polypyridyl complex based sensitizer for dye-sensitized solar cell applications, Adv. Optoelectron. 2011 (2011). doi:10.1155/2011/294353.

[202] M. Chandrasekharam, G. Rajkumar, T. Suresh, C.S. Rao, P.Y. Reddy, J.H. Yum, M.K. Nazeeruddin, M. Graetzel, Substitution of carbazole modified fluorenes as π-extension in Ru(II) complex-influence on performance of dye-sensitized solar cells, Adv. Optoelectron. 2011 (2011) 22–24. doi:10.1155/2011/963068.

[203] L. Giribabu, C. Vijay Kumar, C.S. Rao, V.G. Reddy, P.Y. Reddy, M. Chandrasekharam, Y. Soujanya, High molar extinction coefficient amphiphilic ruthenium sensitizers for efficient and stable mesoscopic Dye-sensitized solar cells, Energy Environ. Sci. 2 (2009) 770–773. doi:10.1039/b903967h.

[204] F. Gao, Y. Wang, D. Shi, J. Zhang, M. Wang, X. Jing, R. Humphry-baker, P. Wang, S.M. Zakeeruddin, M. Gra, Enhance the Optical Absorptivity of Nanocrystalline TiO Film with High Molar Extinction Coefficient Ruthenium Sensitizers for High Performance Dye-Sensitized Solar Cells Enhance the Optical Absorptivity of Nanocrystalline TiO 2 Film with High Molar Extinc, (2008) 10720–10728. doi:10.1021/ja801942j.

[205] C.Y. Chen, S.J. Wu, C.G. Wu, J.G. Chen, K.C. Ho, A ruthenium complex with superhigh light-harvesting capacity for dye-sensitized solar cells, Angew. Chemie - Int. Ed. 45 (2006) 5822–5825. doi:10.1002/anie.200601463.

[206] M.J.G. Peach, P. Benfield, T. Helgaker, D.J. Tozer, Excitation energies in density functional theory: An evaluation and a diagnostic test, J. Chem. Phys. 128 (2008) 044118. doi:10.1063/1.2831900.

[207] M.K. Nazeeruddin, T. Bessho, L. Cevey, S. Ito, C. Klein, F. De Angelis, S. Fantacci, P. Comte, P. Liska, H. Imai, M. Graetzel, A high molar extinction coefficient charge transfer sensitizer and its application in dye-sensitized solar cell, J. Photochem. Photobiol. A Chem. 185 (2007) 331–337. doi:10.1016/j.jphotochem.2006.06.028.

[208] J. Briscoe, S. Dunn, The Future of Using Earth-Abundant Elements in Counter Electrodes for Dye-Sensitized Solar Cells, Adv. Mater. 28 (2016)

3802–3813. doi:10.1002/adma.201504085.

[209] M. Wu, X. Lin, Y. Wang, L. Wang, W. Guo, D. Qi, X. Peng, A. Hagfeldt, M. Grätzel, T. Ma, Economical Pt-free catalysts for counter electrodes of dye-sensitized solar cells, J. Am. Chem. Soc. 134 (2012) 3419–3428. doi:10.1021/ja209657v.

[210] Z. Shi, K. Deng, L. Li, Pt-free and efficient counter electrode with nanostructured CoNi2S4 for dye-sensitized solar cells., Sci. Rep. 5 (2015) 9317. doi:10.1038/srep09317.

[211] J. Xu, H. Xue, X. Yang, H. Wei, W. Li, Z. Li, W. Zhang, C.S. Lee, Synthesis of honeycomb-like Mesoporous pyrite FeS2Microspheres as efficient counter electrode in quantum dots sensitized solar cells, Small. 10 (2014) 4754–4759. doi:10.1002/smll.201401102.

[212] Z. Yang, C.Y. Chen, C.W. Liu, C.L. Li, H.T. Chang, Quantum dot-sensitized solar cells featuring CuS/CoS electrodes provide 4.1% efficiency, Adv. Energy Mater. 1 (2011) 259–264. doi:10.1002/aenm.201000029.

[213] S. Chen, A. Xu, J. Tao, H. Tao, Y. Shen, L. Zhu, J. Jiang, T. Wang, L. Pan, In-Situ and Green Method To Prepare Pt-Free Cu_2ZnSnS_4 (CZTS) Counter Electrodes for Efficient and Low Cost Dye-Sensitized Solar Cells, ACS Sustain. Chem. Eng. 3 (2015) 2652–2659. doi:10.1021/acssuschemeng.5b00585.

[214] S. Chen, J. Tao, H. Tao, Y. Shen, L. Zhu, J. Jiang, X. Zeng, T. Wang, Fabrication of low cost kesterite Cu_2ZnSnS_4 (CZTS) thin films as counter-electrode for dye sensitised solar cells (DSSCs), Mater. Technol. 30 (2015) 306–312. doi:10.1179/1753555715Y.0000000007.

[215] X. Xin, M. He, W. Han, J. Jung, Z. Lin, Low-cost copper zinc tin sulfide counter electrodes for high-efficiency dye-sensitized solar cells, Angew. Chemie - Int. Ed. 50 (2011) 11739–11742. doi:10.1002/anie.201104786.

[216] X. Zhang, X. Wu, A. Centeno, M.P. Ryan, N.M. Alford, D.J. Riley, F. Xie, Significant Broadband Photocurrent Enhancement by Au-CZTS Core-Shell Nanostructured Photocathodes, Sci. Rep. 6 (2016) 1–8. doi:10.1038/srep23364.

[217] S. Chen, A. Walsh, X.-G. Gong, S.-H. Wei, Classification of Lattice Defects in the Kesterite Cu_2ZnSnS_4 and $Cu_2ZnSnSe_4$ Earth-Abundant Solar Cell Absorbers, Adv. Mater. 25 (2013) 1522–1539. doi:10.1002/adma.201203146.

[218] S.S. Latthe, P. Sudhagar, C. Ravidhas, A. Jennifer Christy, D. David Kirubakaran, R. Venkatesh, A. Devadoss, C. Terashima, K. Nakata, A. Fujishima, Self-cleaning and superhydrophobic CuO coating by jet-nebulizer spray pyrolysis technique, CrystEngComm. 17 (2015) 2624–2628. doi:10.1039/c5ce00177c.

[219] Hans-Wilhelm, H. Schiffer, World Energy Resources | 2016, World Energy Counc. (2016) 1–10. https://www.worldenergy.org/publications/2016/world-energy-resources-2016/ (accessed October 3, 2018).

[220] U.S. Energy Information Administration, (n.d.). https://www.eia.gov/ (accessed October 3, 2018).

[221] E. Halawa, A. Ghaffarianhoseini, A. Ghaffarianhoseini, J. Trombley, N. Hassan, M. Baig, S.Y. Yusoff, M. Azzam Ismail, A review on energy

conscious designs of building façades in hot and humid climates: Lessons for (and from) Kuala Lumpur and Darwin, Renew. Sustain. Energy Rev. 82 (2018) 2147–2161. doi:10.1016/j.rser.2017.08.061.

[222] M. Sudan, G.N. Tiwari, Energy matrices of the building by incorporating daylight concept for composite climate - An experimental study, J. Renew. Sustain. Energy. 6 (2014). doi:10.1063/1.4898364.

[223] A. Ghosh, B. Norton, A. Duffy, Daylighting performance and glare calculation of a suspended particle device switchable glazing, Sol. Energy. 132 (2016) 114–128. doi:http://dx.doi.org/10.1016/j.solener.2016.02.051.

[224] A. Ghosh, B. Norton, A. Duffy, Measured thermal & daylight performance of an evacuated glazing using an outdoor test cell, Appl. Energy. 177 (2016) 196–203. doi:10.1016/j.apenergy.2016.05.118.

[225] D.H.W. Li, E.K.W. Tsang, An analysis of daylighting performance for office buildings in Hong Kong, Build. Environ. 43 (2008) 1446–1458. doi:10.1016/j.buildenv.2007.07.002.

[226] A. Ghosh, B. Norton, Advances in switchable and highly insulating autonomous (self-powered) glazing systems for adaptive low energy buildings, Renew. Energy. 126 (2018) 1003–1031. doi:10.1016/j.renene.2018.04.038.

[227] A. Ghosh, S. Sundaram, T.K. Mallick, Investigation of thermal and electrical performances of a combined semi- transparent PV-vacuum glazing, Appl. Energy. 228 (2018) 1591–1600. doi:10.1016/j.apenergy.2018.07.040.

[228] A. Ghosh, B. Norton, A. Duffy, Measured thermal performance of a combined suspended particle switchable device evacuated glazing, Appl.

Energy. 169 (2016) 469–480. doi:10.1016/j.apenergy.2016.02.031.

[229] A. Ghosh, B. Norton, A. Duffy, Measured overall heat transfer coefficient of a suspended particle device switchable glazing, Appl. Energy. 159 (2015) 362–369. doi:10.1016/j.apenergy.2015.09.019.

[230] B.S. En, Glass in building — Determination of the emissivity, (2001).

[231] CIE 15, Technical Report: Colorimetry, Color. 3rd Ed. 552 (2004) 24. doi:ISBN 3 901 906 33 9.

[232] S. Yoon, S. Tak, J. Kim, Y. Jun, K. Kang, J. Park, Application of transparent dye-sensitized solar cells to building integrated photovoltaic systems, Build. Environ. 46 (2011) 1899–1904. doi:10.1016/j.buildenv.2011.03.010.

[233] N. Lynn, L. Mohanty, S. Wittkopf, Color rendering properties of semi-transparent thin-film PV modules, Build. Environ. 54 (2012) 148–158. doi:10.1016/j.buildenv.2012.02.010.

[234] 75-1988 CIE Publication, Spectral Luminous Efficiency Functions Based Upon Brightness Matching for Monochromatic Point Sources with 2° and 10° Fields ISBN 3900734119, (1988).

[235] C.S. McCamy, Correlated color temperature as an explicit function of chromaticity coordinates, Color Res. Appl. 17 (1992) 142–144. doi:10.1002/col.5080170211.

[236] A. Ghosh, B. Norton, Solar Energy Materials & Solar Cells Interior colour rendering of daylight transmitted through a suspended particle device switchable glazing, Sol. Energy Mater. Sol. Cells. 163 (2017) 218–223. doi:10.1016/j.solmat.2017.01.041.

[237] A. Ghosh, B. Norton, A. Duffy, Effect of sky clearness index on transmission

of evacuated (vacuum) glazing, Renew. Energy. 105 (2017) 160–166. doi:10.1016/j.renene.2016.12.056.

[238] T. Gil-Lopez, C. Gimenez-Molina, Influence of double glazing with a circulating water chamber on the thermal energy savings in buildings, Energy Build. 56 (2013) 56–65. doi:10.1016/j.enbuild.2012.10.008.

[239] T.T. Chow, C. Li, Z. Lin, Thermal characteristics of water-flow double-pane window, Int. J. Therm. Sci. 50 (2011) 140–148. doi:10.1016/j.ijthermalsci.2010.10.006.

[240] A. Ghosh, B. Norton, Durability of switching behaviour after outdoor exposure for a suspended particle device switchable glazing, Sol. Energy Mater. Sol. Cells. 163 (2017) 178–184. doi:10.1016/j.solmat.2017.01.036.

[241] P.A. Waide, B. Norton, Variation of insolation transmission with glazing plane position and sky conditions, Trans. Am. Soc. Mech. Eng. J. Sol. Energy Eng. 125 (2003) 182–189. doi:10.1115/1.1563630.

[242] A. Ghosh, B. Norton, A. Duffy, Effect of atmospheric transmittance on performance of adaptive SPD-vacuum switchable glazing, Sol. Energy Mater. Sol. Cells. 161 (2017) 424–431. doi:10.1016/j.solmat.2016.12.022.

[243] T.E. Kuhn, Calorimetric determination of the solar heat gain coefficient g with steady-state laboratory measurements, Energy Build. 84 (2014) 388–402. doi:10.1016/j.enbuild.2014.08.021.

[244] A. Ghosh, T.K. Mallick, Evaluation of optical properties and protection factors of a PDLC switchable glazing for low energy building integration, Sol. Energy Mater. Sol. Cells. (2017) 0–1. doi:10.1016/j.solmat.2017.10.026.

[245] O. Bouvard, S. Vanzo, A. Schüler, Experimental determination of optical and thermal properties of semi-transparent photovoltaic modules based on dye-sensitized solar cells, Energy Procedia. 78 (2015) 453–458. doi:10.1016/j.egypro.2015.11.696.

[246] A. Ghosh, B. Norton, A. Duffy, Effect of sky conditions on light transmission through a suspended particle device switchable glazing, Sol. Energy Mater. Sol. Cells. 160 (2017) 134–140. doi:10.1016/j.solmat.2016.09.049.

[247] A. Ghosh, B. Norton, T.K. Mallick, Daylight characteristics of a polymer dispersed liquid crystal switchable glazing, Sol. Energy Mater. Sol. Cells. 174 (2018) 572–576. doi:10.1016/j.solmat.2017.09.047.

[248] E.S. Lee, D.L. DiBartolomeo, Application issues for large-area electrochromic windows in commercial buildings, Sol. Energy Mater. Sol. Cells. 71 (2002) 465–491. doi:10.1016/S0927-0248(01)00101-5.

[249] M. Sudan, G.N. Tiwari, Daylighting and energy performance of a building for composite climate: An experimental study, Alexandria Eng. J. 55 (2016) 3091–3100. doi:10.1016/j.aej.2016.08.014.

[250] A. Thanachareonkit, J.L. Scartezzini, M. Andersen, Comparing daylighting performance assessment of buildings in scale models and test modules, Sol. Energy. 79 (2005) 168–182. doi:10.1016/j.solener.2005.01.011.

[251] K. Kakiage, Y. Aoyama, T. Yano, K. Oya, J. Fujisawa, M. Hanaya, Highly-efficient dye-sensitized solar cells with collaborative sensitization by silyl-anchor and carboxy-anchor dyes, Chem. Commun. 51 (2015) 15894–15897. doi:10.1039/C5CC06759F.

[252] H.M. Upadhyaya, S. Senthilarasu, M. Hsu, D.K. Kumar, Solar Energy

Materials & Solar Cells Recent progress and the status of dye-sensitised solar cell (DSSC) technology with state-of-the-art conversion ef fi ciencies, Sol. Energy Mater. Sol. Cells. 119 (2013) 291–295. doi:10.1016/j.solmat.2013.08.031.

[253] W.J. Lee, E. Ramasamy, D.Y. Lee, J.S. Song, Dye-sensitized solar cells: Scale up and current-voltage characterization, Sol. Energy Mater. Sol. Cells. 91 (2007) 1676–1680. doi:10.1016/j.solmat.2007.05.022.

[254] H. Apostoleris, M. Stefancich, M. Chiesa, Tracking-integrated systems for concentrating photovoltaics, Nat. Energy. 1 (2016) 16018. doi:10.1038/nenergy.2016.18.

[255] H. Baig, N. Sarmah, D. Chemisana, J. Rosell, T.K. Mallick, Enhancing performance of a linear dielectric based concentrating photovoltaic system using a reflective film along the edge, Energy. 73 (2014) 177–191. doi:10.1016/j.energy.2014.06.008.

[256] I. Santos-gonzález, M. Sandoval-reyes, O. García-valladares, N. Ortega, Design and Evaluation of a Compound Parabolic Concentrator for Heat Generation of Thermal Processes, Energy Procedia. 57 (2014) 2956–2965. doi:10.1016/j.egypro.2014.10.331.

[257] E. Dissociation, S. States, Q. Yu, Y. Wang, Z. Yi, N. Zu, J. Zhang, M. Zhang, P. Wang, High-Efficiency Dye-Sensitized Solar Cells : The Influence of Lithium Ions on, 4 (n.d.) 6032–6038.

[258] M.C. Kao, H.Z. Chen, S.L. Young, C.Y. Kung, C.C. Lin, The effects of the thickness of TiO 2 fi lms on the performance of dye-sensitized solar cells, Thin Solid Films. 517 (2009) 5096–5099. doi:10.1016/j.tsf.2009.03.102.

[259] W. Zhao, H. Bala, J. Chen, Y. Zhao, G. Sun, J. Cao, Z. Zhang, Thickness-Dependent Electron Transport Performance of Mesoporous TiO2 Thin Film For Dye-Sensitized Solar Cells, Electrochim. Acta. 114 (2013) 318–324. doi:10.1016/j.electacta.2013.09.165.

[260] H. Desilvestro, What Physical Factors Affect Current-Voltage Characteristics of Dye Solar Cells?, Dye. Tech. Lit. (2008) 1–16.

[261] K. Okada, H. Matsui, T. Kawashima, T. Ezure, N. Tanabe, 100 mm × 100 mm large-sized dye sensitized solar cells, 164 (2004) 193–198. doi:10.1016/j.jphotochem.2004.01.028.

[262] Effect of Light Intensity, (n.d.). http://www.pveducation.org/pvcdrom/effect-of-light-intensity (accessed July 18, 2017).

[263] M. Sabry, Temperature optimization of high concentrated active cooled solar cells, NRIAG J. Astron. Geophys. 5 (2016) 23–29. doi:10.1016/j.nrjag.2016.03.002.

[264] O. Dupré, R. Vaillon, M.A. Green, Thermal Behavior of Photovoltaic Devices, 2017. doi:10.1007/978-3-319-49457-9.

[265] P.J. Sebastian, A. Olea, J. Campos, J.A. Toledo, S.A. Gamboa, Temperature dependence and the oscillatory behavior of the opto-electronic properties of a dye-sensitized nanocrystalline TiO 2 solar cell, 81 (2004) 349–361. doi:10.1016/j.solmat.2003.11.011.

[266] Q. Wang, J. Moser, M. Gra, Electrochemical Impedance Spectroscopic Analysis of Dye-Sensitized Solar Cells, (2005) 14945–14953.

[267] M. Adachi, M. Sakamoto, J. Jiu, Y. Ogata, S. Isoda, Determination of parameters of electron transport in dye-sensitized solar cells using

electrochemical impedance spectroscopy., J. Phys. Chem. B. 110 (2006) 13872–80. doi:10.1021/jp061693u.

[268] K. Lee, V. Suryanarayanan, K. Ho, Author ' s personal copy A photo-physical and electrochemical impedance spectroscopy study on the quasi-solid state dye-sensitized solar cells based Author ' s personal copy, 185 (2008) 1605–1612. doi:10.1016/j.jpowsour.2008.07.094.

[269] J. Fan, S. Liu, J. Yu, Enhanced photovoltaic performance of dye-sensitized solar cells based on TiO2 nanosheets/graphene composite films, J. Mater. Chem. 22 (2012) 17027. doi:10.1039/c2jm33104g.

[270] J.H. Kim, K.J. Moon, J.M. Kim, D. Lee, S.H. Kim, Effects of various light-intensity and temperature environments on the photovoltaic performance of dye-sensitized solar cells, Sol. Energy. 113 (2015) 251–257. doi:10.1016/j.solener.2015.01.012.

[271] Q. Tang, J. Wang, B. He, P. Yang, Can dye-sensitized solar cells generate electricity in the dark?, Nano Energy. 33 (2017) 266–271. doi:10.1016/j.nanoen.2017.01.047.